

Charged Pion Photoproduction Cross Section and Beam Asymmetry Measurement on HD

Holger Meyer

Dissertation submitted to the Faculty of the
Virginia Polytechnic Institute and State University
in partial fulfillment of the requirements for the degree of

Doctor of Philosophy
in
Physics

Marvin Blecher, Chair
John Ficenec
Andrew Sandorfi
Joseph Slawny
Bruce Vogelaar

August 8, 2002
Blacksburg, Virginia

Keywords: Photoproduction, Cross Section, Beam Asymmetry, Polarization, HD-target
Copyright 2002, Holger Meyer

Charged Pion Photoproduction Cross Section and Beam Asymmetry Measurement on HD

Holger Meyer

ABSTRACT

The charged pion production reactions $d(\gamma, \pi^+n)$, $d(\gamma, \pi^-p)$, $HD(\gamma, \pi^+n)X$ were studied using linearly polarized γ -rays with energies in the range from 260 MeV to 370 MeV at the Laser Electron Gamma Source (LEGS). A solid HD target was used in this experiment for the first time. The beam asymmetry data for the $d(\gamma, \pi^-p)$ reaction significantly add to the previously available data. This gives new input to multipole analysis of pion production. A slight deviation from the beam asymmetry predicted for the free neutron is observed. The cross sections in the $d(\gamma, \pi^-p)$ channel agree with previous measurements.

Dedication

Meinen Eltern, Ingrid und Heinz-Jürgen, für ihre grenzenlose Unterstützung. *

To my wife, Mikyung, for her love.

To my daughter, Alexandra Dahee, for the joy she gives with every smile.

*To my parents, Ingrid and Heinz-Jürgen, for their unlimited support.

Acknowledgments

The LEGS collaboration provided a stimulating and friendly work environment. I particularly wish to thank Andy Sandorfi, Marvin Blecher, Sam Hoblit, Albert Lehmann, and Xiangdong Wei for their support and discussions. At Virginia Tech Chris Thomas assisted in administrative tasks, providing more help than anybody could hope for.

Contents

1	Motivation for Pion Photoproduction Experiments	1
1.1	Introduction	1
1.2	The Nucleon and Amplitudes	1
1.3	Extraction of free neutron observables from measurements on deuterium	3
1.4	Observables	3
1.5	Sum Rules	4
2	The Beam	6
2.1	Introduction	6
2.2	Compton Backscattering	6
2.2.1	Kinematics	7
2.2.2	Cross Section	8
2.3	The NSLS X-ray Ring at BNL	9
2.3.1	Backgrounds to the LEGS Beam	11
2.4	The Laser System	12
2.4.1	The Argon-Ion Laser	13
2.4.2	The DUV Ring Laser	13
2.4.3	Beam Transport and Polarization States	13
2.4.4	Beam Polarization	14
2.5	The Tagging Spectrometer	15
3	Target	17

3.1	Introduction	17
3.1.1	Other targets	17
3.2	Target theory	18
3.3	Target production	19
3.3.1	Target cell	19
3.3.2	Preparation of HD and Injection of the target	21
3.4	Target transfer and Target during data taking	22
4	Detector	24
4.1	Introduction	24
4.2	Crystal Box	26
4.3	pn Bars	27
4.4	Lead glass wall	28
4.5	Veto detectors	28
4.5.1	Gas-Cherenkov detector	29
4.5.2	Aerogel veto detector	29
4.6	Beam flux monitor CG3	30
4.7	Beam monitor wire chambers	30
4.8	Tagging spectrometer	31
4.9	DAQ electronics	31
4.9.1	The trigger logic	32
4.9.2	FERA readout and Event structure	32
4.10	Upgrades	35
4.10.1	Neutron-barrel	35
4.10.2	Time Projection Chamber	36
5	Data Taking at LEGS	38
5.1	Introduction	38
5.2	NQ-DAQ Software and other controls	38

5.3	LEGS data runs in 1999 and 2000	39
5.3.1	November 1999 data set	40
5.3.2	April 2000 data set	40
6	The Data Analysis Software	41
6.1	Introduction	41
6.2	NQ-Analysis Software	41
6.3	SASYSOFT	42
6.4	Monte Carlo	42
6.5	Data preprocessing	43
6.5.1	Data format conversion	43
7	Calibrations	44
7.1	Introduction	44
7.2	Timing calibrations	44
7.2.1	Introduction	44
7.2.2	Tagger	45
7.2.3	pn bars	45
7.2.4	Lead Glass	47
7.2.5	Trigger tdc's	48
7.2.6	tdc calibration tests	48
7.3	Energy calibrations	49
7.3.1	Introduction	49
7.3.2	Tagger	49
7.3.3	Xtal Box	56
7.3.4	pn bars	60
7.3.5	Lead Glass	61
7.4	Beam Flux calibration	61
7.5	Target length determination	62

8	Correction for Accidental Hits in the Tagger	64
8.1	Introduction	64
8.2	Accidental subtraction	64
9	Empty Target Subtraction	66
9.1	Introduction	66
9.2	Comparison of HD and Empty Target spectra	66
10	Detector Thresholds and Resolutions	69
10.1	Introduction	69
10.2	Energy thresholds	70
10.3	Position resolutions	71
10.4	Timing resolutions	72
10.5	Energy resolutions	72
11	Particle Identification	77
11.1	Introduction	77
11.2	Clustering of Hits	77
11.3	Charged Particle Identification	78
11.4	Nucleon Identification	79
12	Energy Spectra of Pions	81
12.1	Energy Deposit of Positive Pions	81
12.2	Energy Deposit of Negative Pions	81
12.3	Missing Energy spectra	82
13	Detector Efficiency	87
14	Calculation of Cross Section and Beam Asymmetry from the Data	89
15	Cross Sections	92

15.1 Errors	93
16 Beam Asymmetries	98
16.1 Errors	99
17 Conclusion	106
18 Outlook	107
A Data tables	110

List of Figures

2.1	Compton scattering kinematics	7
2.2	Energy spectrum and angular distribution of the beam	9
2.3	LEGS facility floor plan	11
2.4	Tagger magnet system	16
3.1	HD energy levels	19
3.2	HD target cell	20
3.3	IBC nose	23
4.1	The Spin Asymmetry Detector Array	25
4.2	Kinematic acceptance of pions	26
4.3	Coordinate System	27
4.4	DAQ electronics (schematic), part 1	33
4.5	DAQ electronics (schematic), part 2	34
4.6	Event structure	35
7.1	Crosstalk in the pn bars	47
7.2	Kinetic energy of neutrons	54
8.1	True-/Accidental- spectrum of the tagger	65
9.1	Missing energy of protons from deuteron breakup, no empty target subtraction	67
9.2	Missing energy of protons from deuteron breakup, flux normalized empty target subtraction	68

9.3	Missing energy of protons from deuteron breakup, empty target subtracted with factor 1.2	68
10.1	Energy spectra showing hardware thresholds for some detectors	73
10.2	Position resolution in Xtal box corner 4, row 1, column 2	74
10.3	Position and tof resolution in PN bars	75
10.4	Energy resolution of the Xtal box	76
11.1	E-dE plots for xtal box and pn bars, no cuts.	79
11.2	<i>rtof</i> in the pn bars	80
11.3	E-dE plot for the pn bars for particles with <i>rtof</i> > 1.5.	80
12.1	π^+ energy deposit in the xtal box	83
12.2	π^- energy deposit in the xtal box	84
12.3	π^\pm missing energy	85
12.4	π^+ missing energy	85
12.5	π^- missing energy	86
14.1	ϕ dependence of the asymmetry $\frac{Y_0 - Y_{90}}{Y_0 + Y_{90}}$	91
15.1	Differential cross section for $d(\gamma, \pi^- p)p$ vs. θ_{CM}	94
15.2	Differential cross section for $d(\gamma, \pi^+ n)n$ vs. θ_{CM}	95
15.3	Differential cross section for $d(\gamma, \pi^- p)p$ vs. θ_{lab}	96
15.4	Differential cross section for $d(\gamma, \pi^+ n)n$ vs. θ_{lab}	97
16.1	Beam asymmetry for $d(\gamma, \pi^- p)p$ vs. θ_{CM}	100
16.2	Beam asymmetry for $d(\gamma, \pi^+ n)$ vs. θ_{CM}	101
16.3	Beam asymmetry for $HD(\gamma, \pi^+ n)$ vs. θ_{CM}	102
16.4	Beam asymmetry for $d(\gamma, \pi^- p)p$ vs. θ_{lab}	103
16.5	Beam asymmetry for $d(\gamma, \pi^+ n)$ vs. θ_{lab}	104
16.6	Beam asymmetry for $HD(\gamma, \pi^+ n)$ vs. θ_{lab}	105

List of Tables

2.1	NSLS X-ray ring parameters.	10
2.2	Laser lines available at LEGS	12
2.3	Fit parameters for beam polarization	15
7.1	Tagger energy calibrations	55
7.2	Photon beam flux in November 1999	62
10.1	Summary of detector thresholds and resolutions.	73
15.1	Systematic errors for the cross sections.	93
16.1	Systematic errors for the beam asymmetries.	99
A.1	$d\sigma/d\Omega[\mu b/sr]$ for $HD(\gamma, \pi^+n)$, CM frame.	111
A.2	$d\sigma/d\Omega[\mu b/sr]$ for $d(\gamma, \pi^+n)n$, CM frame	111
A.3	$d\sigma/d\Omega[\mu b/sr]$ for $d(\gamma, \pi^-p)p$, CM frame.	111
A.4	Beam asymmetry for $HD(\gamma, \pi^+n)$, CM frame.	111
A.5	Beam asymmetry for $d(\gamma, \pi^+n)n$, CM frame	112
A.6	Beam asymmetry for $d(\gamma, \pi^-p)p$, CM frame.	112
A.7	$d\sigma/d\Omega[\mu b/sr]$ for $HD(\gamma, \pi^+n)$, lab frame.	112
A.8	$d\sigma/d\Omega[\mu b/sr]$ for $d(\gamma, \pi^+n)n$, lab frame	112
A.9	$d\sigma/d\Omega[\mu b/sr]$ for $d(\gamma, \pi^-p)p$, lab frame.	113
A.10	Beam asymmetry for $HD(\gamma, \pi^+n)$, lab frame.	113
A.11	Beam asymmetry for $d(\gamma, \pi^+n)n$, lab frame	113

A.12 Beam asymmetry for $d(\gamma, \pi^-p)p$, lab frame. 113

blank

Chapter 1

Motivation for Pion Photoproduction Experiments

1.1 Introduction

The underlying motivation for doing pion photoproduction experiments is to further the understanding of the nucleon. In this chapter aspects of the theory are reviewed that are relevant to pion photo production experiments. No attempt is being made to review the current status of our understanding of the nucleon completely. Within the scope of this work a comprehensive overview of the theory is not possible.

1.2 The Nucleon and Amplitudes

To a large extent, the baryon spectrum is successfully predicted by a wide range of models. Transitions between the nucleon ground state and excited states (resonances) provide tests of nucleon structure models that are considerably more stringent. Most of these transitions involve pion production through $\gamma + N \longrightarrow N^* \longrightarrow \pi + N$ where N^* is a nucleon resonance defined by its isospin I , angular momentum J , and parity P . In the calculation of reactions, nucleon wave functions and amplitudes characterized by these quantum numbers are necessary. Also, the helicity (i.e. particle spin quantized along its momentum) of initial and final state can be used to characterize a reaction. Helicity amplitudes have simple relations to the observables. Commonly used are the electromagnetic multipole transition amplitudes obtained by expanding the total amplitude into eigenamplitudes of the photon and pion angular momentum. A detailed explanation of these amplitudes and their relations to each other can for example be found in [1]. This reference contains a useful appendix that relates the notations used by different authors and is thus recommended as a starting point for the

reader interested in a discussion exceeding the brief overview following in the remaining part of this section.

Since the pion has spin 0, there is a total of eight different helicity combinations. Due to parity conservation only half of these are independent. The initial photon helicity can be chosen as $\lambda_\gamma = +1$, such that the total initial helicity is $\lambda = 1 - \lambda_{N1} = +\frac{1}{2}$ or $+\frac{3}{2}$, where λ_{N1} is the initial nucleon helicity. The final helicity μ is given by the helicity of the final nucleon λ_{N2} as $\mu = -\lambda_{N2}$. It is either $-\frac{1}{2}$ or $+\frac{1}{2}$. The resulting four helicity amplitudes can be labeled by the change in helicity as $H_N(\theta)$, $H_{SP}(\theta)$, $H_{SA}(\theta)$, and $H_D(\theta)$ for *No* spin flip, *Single* spin flip with initially *Parallel* spins, *Single* spin flip with initially *Antiparallel* spins, and *Double* spin flip. The helicity amplitudes depend on the scattering angle θ of the pion.

The total scattering amplitude squared is the sum of the squared helicity amplitudes. The unpolarized cross section σ is thus given as

$$\sigma(\theta) = \frac{q}{2k} \left(|H_N(\theta)|^2 + |H_{SP}(\theta)|^2 + |H_{SA}(\theta)|^2 + |H_D(\theta)|^2 \right) \quad (1.1)$$

where q and k are the center-of-momentum momenta of the pion and photon, respectively. With linearly polarized photons, the cross sections from photons polarized in the scattering plane or perpendicular to the scattering plane, σ_{\parallel} and σ_{\perp} , differ. The beam asymmetry $\Sigma = \frac{\sigma_{\parallel} - \sigma_{\perp}}{\sigma_{\parallel} + \sigma_{\perp}}$ is related to the helicity amplitudes through

$$\Sigma(\theta)\sigma(\theta) = \frac{q}{2k} \text{Re} (H_{SP}(\theta)H_{SA}^*(\theta) - H_N(\theta)H_D^*(\theta)). \quad (1.2)$$

The helicity amplitudes can be expanded as a sum of reduced matrix elements, or multipole amplitudes, of definite total angular momentum j which do not depend on the scattering angle. The angular dependence enters only in the Legendre polynomials P_l . Each total angular momentum state has contributions from the two parity states. The state with pion angular momentum l and final nucleon spin $+\frac{1}{2}$ has $j = l + \frac{1}{2}$ with parity $(-1)^l$, while the state with pion angular momentum $l + 1$ and nucleon spin $-\frac{1}{2}$ has same $j = (l + 1) - \frac{1}{2}$, but opposite parity $(-1)^{l+1}$. It is straight forward to form linear combinations of the total angular momentum multipoles that have definite parity and photon and pion angular momentum. The notation for the four amplitudes uses subscripts $l+$ to denote the state with final pion momentum l and $j = l + \frac{1}{2}$ and $(l + 1)-$ for the state with final pion momentum $l + 1$ and same j . The multipole amplitudes are related to the helicity amplitudes through the equations:

$$\begin{aligned} H_N(\theta) &= \sqrt{\frac{1}{2}} \cos\left(\frac{\theta}{2}\right) \sum_{l=0}^{\infty} \left[(l+2)(E_{l+} - M_{(l+1)-}) + l(M_{l+} + E_{(l+1)-}) \right] (P'_l - P'_{l+1}) \\ H_{SP}(\theta) &= \sqrt{\frac{1}{2}} \cos\left(\frac{\theta}{2}\right) \sin(\theta) \sum_{l=1}^{\infty} \left[E_{l+} - M_{l+} - E_{(l+1)-} - M_{(l+1)-} \right] (P''_l - P''_{l+1}) \\ H_{SA}(\theta) &= \sqrt{\frac{1}{2}} \sin\left(\frac{\theta}{2}\right) \sum_{l=0}^{\infty} \left[(l+2)(E_{l+} + M_{(l+1)-}) + l(M_{l+} - E_{(l+1)-}) \right] (P'_l + P'_{l+1}) \end{aligned}$$

$$H_D(\theta) = \sqrt{\frac{1}{2}} \sin\left(\frac{\theta}{2}\right) \sin(\theta) \sum_{l=1}^{\infty} [E_{l+} - M_{l+} + E_{(l+1)-} + M_{(l+1)-}] (P_l'' + P_{l+1}'') \quad (1.3)$$

1.3 Extraction of free neutron observables from measurements on deuterium

Besides the phenomenological multipole model, other more fundamental theoretical models of the nucleon and its interactions are needed, especially when one tries to extract information on the free neutron from measurements on the deuteron or other nuclei. A meson exchange model has been developed by T. Sato and T.-S. H. Lee [3],[4]. Based on this model for the nucleon, a joint effort of the LEGS collaboration and Harry Lee is now underway to develop a model of the deuteron. This model, once it reproduces the deuteron data observed at LEGS, can then be used to extract the observables for the free neutron.

The first (and largest) change from a model of the free nucleon to a model of the deuteron takes into account the Fermi motion of the nucleons inside the deuterium nucleus. This is the impulse approximation. Results of the impulse approximation calculations will be shown for comparison with the results. Other modifications take into account final state interactions, etc. These parts of the theory are still being worked on. The data presented in this work will be useful in improving the model of the deuteron.

1.4 Observables

The cross section and beam asymmetry are the two observables for which data are extracted in this work. However, for a complete determination of the pion amplitude a measurement of eight independent observables is needed [2]. All observables except for the unpolarized cross section are asymmetries. Besides the beam asymmetry Σ the target polarization asymmetry T and recoil nucleon polarization asymmetry P can be measured. Further observables describe double polarization asymmetries with two of beam, target, and recoil polarization required. Even with polarized beams and targets, only six beam-target observables are independent and recoil polarization will ultimately be needed to completely determine the pion amplitude in a model independent way. Each of the single polarization asymmetries Σ , T , and P , can be expressed as a double polarization observable in the two other polarizations. In particular the recoil polarization P can be measured using a target polarized transverse to the reaction plane and linearly polarized photons with polarization in the reaction plane and perpendicular to it. Thus there is a total of eight observables that can be measured for each of the four pion production reactions (charged and neutral pion production on protons and neutrons). The differential cross section in a direction (θ, ϕ) is given in terms of these

observables, the target polarization \mathcal{P} , and the beam polarization \wp as

$$\begin{aligned} \frac{d\sigma}{d\Omega}(\theta, \phi) = \frac{d\sigma}{d\Omega}(\theta) \cdot [& 1 + \Sigma(\theta) \cdot 1 \cdot \wp_{0/90} \cos(2\phi) \\ & - E(\theta) \cdot \mathcal{P}_z \cdot \wp_C \\ & + G(\theta) \cdot \mathcal{P}_z \cdot \wp_{\pm 45} \sin(2\phi) \\ & + T(\theta) \cdot \mathcal{P}_y \\ & - P(\theta) \cdot \mathcal{P}_y \cdot \wp_{0/90} \cos(2\phi) \\ & + F(\theta) \cdot \mathcal{P}_x \cdot \wp_C \\ & - H(\theta) \cdot \mathcal{P}_x \cdot \wp_{\pm 45} \sin(2\phi)] \end{aligned} \quad (1.4)$$

The different angular dependencies on each observable are expressed in the sine and cosine functions in this equation. The subscripts x , y , and z refer to target polarization in the scattering plane, perpendicular to it, and along the photon momentum, respectively. The subscripts on the beam polarization denote linear polarization in and perpendicular to the scattering plane (0/90), linear polarization at 45° above and below the scattering plane (± 45), and left/right circular polarization (C).

With a target polarized in the beam direction four observables (σ , Σ , E , and G) can be measured simultaneously. The simultaneous measurement of many variables reduces the ambiguities due to systematic errors from different experiments in fitting the multipoles.

1.5 Sum Rules

Sum rules for the various polarizabilities of the nucleon and other quantities have been derived from dispersion relations since the 1950's [5]. In recent years particularly the Gerasimov-Drell-Hearn (GDH) sum rule and the related forward spin polarizability sum rule have received a lot of attention because it now becomes possible to measure these sum rules.

The GDH sum rule, found in 1965 independently by S. B. Gerasimov [6] and S. D. Drell and A. C. Hearn [7], relates the anomalous magnetic moment of a nucleon to the integral over energy of the total cross section difference for absorption of circularly polarized photons of positive and negative helicity on a nucleon polarized in the photon direction (i.e. to the E asymmetry of the previous section):

$$\frac{\alpha}{2M^2} \kappa^2 = \int_{\omega_{thr}}^{\infty} \frac{\sigma_{1/2}(\omega) - \sigma_{3/2}(\omega)}{\omega} d\omega \quad (1.5)$$

Here α is the fine-structure constant, M is the nucleon mass, κ is the nucleon anomalous magnetic moment, the subscripts 1/2 and 3/2 refer to the total helicity of initial states with

spins parallel and anti-parallel, respectively, and ω is the photon energy, integrated from pion production threshold to infinity. This sum rule is valid for both proton and neutron.

The sum rule for the forward spin polarizability γ_0 is closely related to the GDH sum rule. Only the energy weighting is different:

$$\gamma_0 = \frac{-1}{4\pi^2} \int_{\omega_{thr}}^{\infty} \frac{\sigma_{1/2}(\omega) - \sigma_{3/2}(\omega)}{\omega^3} d\omega \quad (1.6)$$

Both sum rules are derived with the forward Compton scattering amplitude $A(\omega)$ as a starting point. It can be written in a general form as

$$A(\omega) = f(\omega^2)\epsilon' \cdot \epsilon + i\omega g(\omega^2)\sigma \cdot (\epsilon' \times \epsilon) \quad (1.7)$$

where ϵ and ϵ' are the initial and final photon polarizations and σ is the target nucleon spinor. $f(\omega^2)$ and $g(\omega^2)$ can be expanded for low energies ω as

$$\begin{aligned} f(\omega^2) &= \frac{-e^2}{4\pi M} + (\alpha + \beta)\omega^2 + \mathcal{O}(\omega^4) \\ g(\omega^2) &= \frac{-e^2\kappa^2}{8\pi M^2} + \gamma_0\omega^2 + \mathcal{O}(\omega^4) \end{aligned} \quad (1.8)$$

Here the lowest order coefficient in f is the Thomson cross section, α and β are electric and magnetic dipole polarizability of the nucleon, the lowest order in g is the low energy limit of Low [8] and Gell-Mann and Goldberger [9], and γ_0 is the forward spin polarizability of the nucleon.

Using a dispersion relation from [5], the sum rules follow, if we assume no subtraction, i.e. convergence of the integral or $g(\infty) = 0$.

Chapter 2

The Beam

2.1 Introduction

To do the type of experiment described in this work a photon beam with high flux, high polarization, and high energy (150 MeV to 400 MeV) is needed. The LEGS (*Laser Electron Gamma Source*) facility provides a beam with these properties by Compton backscattering laser light from electrons in a storage ring.

The LEGS facility is located at the X5 beam line of the X-ray ring at the National Synchrotron Light Source (NSLS) at Brookhaven National Laboratory (BNL) on Long Island, New York. The X-ray storage ring circulates electrons of (nominal) 2.5 GeV (before May 2000) or 2.8 GeV (since May 2000 and in October/November 1999).

This chapter gives a full discussion of the LEGS beam and the underlying principles. However, for a description that explores some of the particular aspects in more detail, see [10].

2.2 Compton Backscattering

The scattering of photons from electrons is named the Compton Effect. Arthur Holly Compton studied the effect in 1923. It is very well understood theoretically. If the electron is relativistic in the lab frame, there are some interesting consequences that were first pointed out in 1963 [11, 12] and imply that a high flux, high polarization, and high energy photon beam can be produced by directing a polarized laser beam head-on into an electron beam. Due to the Lorentz transformation the scattered photons will be in a very narrow cone along the electron momentum in the lab frame, thus giving a backscattered beam. More properties are discussed in the following subsections.

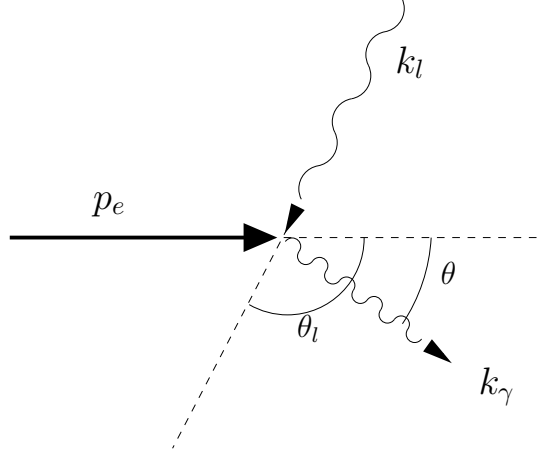


Figure 2.1: Kinematics of Compton scattering: The incoming electron has four-momentum $p_e = (\gamma m_e; 0, 0, \beta \gamma m_e)$, the incoming laser photon is $k_l = (\epsilon_l; 0, \epsilon_l \sin \theta_l, \epsilon_l \cos \theta_l)$, the outgoing photon $k_\gamma = (E_\gamma; 0, E_\gamma \sin \theta, E_\gamma \cos \theta)$, and the outgoing electron is not shown.

2.2.1 Kinematics

The maximum energy of the photon beam and the fact that the scattered photons form a beam follow from kinematics of Compton scattering. Conservation of four-momentum relates the scattering angle of the photon to its final energy. In the Lab frame, where the electron is moving with velocity βc (see figure 2.1), the energy of the scattered photon is

$$E_\gamma = \frac{\epsilon_l (1 - \beta \cos \theta_l)}{(1 - \beta \cos \theta) + \frac{\epsilon_l}{\gamma m_e} (1 - \cos(\theta - \theta_l))} \quad (2.1)$$

Here ϵ_l is the energy of the incoming photon (subscript l for *laser*), θ_l is the angle between directions of travel of the initial photon and electron, and θ the angle between final photon and initial electron, as shown in figure 2.1. γm_e is the energy of the electron in the Lab frame. For the case of $\theta_l \approx \pi$, i.e. for head-on colliding electron- and laser-beam, this can be approximated very well as

$$E_\gamma \approx \frac{4\epsilon_l \gamma^2}{1 + 4\frac{\epsilon_l}{m_e} \gamma + \theta^2 \gamma^2} \quad (2.2)$$

The other approximations used to derive formula 2.2 from 2.1 are $1 - \beta \approx \frac{1}{2\gamma^2}$ and $\sin \frac{\theta}{2} \approx \frac{\theta}{2}$. The scattered photons are Lorentz-boosted from the electron rest frame, where they have angle θ^{ERF} into a narrow beam around $\theta = 0$ in the lab, where

$$\cos \theta = \frac{\beta + \cos \theta^{ERF}}{1 + \beta \cos \theta^{ERF}} \quad (2.3)$$

and $1 - \beta \approx 2 \times 10^{-8}$ for the electron beam at the NSLS. The photons scattered at large angles θ in the lab are too low in energy to be of interest. Thus approximating the sin function with its argument is justified. In figure 2.2 the angle θ is plotted versus E_γ for one of the laser energies and storage ring energy used at LEGS.

The highest energy of the backscattered photons is reached for $\theta = 0$ in formula 2.2. It is given below in table 2.2 for values of laser- and electron-energies available at LEGS.

2.2.2 Cross Section

To get a better idea of the energy spectrum, total beam rate, and beam-polarization, it is necessary to consider the cross section. It was first calculated by Klein and Nishina [13]. The differential cross section is

$$\frac{d\sigma}{d\Omega} = \frac{1}{4} r_e^2 \left(\frac{E_\gamma^{ERF}}{\epsilon_l^{ERF}} \right)^2 \left[\frac{\epsilon_l^{ERF}}{E_\gamma^{ERF}} + \frac{E_\gamma^{ERF}}{\epsilon_l^{ERF}} + 4 \cos^2 \Theta - 2 \right] \quad (2.4)$$

Here $r_e = \frac{\alpha \hbar}{m_e c} = 2.8 \times 10^{-15} \text{m}$ is the classical electron radius and Θ is the angle between the initial and final photon polarization. The electron polarization has been averaged over the initial and summed over the final state. We see that the cross section for final photon polarizations parallel to the initial photon polarization is always larger than that for final photon polarizations perpendicular to the initial polarization. At LEGS, $\frac{\epsilon_l^{ERF}}{m_e}$ is small ($< 6\%$) and the total cross section is approximately equal to the Thomson cross section $\sigma_T = \frac{8\pi}{3} r_e^2$. In this approximation the cross section for the perpendicularly polarized final photon vanishes, as E_γ^{ERF} becomes equal to ϵ_l^{ERF} . Thus the polarization of the incoming photons is largely preserved. In practice the polarization as a function of gamma ray energy has to be obtained from a detailed simulation that takes into account the momentum spread of the electrons in the storage ring, the degree of polarization of the incident laser beam, etc. It shows that the polarization is nearly 100% at the Compton edge (as expected from helicity constraints) and reduces for lower energies to a minimum of 75%.

From the total cross section the intensity of the scattered beam can be estimated using the parameters of the laser (power, energy, and area of the beam) and the electron beam (number of electrons in the interaction region). The cross section is sufficient to perform nuclear physics experiments in a short time. For the LEGS facility the gamma ray flux is about $1 - 2 \times 10^6$ Hz.

To determine the energy spectrum of the produced beam, we have to consider the differential cross section with respect to the energy of the final photon. Averaging over initial spins, it is

$$\frac{d\sigma}{dE_\gamma} = \frac{\pi r_e^2}{2} \frac{m_e^2}{\epsilon_l E_e^2} \left[\frac{m_e^4}{4\epsilon_l^2 E_e^2} \left(\frac{E_\gamma}{E_e - E_\gamma} \right)^2 - \frac{m_e^2}{\epsilon_l E_e} \left(\frac{E_\gamma}{E_e - E_\gamma} \right) + \frac{E_e - E_\gamma}{E_e} + \frac{E_e}{E_e - E_\gamma} \right] \quad (2.5)$$

The energy spectrum does not fall off at high energies. It is relatively flat, as shown in figure 2.2.

As noted before, the angle θ and the energy are related, such that for a given energy the beam forms a cone of fixed opening angle. In the case of linearly polarized beams the intensity around this cone is modulated with $\cos^2 \Psi$, where Ψ is the angle between the initial photon polarization plane and the scattered photon momentum plane. The beam profile for circularly polarized beams is unmodulated in the azimuthal direction.

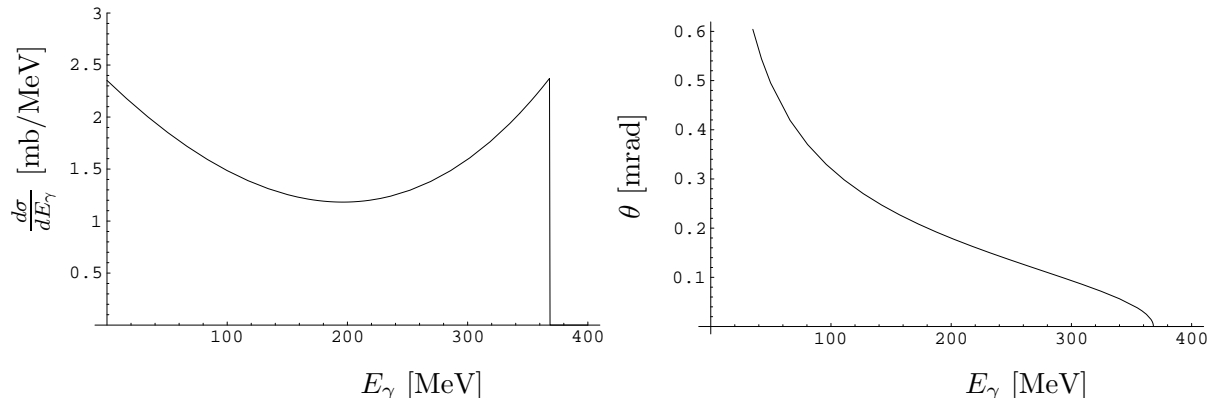


Figure 2.2: Energy spectrum and angular distribution of a beam produced from a 351 nm laser on a 2.8 GeV electron beam

2.3 The NSLS X-ray Ring at BNL

The X-ray ring at the NSLS provides synchrotron light to users at 30 beam lines. It is an electron storage ring with 170.1 meters circumference, circulating up to 350 mA of beam current in 25 bunches spaced 18.9 ns apart. Other parameters are given in table 2.1. The ring consists of eight superperiods, each covering 45° of the ring. Each superperiod consists of two straight sections with dipole magnets in between to bend the beam by 22.5° per dipole. One of the two straight sections in every superperiod is short (4.5 meters). The other one is longer (11.3 meters). The X5 beam line is located at one of the long straight sections (see figure 2.3).

During normal operation the ring is filled at twelve hour intervals. The fill procedure, from dumping the remaining electron beam to orbit corrections after injection, usually is completed within 30 minutes. Thus the beam can be used for up to twenty three hours every day, allowing almost continuous data taking. This is important when experiments are performed with (polarized) targets that decay over time.

When LEGS is producing beam, the electrons that photons scattered from are lost to the

NSLS X-ray ring parameters	
nominal electron energy (E)	2.584 GeV or 2.800 GeV
natural energy spread ($\frac{\sigma E}{E}$)	8.6×10^{-4}
rf frequency	55.88 MHz
circumference	170.1 m
electron orbit period	567.2 ns
rf bunch structure	30 bunches (25 filled during normal operation)
bunch spacing	18.9 ns
natural bunch length (2σ)	10.5cm
maximum beam current	~ 350 mA (1.2×10^{12} electrons)
lifetime	~ 20 hours
number of superperiods	8
magnet complement per superperiod	2 dipole (2.70 m long each) 5 quadrupole (0.45 m each) 2 quadrupole (0.80 m each) 4 sextupole (0.20 m each)
radiated power for bending dipoles	144 kW / 0.25 A of beam current
horizontal damped emittance (ϵ_x)	1.0×10^{-7} m rad
vertical damped emittance (ϵ_y)	1×10^{-10} m rad

Table 2.1: NSLS X-ray ring parameters.

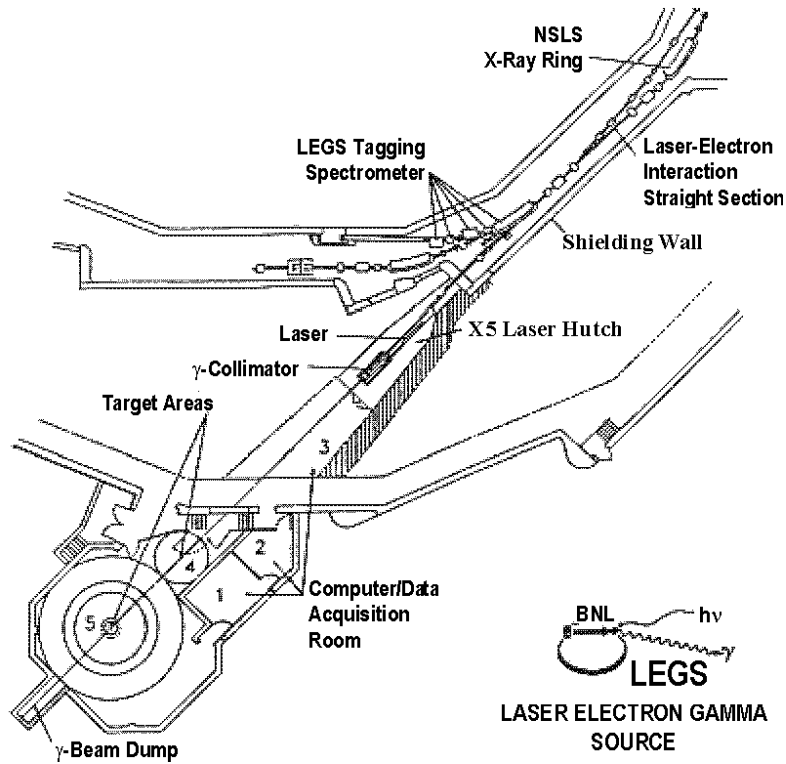


Figure 2.3: LEGS facility floor plan: Part of the NSLS X-ray ring is shown on top. The LEGS beam line (X5) extends to the laser hutch shown in the center. The LEGS target area is shown at the bottom

ring. This causes the lifetime to drop. The partial life time due to LEGS operations may not exceed 20 hours in order to not interfere with experiments at other beam lines.

2.3.1 Backgrounds to the LEGS Beam

The synchrotron radiation is much too low in energy (up to tens of keV at the NSLS) to be a concern as a background to the LEGS photon beam. It does however damage the beam optics significantly and the optics has been designed to minimize this damage.

Another source of photons is bremsstrahlung from the residual gas left in the storage ring. This is monitored during data taking and results in a $\sim 1\%$ unpolarized addition to the photon beam from compton backscattering.

Wavelength λ [nm]	ϵ_l [eV]	$E_{\gamma max}$ [MeV] for ...	
		$E_{e^-} = 2584$ MeV ($\gamma = 5056.8$)	$E_{e^-} = 2800$ MeV ($\gamma = 5479.8$)
514.5	2.41	225.0	262.3
501.7	2.47	230.2	268.4
496.5	2.50	232.4	270.9
488.0	2.54	236.1	275.1
476.5	2.60	241.3	281.1
472.7	2.62	243.0	283.1
465.8	2.66	246.3	286.9
457.9	2.71	250.1	291.3
454.5	2.73	251.8	293.3
363.8	3.41	307.1	357.1
351.1	3.53	316.9	368.3
334.4	3.71	330.7	384.2
302.0	4.11	361.2	419.2
263.3	4.71	406.0	470.6

Table 2.2: Laser lines available at LEGS (partial list): for each wavelength λ the corresponding energy of the laser photon ϵ_l and the maximum energy of the photon beam $E_{\gamma max}$ for each NSLS ring energy are given. The bold entries are the modes used to take data (but see text for details). Other modes were used for calibration of the tagger.

2.4 The Laser System

In order to produce a high quality beam, the laser system needs to operate reliably at high intensity. The optics has to deliver a high degree of polarization in the polarization states desired (linear and/or circular) and the degree of polarization has to be known precisely. Finally, the system has to be able to provide laser lines of different energies, such that the desired kinematic range can be covered with a consistently high degree of polarization (cf. section 2.2.2). This poses various technical difficulties, as most parts of the beam optics are wavelength specific and will not work well for other wavelengths than the one they are specified for.

Two different lasers are used at LEGS. They are located in the laser hutch, about 20 meters away from the center of the interaction straight section of the X-ray ring. The laser beam is directed through a system of mirrors into the straight section, where the Compton-backscattering happens. The resulting gamma beam gets to the target room experimental area through the same beam pipe in which the laser beam travels toward the electron beam, through the laser hutch, and through another beam pipe.

2.4.1 The Argon-Ion Laser

The laser used to provide all but the highest photon energy is an *Innova-100* manufactured by Coherent. It is a Ar-Ion CW laser that can operate at a variety of single laser lines or in various multiline modes. The wavelengths between 515 nm and 300 nm are listed in table 2.2. Power output is up to 28 W for a multiline visible mode and drops to 3 W for the 302 nm line mode. In the multiline-UV mode (MLUV) the power output is at most 9 W, split into 334.4 nm, 351.1nm, and 363.8 nm with fractions of approximately 15%, 50%, and 35% respectively. This laser can operate continuously for long times, does not require a lot of maintenance, and works quite reliably. The tube of this laser has a lifetime of 1000 hours. The quartz Brewster windows of the tube slowly damage under the intense UV radiation inside the cavity. The damaged quartz absorbs power and the resulting heating distorts the window, resulting in a laser beam of modes other than the preferred TEM₀₀. The other modes have two disadvantages. First, they result in a drastically reduced gamma beam flux, because the intensity profile of the laser beam in the straight section does not match the profile of the electron beam any more. And second, the beam optics can no longer give a high degree of polarization, as the optics is optimized to the TEM₀₀ mode.

2.4.2 The DUV Ring Laser

The Deep-UV ring laser provides a laser beam of 263.3 nm wavelength. It was not used in the current set of experiments and is mentioned here for completeness only. It consists of a 'ring' that actually has the shape of a rhombus with mirrors on two corners and sets of two mirrors with a crystal in between at the two other corners. The infra-red beam of a commercial laser is coupled into the ring through the back of one of the two mirrors that sandwich the first crystal. In this crystal photons in the IR are absorbed and photons of half the wavelength are emitted. This produces a green beam that circulates in the ring. In the second crystal two photons of the green beam can be converted into one photon of 263.3 nm wavelength. The photons of this wavelength are coupled out of the ring through a mirror that is transparent for the DUV, but reflects the green beam. The optical length of the ring is adjusted to an integer multiple of the wavelength of the green beam (526.6 nm). This causes the stimulated absorption of two photons in the crystals to happen at a rate that enables high output power in the DUV. With a few watts of stored power of the green beam in the ring, more than one watt of DUV power can be obtained.

2.4.3 Beam Transport and Polarization States

Through mirrors the beams from the lasers are transported onto an optical bench, where the beams from both lasers are combined. On the optical bench the desired polarization state is prepared through a combination of quarter- and half-wave plates. These plates can be

flipped into or out of the beam controlled through a computer interface. From the optical bench the beam is transported into the straight section of the storage ring through the *zag*, a window to the vacuum of the beam line, and a mirror inside the vacuum. The *zag* is a set of two steerable mirrors that can be both tilted and translated to focus the laser-beam in the center of the straight section. The settings of the *zag* mirrors have to be adjusted manually at the beginning of a run. Then a computerized feedback system controls the *zag* to maximize the gamma ray flux as measured by the tagger rate. During data taking the polarization setting of the beam is cycled through the set of desired states (linear at -45° , 0° , 45° , and 90° with respect to the horizontal direction, and left-/right-circular) at ~ 5 minute intervals of randomly changing duration. This greatly reduces systematic uncertainties in the data compared to the scenario of taking data in each state sequentially for an extended length of time.

As described in section 2.2.2 the beam profile depends on the polarization state. The differences in the profile can be observed using the beam monitor wire chambers. During data taking the gamma ray beam is collimated in the laser hutch (followed by a sweeping magnet to clean the beam of charged particles created on the collimator walls). This is necessary to ensure that the beam size at the target does not exceed the target diameter. It also ensures that the differences in the beam profiles are practically negligible. The collimator may cut different fractions of the flux for different polarizations or different energies. However, the differences of the beam profile after collimation are limited to variations inside the small target diameter. Using different beam profiles in Monte Carlo simulations it was confirmed that the detector response is insensitive to the beam profile. Thus no corrections to the data are applied to compensate for the differences in beam profile.

2.4.4 Beam Polarization

The polarization of the laser is measured (using a Brewster window) several times throughout each running period. For the November 1999 data the laser polarizations were $P_0^l = 0.993 \pm 0.003$ and $P_{90}^l = 0.983 \pm 0.005$ for 0° and 90° linear polarization states. A full Monte Carlo of the laser and electron beam characteristics was performed to determine the polarization of the backscattered photons for a fully polarized beam. A polynomial fit to the result of this simulation depends on the backscattered photon energy E_γ as a fraction of the Compton edge energy E_γ^{max} . For each linear polarization state the fit parameters are given in table 2.3.

$$\wp_{0/90}(E_\gamma) = \sum_{i=0}^4 a_i \left(\frac{E_\gamma}{E_\gamma^{max}} \right)^i \quad (2.6)$$

Putting these two pieces together while taking the small fraction of bremsstrahlung into account, the polarization of the beam is obtained as

$$P_0^\gamma(E_\gamma) = P_{brem} \left\{ P_0^l \wp_0(E_\gamma) - \frac{1}{2} (1 - P_0^l) [\wp_{90}(E_\gamma) - \wp_0(E_\gamma)] \right\} \quad (2.7)$$

	\wp_0	\wp_{90}
a_0	2.0101	-0.18833
a_1	-13.295	-2.7913
a_2	33.497	14.738
a_3	-31.246	-16.409
a_4	10.031	5.6481

Table 2.3: Fit parameters for beam polarization

with $P_{brem} = 0.99$ and equivalent for $P_{90}^\gamma(E_\gamma)$.

2.5 The Tagging Spectrometer

The tagging spectrometer, also called tagger, is the device used to determine the energy of the beam on an event by event basis. This is done by *tagging* the electron that a particular photon in the beam was scattered from. The sum of photon and electron energy is conserved. An electron that scattered a photon has a lower energy than the other electrons in the ring. It's trajectory in the dipole magnet downstream of the straight section is a stronger bend, such that at the end of the dipole it is separated by ~ 5 cm from the electron beam. From this point on it will travel through three more tagger magnets and finally be detected. Since the bending of the trajectory in the field of the magnets depends on the electron's energy, it's position in the tagger focal plane is a function of it's energy. The tagger focal plane is described in section 4.8. Here the tagger magnet system and controls are discussed.

The arrangement of the tagger magnets is shown in figure 2.4. The D1 dipole is part of the X-ray ring. It's field is dictated by the energy of electrons circulating in the storage ring. The fields of the other three dipoles need to be adjusted by the LEGS group to change the direction of electrons from photon collisions toward the focal plane. Lower energy electrons (corresponding to higher energy photons) will be deflected the most. In order to make good use of the available width of the focal plane it is desirable to deflect electrons from the highest energy photons such that they will hit the focal plane close to the edge on the side furthest away from the x-ray ring beam. For an experiment at higher photon energies this implies that the tagger magnet fields need to be lower than for an experiment at lower photon energies. Rather than provide adjustments for each of the three controlled tagger magnets individually, the fields are controlled through an interface that takes as input a mode ($0 < \text{mode} < 1$) and the ring energy. This allows easy reproduction of tagger settings at different times and to shift the Compton-edge in the tagger at the push of a button. During one data taking period small shifts in the electron orbit of the X-ray ring can be compensated by small adjustments to the tagger mode. These adjustments keep the energy calibration of the tagger valid throughout the data taking. Usually the orbit does not change from run to

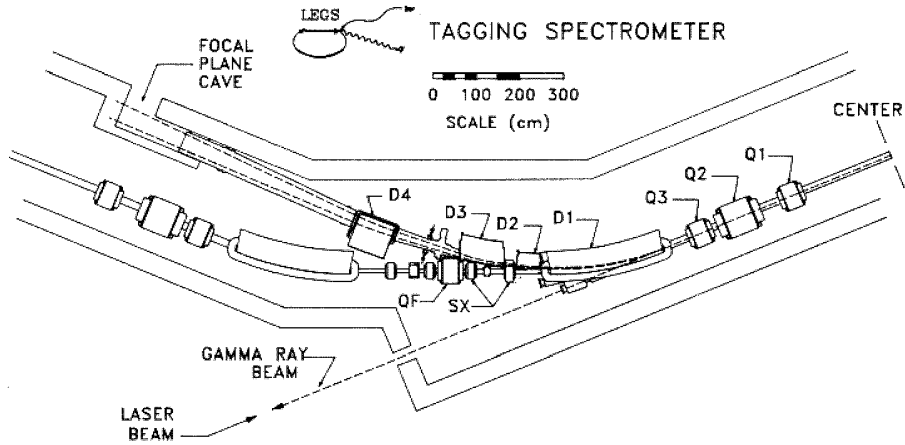


Figure 2.4: The tagger magnet system consists of one of the ring dipoles (D1) and three more dipole magnets (D2, D3, and D4). The other ring magnets, quadrupoles Q1, Q2, Q3, and QF, as well as sextupoles SX are also shown. The Laser electron interaction region is in the straight section on the right side.

run and only rarely small adjustments are necessary.

For the method of calibrating the tagger using the Compton edges from various laser lines it is important to point out that the position of the hit on the tagger depends solely on the energy of the electron after scattering, i.e. the final photons of the same energy are tagged in the same channel, irrespective of what laser line was used to produce the beam. This is true to the extent that the energy difference of the incoming photons from different laser lines is negligible (and it is: less than 2 eV, much less than the spread in energy of the electrons stored in the beam), and the scattering angle of the electron is negligible. Just as for the photons, the large range of electron scattering angles in the electron rest frame ($90^\circ < \theta_{electron}^{ERF} \leq 180^\circ$) collapses into a very small cone around 0° . Formula 2.3 (valid only for photons) has to be replaced for the scattered electron e' with

$$\cos \theta_{e'} = \frac{\beta \frac{E_{e'}^{ERF}}{p_{e'}^{ERF}} + \cos \theta_{e'}^{ERF}}{\sqrt{1 + 2\beta \frac{E_{e'}^{ERF}}{p_{e'}^{ERF}} \cos \theta_{e'}^{ERF} + \beta^2 \left(\left(\frac{E_{e'}^{ERF}}{p_{e'}^{ERF}} \right)^2 - \sin^2 \theta_{e'}^{ERF} \right)}} \quad (2.8)$$

where $\frac{E_{e'}^{ERF}}{p_{e'}^{ERF}}$ is the ratio of the scattered electron energy to its momentum in the initial electron rest frame. Substituting in the above formula the electron scattering angle in the electron rest frame as a function of the photon scattering angle or the final photon energy, the small size of the cone for $\theta_{e'}$ can be verified. Taking into account the quadrupole magnets of the NSLS storage ring, that the electrons travel through on their way to the tagger, we see that for the purpose of tagging it is inconsequential which laser line produces the beam.

Chapter 3

The frozen HD target

3.1 Introduction

The SPHICE (**S**trongly **P**olarized **H**ydrogen and Deuterium **I**CE) target used in this set of experiments is a solid hydrogen-deuteride target. While in the current experiment the target is unpolarized, the target was designed to achieve high polarization for both protons and neutrons. The target dewar was built to support polarized targets, i.e. contains coils to apply a magnetic field to the target at all times and maintain low temperatures to keep spins frozen. Another important design consideration was to have low energy thresholds, i.e. to introduce as little material as possible between the target itself and detectors used in the experiment in order to minimize energy loss of reaction particles on their way through the 'dead layers'. This was achieved by the use of different dewars for target production and target use in the experiment. Splice targets are made in a dilution refrigerator (for polarized targets) or a production dewar, can be stored in a storage dewar for later use and are used inside the detector array in an in-beam-dewar. They get transferred between the different locations using a special transfer dewar.

3.1.1 Other targets

The perfect target to do experiments on protons or neutrons would be a target containing only free protons or free neutrons respectively. In the case of protons, there exists a very good approximation to this ideal. Liquid Hydrogen targets have been used in many previous experiments at the LEGS facility and elsewhere [18]. Of course no free neutron targets exist. Instead, liquid deuterium targets have been used [19], which contain as many protons as neutrons. In experiments the contribution to cross-sections and other observables from the proton has to be subtracted to get results for neutrons. This relies on the assumption that the system of a proton and a neutron bound in a deuteron behaves like the sum of the two

free particles.

However, neither pure hydrogen nor pure deuterium targets can be polarized at magnetic fields and temperatures practical for doing nuclear physics experiments. So the need for even more complicated targets arises. Various designs have been used successfully. A group in Mainz, Germany uses a butanol target [20] and substitutes the hydrogen in the butanol with deuterium for measurements on polarized neutrons. Ammonia targets are common as well [21]. The main problem with these targets is that besides the polarized nucleons of interest, there are many other unpolarized nucleons in the other atoms (e.g. carbon and oxygen, or nitrogen) of the target molecules.

3.2 Target theory

Polarization (and depolarization) of protons and neutrons in targets depends mainly on the spin-lattice coupling through molecular rotations. Hydrogen-deuteride (HD) molecules at low temperatures will be in a molecular angular momentum state $L=0$. This means that a polarized HD target will depolarize very slowly, i.e. with a relaxation time of days even at 4K. Since there are no Pauli restrictions on the spins of each of the nuclei in HD imposed by the molecular wave function, both the H and the D can be polarized independent of each other. In contrast, in hydrogen molecules, consisting of two fermions, the orientation of nuclear spins is restricted by the symmetry of the molecule wavefunction. There are two forms of molecular hydrogen. Para-hydrogen has the spins of both atoms aligned antiparallel ($J=0$) and zero molecular angular momentum ($L=0$). In ortho-hydrogen the spins are parallel ($J=1$) and L is odd. At room temperature the ratio of o- H_2 to p- H_2 is close to 3:1. The energy splitting between the ortho- and para-state is $k_B \times 172$ K, where k_B is the Boltzmann constant. At temperatures below this o- H_2 will decay to p- H_2 with a time constant of 6.25 days. This offers a way to implement a *relaxation switch* in the target. Under normal circumstances polarization and depolarization occur at the same rate. The need for long depolarization times implies long polarization times as well. Polarization times can be shortened however, if the coupling between the spins in the HD and the crystal lattice can be increased during polarization of the target and the coupling can afterwards be turned off. Doping the HD with a small concentration (on the order of 10^{-4}) of o- H_2 does exactly this. The o- H_2 couples to both the spin of hydrogen atoms in neighboring HD molecules and to the crystal lattice. The target can be polarized in a strong magnetic field at low temperature in a short time. Then keeping the target at these conditions allows the o- H_2 to decay into the inert $L=0$ p- H_2 , *freezing* the spins of the hydrogen nuclei in the HD. Now the target can be used in an experiment in an environment of lower magnetic field and higher temperature.

A similar method can be used to polarize the neutrons in the HD by doping the target with a small concentration of D_2 . It turns out however, that this is not very practical. The decay from p- D_2 , which does couple to the lattice, to the inert o- D_2 has a time constant of 18.25 days. This would require freezing the spins for months rather than weeks, as in the case

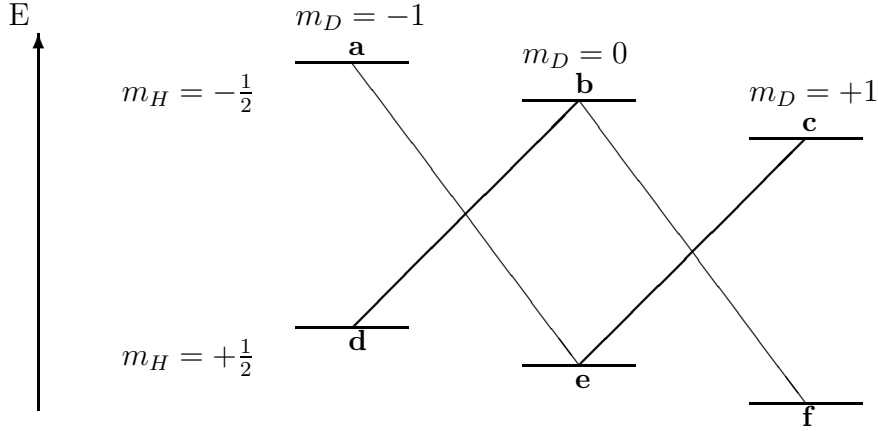


Figure 3.1: Energy levels of dipolar coupled H and D in neighboring HD molecules (schematic)

of hydrogen. Also, the maximum D polarization obtainable in this way is only $\sim 20\%$, the equilibrium deuterium polarization at 15 mK and 17 T. There is another method to polarize the deuterium in the HD. It is to transfer the polarization from H to D by means of *adiabatic fast passage* and then to repolarize the hydrogen (if desired). Figure 3.1 shows the energy levels of the dipolar coupling of H and D nuclei in neighboring HD molecules. This coupling mixes to the eigenstates of the unperturbed system (m_H, m_D) ($m_H = \pm\frac{1}{2}$, $m_D = -1, 0, 1$) small components of the states with $(m_H, m_D \pm 1)$. This makes possible the 'forbidden' transitions indicated by the lines between states a and e, b and f, b and d, and c and e, that transfer polarization from one nucleon to the other. The energy for transitions $d \leftrightarrow b$ and $e \leftrightarrow c$ is different from the energy for transitions $a \leftrightarrow e$ and $b \leftrightarrow f$. The choice of Rf-field frequency allows selection of $d \leftrightarrow b$ and $e \leftrightarrow c$ transitions with their lower frequency at a given value of magnetic field over the other forbidden transitions. The populations of the states can be inverted by sweeping through the resonant frequency. If initially the hydrogen was polarized stronger than the deuterium, this transfers polarization to the deuterium.

3.3 Target production

3.3.1 Target cell

The target consists of a copper ring that holds the target cell and screws into the various dewars, an inner and outer mylar cap to contain the HD and cooling wires. Figure 3.2 shows a schematic drawing. Figure 3.3 includes more details.

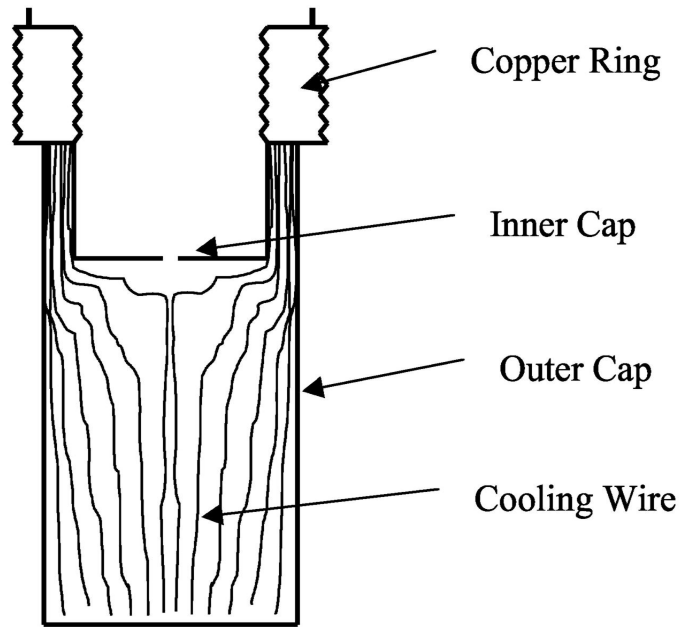


Figure 3.2: Schematic drawing of HD target cell

The copper ring has an inner diameter of 26 mm. This is the maximum size of the photon beam to be used in an experiment with this target. In the in-beam-dewar the target is mounted with its center axis centered in the beam that passes through the ring and then hits the HD. Thus, the copper ring is upstream of the HD at very backward angles. Particles do not have to pass through it on the way to the detectors. The ring is 13 mm long. It has threads on the inside and outside and four small holes on the upstream end. The four holes and the inside threads engage the transfer cryostat or a screw driver tool used to mount warm (room temperature) target cells in the dilution refrigerator or production dewar. The outside threads of the target ring fit into the cold fingers on the dilution refrigerator, production dewar, or storage dewar. On the downstream end of the ring are holes to solder the aluminum cooling wires to and grooves to glue the inner and outer mylar cap. The two caps are made from mylar formed under heat and pressure in a metal mold. The mylar is 0.127 mm (5 mil) thick. The HD is filled into the target cell through a small hole in the center of the inner cap.

The wires inside the target volume are needed to dissipate the heat released to the crystal lattice by the spin flips during polarization. The thermal conductivity of solid HD is not sufficient for this. The unpolarized target used in the November 1999 data run did not have wires. It instead had a thin copper foil inside the HD close to the outer cap in the region of the target volume that is not reached by the photon beam. The target used in April 2000 had the normal configuration of 3000 aluminum wires of 0.038 mm diameter. The wires have

a mass of 20% of the HD.

3.3.2 Preparation of HD and Injection of the target

The HD gas for target production was cleaned in a still to achieve high purity. For reasons described in section 3.2, a small content of H₂ is left in the HD. The HD is usually stored in a liquid helium bath at 4 K in the *pre-ager*. This converts all of the H₂ into the para state. The HD can then be warmed to room temperature for a controlled amount of time to convert just the right amount of H₂ into the ortho state to get the desired HD polarization time. If there is too much o-H₂ it will take too long to freeze the spins after polarization. If there is too little, the HD can not be polarized at all.

HD becomes solid at 16.6 K. To achieve high polarization temperatures of 15 mK or less are necessary. The LEGS group uses two liquid helium dewars (called the production dewar and the storage dewar) to reach temperatures of 4 K to 1.5 K and a dilution refrigerator (DF) to reach temperatures of ~ 15 mK. All three of these are top loading. The cold fingers in the DF and storage dewar can hold up to three targets at a time while the production dewar has room for only one target. Typically, to fill a target the target cell is screwed onto the injection tool and inserted into the production dewar. The target cell cools down to 4 K. The HD is filled into an expansion volume from the preager. The amount is measured by the gas pressure. The HD gas is left at room temperature for the desired amount of time and then injected into the target through the injection tool. The temperature in the target cell is controlled by lifting and lowering the injection tool out of and into the dewar. This completes the production of an unpolarized target.

To polarize a target, it is transferred into the dilution refrigerator. It is possible to inject targets inside the DF directly. However, there is a small risk of breaking the mylar of the target cell in the process. If this happens, the dewar needs to be warmed up to retrieve the HD gas and mylar pieces. This is far easier to do with the comparatively simple production dewar than with the dilution refrigerator, especially so, if there are already targets in the other positions in the DF. Inside the DF the target is polarized and then stored to freeze the spins as described in section 3.2. The practical aspects of polarizing a target and verifying the degree of polarization by means of NMR measurements are under continuous development, especially with respect to the forbidden adiabatic fast passage. For example, one improvement was to replace all materials inside the cold fingers (i.e. NMR coil holders, glues, mylar cap of the target cell, etc.) that contain hydrogen with materials that do not contain hydrogen so that background for the HD NMR measurements is reduced. The new target flasks and NMR coil forms will be made from Kel-F (C₁F₃C₂).

3.4 Target transfer and Target during data taking

During production and use of the target multiple transfers from one dewar to another occur. There are special requirements on the transfer cryostat (TC) used for this procedure. It has to connect to the originating dewar vacuum tight, mechanically engage the target as far as 110 cm inside the dewar, provide cooling and in the case of polarized targets a magnetic field while the target is extracted and then moved inside the TC to another dewar possibly in another room, then connect to the dewar the target is moved to, where again a vacuum connection has to be made to push the target into this dewar and screw it into the coldfinger there. Since the target is made in a top loading dewar with its center axis vertical and used in the experiment with its axis horizontal along the beam, it needs to be turned during the transfer into the in-beam-cryostat (IBC). This is done by rotating both the TC and the IBC to an angle of $\approx 30^\circ$ with respect to the beam direction. Turning the TC horizontal would cause the cryogenics to flow out the top end. The target transfers were a source of trouble during this experiment. The parts of the TC that have to move under vacuum developed vacuum leaks during operation resulting in cold leaks (thermal connections between parts of the transfer cryostat at different temperatures), liquid nitrogen and liquid helium boiloff, and thus target loss. The in beam cryostat was designed to hold the target during data taking. The target is inside a long 'nose' that reaches into the detector. The liquid helium reservoir and control valves are inside the can which remains outside and upstream of the detector. During the experiment the photon beam passes through the IBC entering at a window in the can, traveling along the nose and through the target, leaving through a set of aluminum foil and mylar windows on the downstream end of the IBC nose. The part of the nose that holds the target is shown in figure 3.3. In this figure the photon beam enters the IBC from the left and exits the front of the nose on the right.

In the experiment it is necessary to subtract any contributions to the data arising from reactions on the target cell. The position of the target cell during data taking with the empty cell should of course be identical to the position during the 'full target' data taking. The position can be adjusted precisely with screws at the base of the IBC stand. Yet it was found in November 1999 that it is difficult to get the target cell into the exact same position once the IBC was moved out of the detector or the target cell removed from the IBC. Instead in April 2000 the IBC was warmed up and the HD gas pumped out. Since the thermal expansion also moved the warm nose relative to its cold position, the IBC was then cooled down again for 'empty target' data taking.

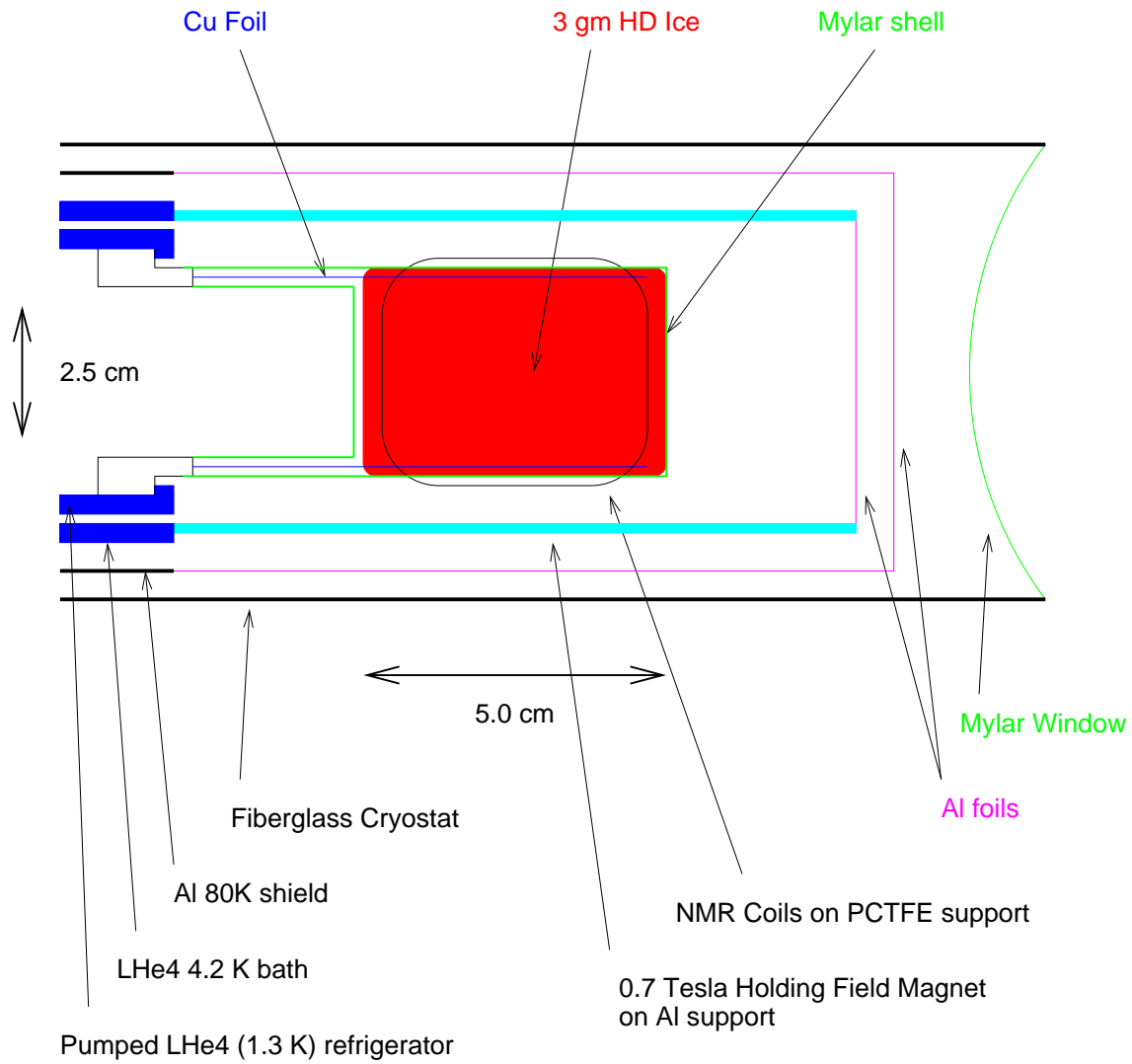


Figure 3.3: November 1999 target in IBC nose (not to scale, schematic)

Chapter 4

The Sasy detector system

4.1 Introduction

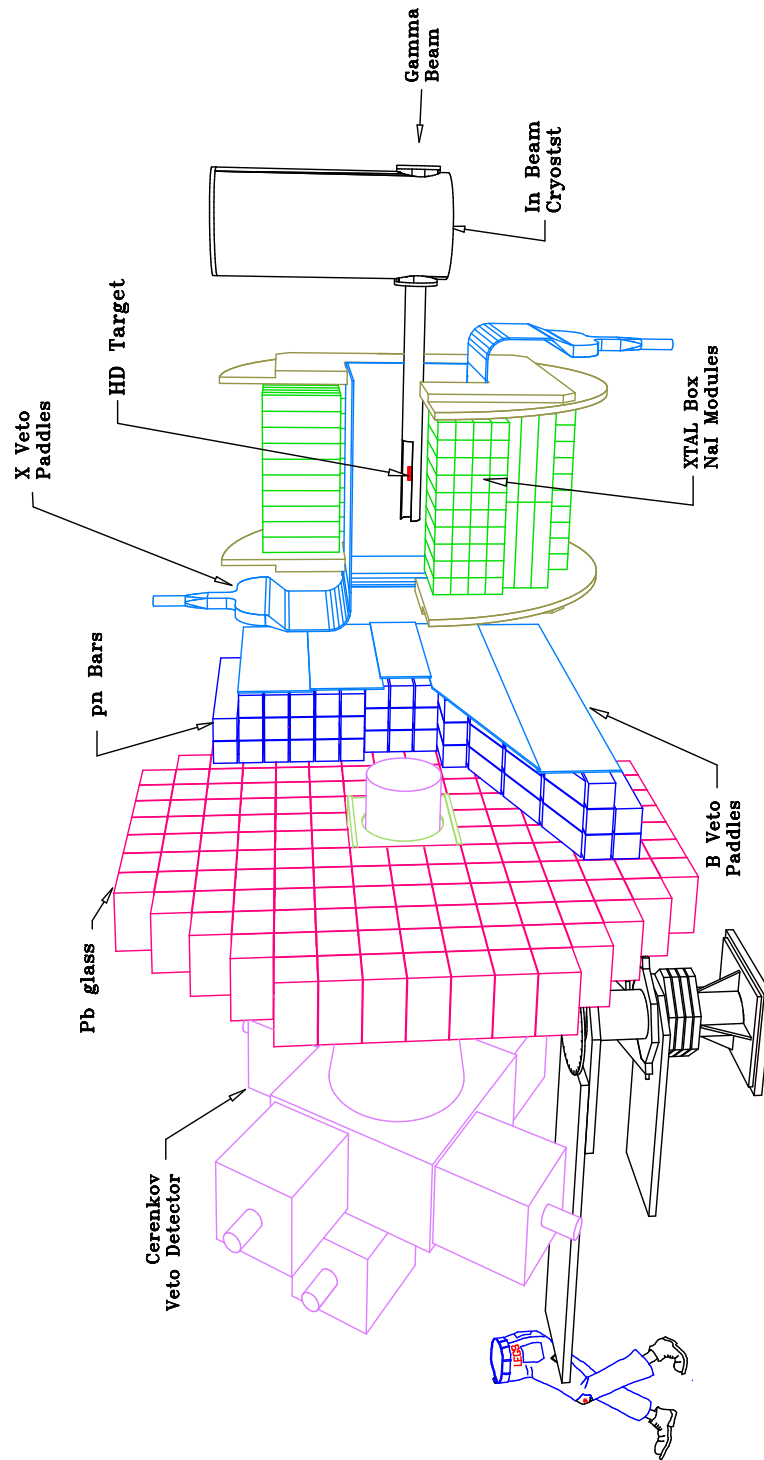
The particle detectors used in this experiment should detect photons, pions and nucleons with a large coverage of solid angle, good efficiency, and good energy and timing resolutions. Due to the kinematics of the fixed target experiment, most reaction particles are emitted in the forward direction. Thus, good coverage of the forward region is important, while the backward angles of $\theta > 130^\circ$ do not need to be covered. The *Spin ASY*mmetry spectrometer (SASY) is comprised of the various detectors used in this set of experiments. It is shown in figure 4.1.

The three major components are the 'crystal box' for full ϕ coverage at $50^\circ \leq \theta \leq 130^\circ$, the 'pn-bars' to detect nucleons at $\theta \leq 38^\circ$, and the 'lead glass wall' for photons at $\theta \leq 38^\circ$. Each of these is described below. With these detectors a gap exists in the region from $38^\circ \leq \theta \leq 50^\circ$. In addition there are several other detectors, like the Cherenkov veto detectors, the beam flux monitor, and beam monitor wire chambers. These systems are also described below.

The kinematic coverage of the detector is shown in figure 4.2 for charged pions in the xtal box with and without the requirement to detect a nucleon in the pn bars. For all beam energies used in November 1999 the pions reach the xtal box at all angles. The coincidence of a nucleon detection limits the pion region to $\theta > 80^\circ$. Also the nucleons in the bars are above threshold for beam energies above 280 MeV only. At lower beam energies and in the forward region of $\theta < 80^\circ$ some events are observed. However, these are from the tails of the energy and angular distributions that are due to Fermi motion in the target deuterons.

For future experiments upgrades of the detector system are planned. For neutron coverage at larger polar angles a 'neutron barrel' will be installed inside the crystal box. This will also fill the gap at $38^\circ \leq \theta \leq 50^\circ$. Later a time projection chamber (TPC) will replace the

SASY Present Configuration



XTBXASY2P_ASS.DWG

Figure 4.1: The Spin Asymmetry Detector Array

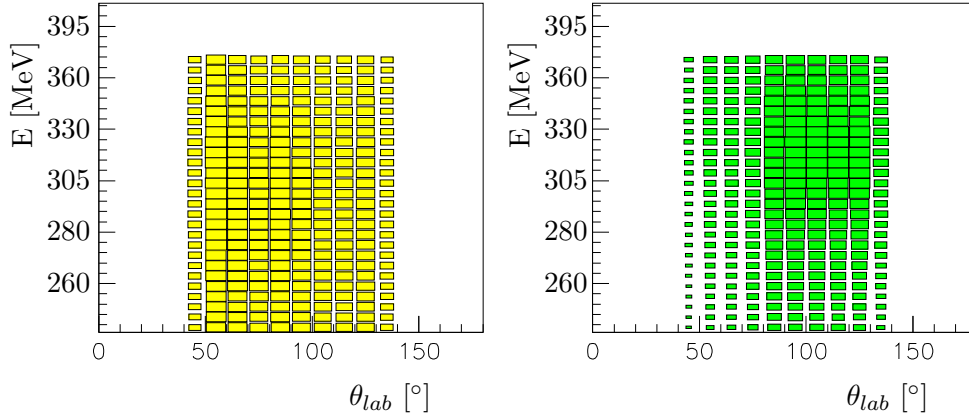


Figure 4.2: Kinematic acceptance of charged pions without detection of a nucleon (left) and with a nucleon in coincidence (right). Nucleons are fully detected only for pions at $\theta > 80^\circ$ and $E_\gamma > 280$ MeV.

neutron barrel for improved detection of charged particles.

Whenever a coordinate system is used in this or other sections, it is a right-handed Cartesian system with its origin in the center of the crystal box which coincides with the target center position. The z axis points along the beam with larger z being further downstream. The y axis points up and positive x direction is to the left looking down the beam (see figure 4.3)

4.2 Crystal Box

The Crystal Box [22], also referred to as 'xtal box', 'xt', or 'Box', is a NaI(Tl) scintillation calorimeter with 396 modules, each $6.35 \text{ cm} \times 6.35 \text{ cm}$ in cross section. It has four 'faces', each consisting of 90 modules of 30.48 cm depth arranged in nine rows by ten columns, and four 'corners' with three by three modules of 76.2 cm length each. All modules are optically isolated from each other. The faces form the sides of a box surrounding the target. Each module is read out with one photo-multiplier at the outside end. The corners are positioned along the edges where two faces touch. Each of their modules is read out by two photo-multipliers, one on the upstream and downstream ends each. This allows reconstruction of both position along the z direction and energy deposited. The corners help to contain electromagnetic showers near $\phi = 45^\circ, 135^\circ, 225^\circ,$ and 315° .

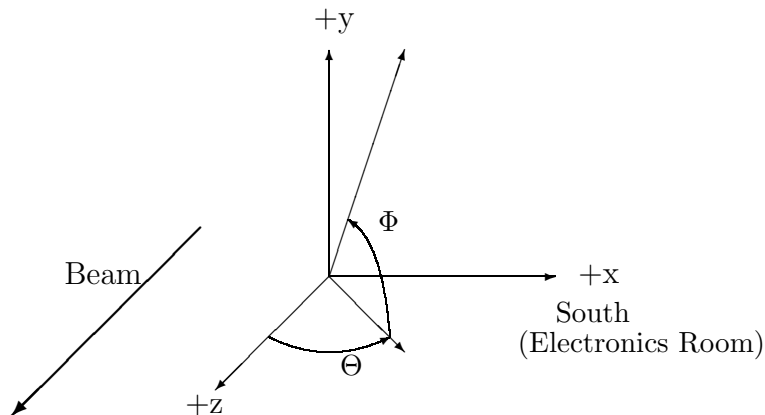


Figure 4.3: The Coordinate System

The mechanical structure of the crystal box consists of aluminum on the outside. To achieve small energy loss of particles, Hexcel is used inside each face.

The inside of each of the faces is covered by a 0.635 cm thick plastic scintillator for charged particle identification. These 'veto paddles' are read out through Lucite light guides with one photo-multiplier each. The readout was on the upstream end for the bottom veto paddle, but at the downstream end for the other three faces, such that the light guides of those three faces partly shadowed the pn-bars described below. In May 2001 the readout of all box veto paddles was moved to the upstream end.

A pulser system is installed on the xtal box to monitor gain drifts in the photomultipliers. It consists of a laser, optical splitters, and fiberoptic cables that connect to each of the modules. This system is used for short-term photomultiplier stability monitoring, whereas cosmic ray signals are used for long-term gain drift monitoring.

4.3 pn Bars

The pn Bars are an array of 43 plastic scintillator bars of 10 cm \times 10 cm cross section and 160 cm length each with a set of four 'full' and two 'half' veto paddles. The bars form three layers. The front surface of the first layer of 13 bars is at $z = 109.2$ cm. The other two layers have 15 bars each. All bars extend to $x = \pm 80.0$ cm. The three rows of bars at $y = 0$ cm and $y = \pm 10$ cm in each layer have an air gap of 33.0 cm at their center to form a hole for the photon beam. The left and right part of these 'half bars' are optically connected by air.

Upstream, just in front of the three layers of bars, are the paddles for charged particle identification. They cover the active area of the bars and leave a hole for the beam. Four

160 cm \times 30 cm paddles cover the upper and lower rows of bars and two paddles of 70 cm \times 21.5 cm cover the half bars to the left and right of a 20 cm wide opening for the beam. Each of these veto counters has a thickness of 0.635 cm. The half bar veto paddles are not optically connected. This makes it difficult to obtain position or time information. However, this shortfall can easily be compensated for by taking that information from the next layer of bars.

4.4 Lead glass wall

The lead glass wall (PbG or PB) is an array of 176 lead glass elements stacked into a wall that covers approximately a circular area of radius 110 cm. Each block is 25 cm deep and of 15 cm square profile. Photomultipliers are attached to the downstream end of each block for readout.

This detector is mainly used to detect photons from π^0 decay. The photon showers in the lead glass. Those electrons and positrons in the electromagnetic shower which are above Cherenkov threshold in the lead glass produce the light detected by the photomultipliers.

A system of LED pulsers is installed in the lead glass wall to monitor gain drifts in the photomultiplier tubes. The trigger electronics for these LEDs is installed in a few boxes at the downstream end of the wall and a small module with one LED directly connected through an optical port to each of the lead glass blocks. This pulser system provides the means to monitor small short-term gain drifts. Long-term gain drifts are monitored using signals from cosmic rays.

4.5 Veto detectors

The reactions of interest in this experiment have as their reaction products pions, nucleons and photons. Electrons are a background that has to be cut down by veto detectors to reduce trigger rates and simplify data analysis. In SASY there are two Cherenkov threshold detectors that are only sensitive to electrons, over the entire range of beam energies. One is a gas Cherenkov detector that covers a narrow forward cone. It is in the beam. For detection of electrons at larger polar angles an Aerogel Cherenkov detector is used. It consists of two subsystems, the 'forward Aerogel' and the 'Aerogel barrel'. These detectors have been assembled by the author and a next generation forward aerogel detector has been developed by the author.

Upstream of the target and detector there are two beam veto paddles. They are 1cm lead converters followed by plastic scintillators to veto the beam halo at the exit window of the beam pipe, where the beam enters the target room. These paddles are placed above and below the beam to form a slit through which the beam passes. The beam halo is more

intense in the vertical plane than in the horizontal plane and thus we choose to not place additional veto paddles to the sides of the beam.

4.5.1 Gas-Cherenkov detector

This detector detects electrons in a 5° cone centered around the beam in the downstream direction. Cherenkov photons created in a volume of tetrafluoroethane are collected through a system of five parabolic mirrors, Winston cones, and RCA 8854 photomultipliers. Four of five mirrors are located ~ 130 cm downstream of the entrance window leaving a hole at the beam position. The last mirror is ~ 170 cm downstream of the entrance window centered in the beam. This corresponds to a detection efficiency of better than 99% for electrons with energies above 50 MeV. In the ADC spectra of the photomultiplier signals peaks can be seen that correspond to signals from different numbers of photoelectrons. The efficiency was determined by fitting the number of observed photoelectrons to Poisson statistics. The measurement was in agreement with the expectations based on simulations of the detector.

4.5.2 Aerogel veto detector

The electron background is mostly due to electron positron pair production. The large Lorentz boost causes at least one of the two particles to move at a very forward angle. The Gas Cherenkov veto detector should always detect at least one of the particles in the pair. Nevertheless it was found desirable to extend the angular coverage of electron detection. The aerogel veto detector serves this purpose. The silica aerogel used as a radiator has an index of refraction of $n=1.0298$ for the aerogel SP30 used in the forward direction and $n=1.0517$ for the aerogel SP50 at larger polar angles. The higher index of reflection results in a larger number of Cherenkov photons. However, the aerogel is opaque and photons get absorbed. This is worse for the aerogel with higher index of refraction. The optimal thickness of the radiator is 3 cm.

The forward detector has three layers of four 1 cm thick 11.6 cm square pieces of SP30 aerogel with each layer slightly offset from the previous to ensure that small gaps between the pieces will not line up, improving uniformity of detection efficiency over the whole square area of the detector. There is a small hole of square aperture in the center of the aerogel to allow the photon beam to pass through as little material as possible, minimizing harmful beam interactions in the aerogel. Electrons not detected in the aerogel because of the hole at small forward angles will be seen by the gas Cherenkov veto detector. The aerogel is held at $z=28.5$ cm to 31.5 cm by a self supporting structure of aluminized mylar that also serves as the reflective light collection system to focus the Cherenkov photons on a 12.7 cm diameter photomultiplier mounted at the downstream end of the xtal box and below the path of particles from the target to the pn bars. The forward aerogel detector extends the angular coverage to a $\approx 20^\circ$ cone.

The aerogel barrel is mounted inside the xtal box. Its angular coverage overlaps the forward aerogel detector and extends to angles further backward than the acceptance of the xtal box. Three layers of 1 cm thick aerogel are mounted around the beam axis from $z = -33$ cm to $z = +24$ cm in a square profile with the inner surfaces of the aerogel at x and $y = \pm 4.6$ cm. The light is detected by four 12.7 cm diameter photomultipliers mounted at the upstream end of the detector. Light collection efficiency for this detector was poor, resulting in a low efficiency. Even so this aerogel detector helped to reduce the event rate and, especially, to clean up events in the xtal box.

4.6 Beam flux monitor CG3

The beam flux monitor CG3 (*C*ounter for *G*ammas, version *3*) is a simple but very important part of the experiment. It is located downstream of the target and other parts of SASY near the beam dump. It consists of two scintillator paddles with a layer of lead in between them. The first scintillator (PCV, *P*hoton *C*ounter *V*eto), placed upstream of the lead, is used to veto charged particles in the beam (mostly electrons from the target and other material). Photons can convert into pairs in the lead and then be detected in the second scintillator (PCC, *P*hoton *C*ounter *C*ounter), which is placed downstream of the lead. This detector responds to $\approx 5\%$ of the photons in the beam. It is calibrated (multiple times throughout a run) at a lowered beam intensity using a big NaI crystal. This crystal is usually moved out of the beam and can be moved into the beam just upstream of CG3 to measure the CG3 efficiency.

The tagging efficiency for the electrons, from which a photon was backscattered, is 100%. But not all the photons that are scattered in the storage ring get to the target, because the beam is collimated. To calibrate CG3 the fraction of tagged photons that reaches the target is measured using the NaI crystal, which is 100% efficient at detecting photons. Then the fraction of tagged photons detected by CG3 is measured with the NaI crystal moved out of the beam, but otherwise unchanged conditions. The ratio of these fractions is the calibration for CG3 and is obtained for each tagger channel.

The cross section determinations depend on the accurate measurement of the photon flux. The photon flux is measured only by CG3. Any error here would directly propagate into the cross section. CG3 was very reliable and stable throughout the data taking periods of this experiment and for many years before that.

4.7 Beam monitor wire chambers

To ensure good beam quality it is useful to monitor the photon beam profile. At the time of the experiments described here only one beam monitor wire chamber was available. It was

moved out of the beam during data taking and moved into the beam upstream of the target before each running period to determine the beam size and shape for each polarization state.

4.8 Tagging spectrometer

As described in section 2.5 a tagging spectrometer is used to detect the electrons that photons scattered from. The focal plane of this tagger is made from 64 plastic scintillator bars of 0.76 cm square cross section arranged vertical in a plane that intersects the plane of the storage ring, and is oriented such that the electrons have normal coincidence on the tagger plane. There is a second set of identical scintillators behind the first plane which is offset by one half of the width of the scintillator elements. This could be used to improve position resolution on the tagger focal plane from the 0.76 cm given by the width of each tagger element to half that number. However, the resulting improvement in position resolution would not have resulted in a better photon energy resolution due to the energy spread of the electrons in the ring. This second plane of scintillators was not used in the experiment described here.

Behind the two layers of scintillators is a Cherenkov detector with a lucide radiator and seven 2 inch diameter photomultipliers with timing resolution (300ps rms) much better than the timing resolution which can be obtained from the signals of the photomultipliers on the plastic scintillator bars. In the case of multiple tagger hits this detector does not necessarily allow identification of the improved timing signal with one of the tagger channels if two scintillator bars got hit within a short time of each other. This happens infrequently and does not pose a problem. We could not take full advantage of the improvement in tagger timing resolution because the uncertainty in time of flight of a particle is due to the combination of tagger time resolution and detector time resolution, thus the resolution of the pn bars and lead glass were not improved.

4.9 DAQ electronics

All the signals from the SASY detector system and the tagging spectrometer are brought into the electronics room through coaxial cable. The signals from PN bars and lead glass are split and input to analog and time to digital converters (ADCs or adcs and TDCs or tdc), and the event trigger. The xtal box signals are split into ADC and trigger signals. The tagger signals are processed by TDCs and the trigger logic. The veto detectors are used in making the trigger and recorded in ADCs for diagnostic purposes. For charged particles the veto ADC values contributes to the total charged particle energy. When the trigger logic produces a trigger, ADCs are gated and TDCs started. The ADCs and TDCs are FERA modules in CAMAC crates. They are read out into FERA memory modules. From the memory modules the data is transferred to a MicroVAX computer. Online histogramming and

storage of data on hard-disk are carried out by this computer. Periodically the data is copied to tape. The experiment is controlled through this and other slow-control computers.

4.9.1 The trigger logic

The trigger logic is set up in NIM modules in nine NIM crates. Its schematic is shown in figures 4.4 and 4.5. There are different triggers for different kinds of events. The 'main-event' triggers on nuclear reactions. This is accomplished by taking the coincidence of a hit in the tagger and a hit in the SASY (xtal box or pn bars or PbG in November 1999 run, xtal box or pn bars in April 2000) in anti-coincidence with the Cherenkov veto detectors. The cosmics trigger is used to collect cosmic ray data for detector pre-calibration. It can be triggered by the xtal box, the pn bars, or the PbG. The xtal box cosmics trigger is made of either a coincidence of signals in the top and bottom faces or coincidence of the two left or the two right corners. In this way cosmic rays traversing the xtal box from top to bottom will cause a trigger. For the pn bars and the PbG the cosmics trigger is simply a coincidence of at least 8 pn bar hits or 5 PbG block hits. To monitor gain changes in the beam flux monitor CG3 a small fraction (2^{-8}) of the CG3 hits trigger a 'monitor event'. There is a laser pulser system on the xtal box that can trigger box pulser events. The PbG pulsers produce PbG pulser events. There is an event to measure pedestals of the adcs which is triggered at constant frequency. This pedestal event is not enabled during data taking. Other special purpose events, e.g. to measure the veto detector efficiencies, are usually disabled, too.

4.9.2 FERA readout and Event structure

FERA modules use CAMAC crates for power supply and initialization of the FERA virtual station numbers (vsn) through the CAMAC bus. The FERA bus has a 16 bit data bus and a command bus. For each event the ADC- and TDC-modules as well as certain other information (event type, triggered by cosmics or not, etc.) are read out through the FERA bus into one of two FERA memory modules. When the memory in one module is almost full, new data will be recorded into the other memory module while the first module triggers a 'buffer event'. The computer reads out the memory module along with some other information like the polarization setting of the beam and the beam flux scalers. The reason for this double buffering scheme is to reduce the deadtime of the experiment. While one memory module is read out the trigger is alive and the experiment can take data. Another advantage is that in each buffer an event has all the information needed for its analysis and is self contained. This allows discrimination between good and bad buffer events during offline analysis. Parts of a data run can be analyzed while ignoring other parts of the same run. This is useful in cases where some part of the electronics started to malfunction during a run. The structure of a buffer event is shown in figure 4.6.

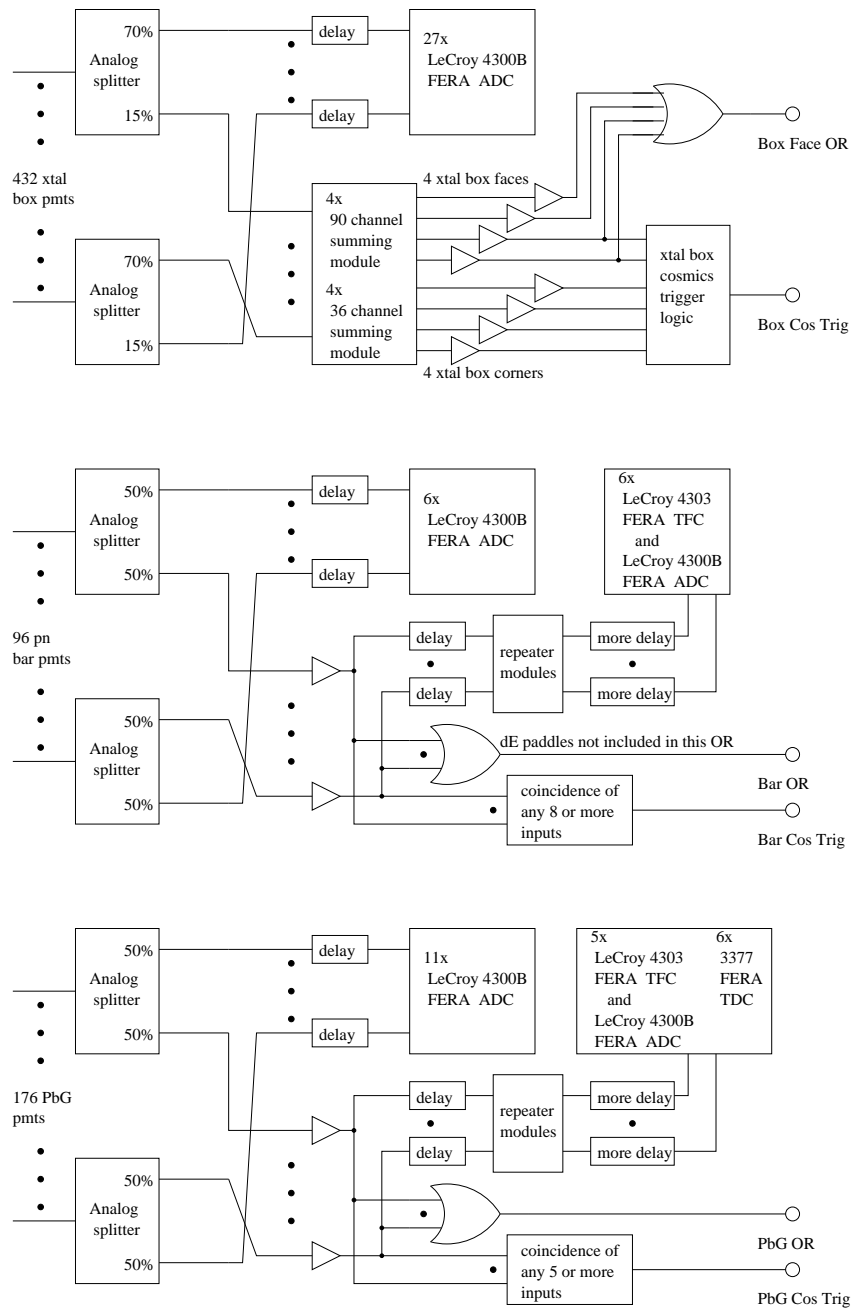


Figure 4.4: DAQ electronics (schematic), part 1: signal path from all subdetector systems to ADCs, TDCs, and trigger logic (trigger, Box dE paddles, and beam flux monitor not shown)

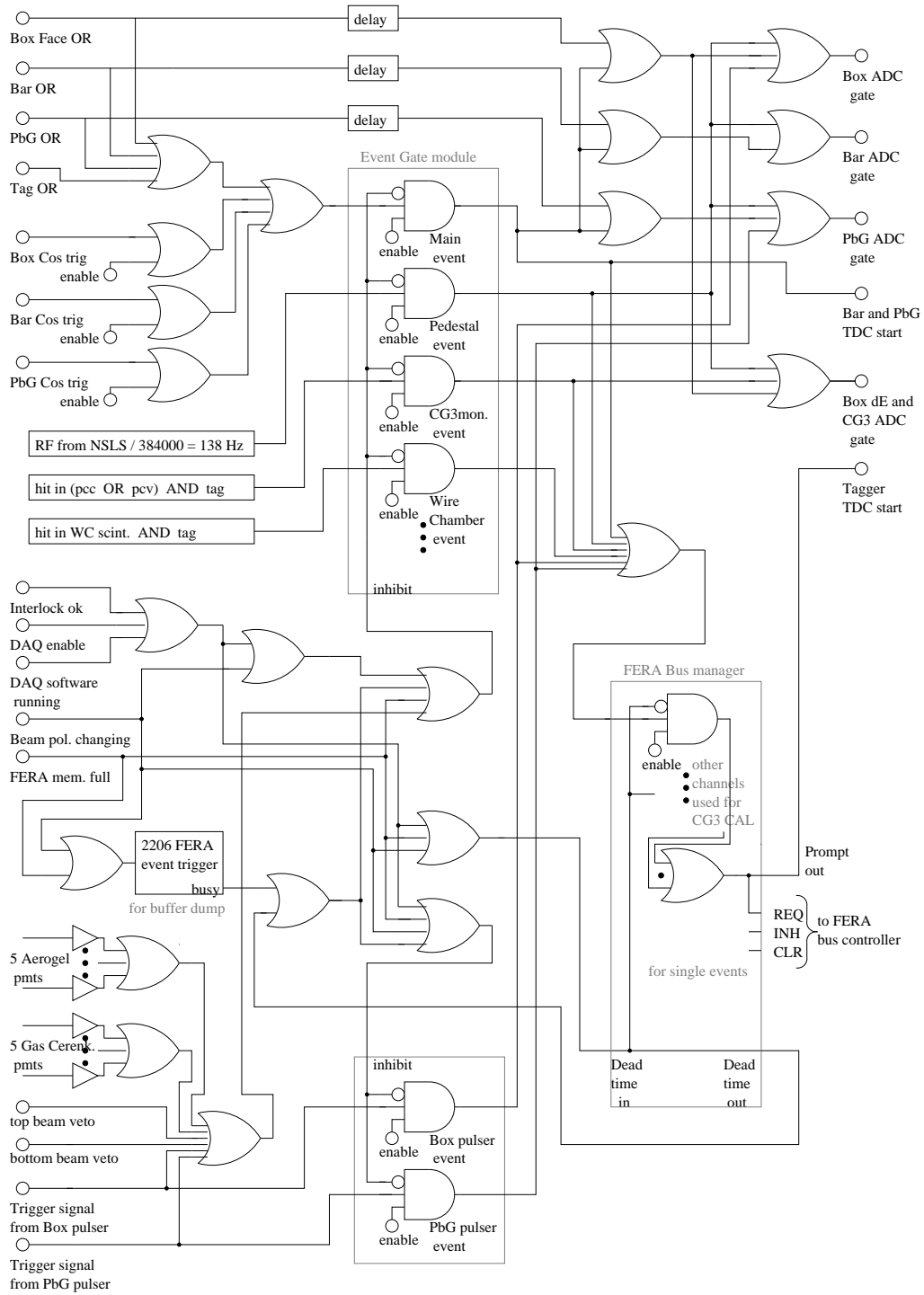


Figure 4.5: DAQ electronics (schematic), part 2: trigger logic; various scalers and registers as well as some other details are not shown to keep the schematic readable.

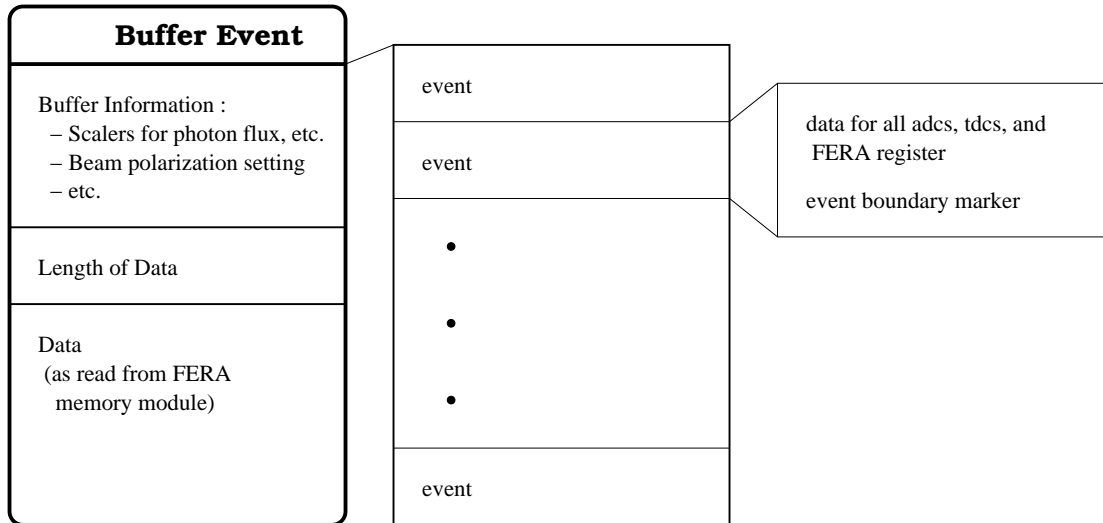


Figure 4.6: Event structure: Each FERA memory dump contains many events and the auxiliary information needed to analyze them.

4.10 Upgrades of SASY for future data runs

4.10.1 Neutron-barrel

The combination of pn-bars and xtal box has a good solid angle coverage for forward going nucleons. However, it is not possible to detect nucleons in the xtal box, over the angular range that corresponds to forward going pions. In this case the proton energy is too small or the nucleons are directed so that they miss the bars and the xtal box. Without this coincidence the determination of the reaction $\gamma p \rightarrow \pi^+ n$ for small pion polar angles is impossible due to electron contamination of the pion signal in the pn bars.

The neutron-barrel has 32 segments of scintillator that fill roughly the volume from $\theta \approx 40^\circ$ to $\theta = 90^\circ$ at a radial distance from the target of $r \approx 5$ cm to $r = 25$ cm. Each segment is read out through a lightguide at the downstream end together with wave shifting optical fibers along the radially outside surface of the counters, all connected to one Hamamatsu 580 photomultiplier per segment. On the inside of the barrel, surrounding the target, there is a charged particle delta E counter of four segments read out through curved lightguides to the upstream end of the xtal box.

Aerogel-Veto-Detector

The neutron-barrel is incompatible with the Aerogel veto detector described above, because both detectors would occupy the same space inside the xtal box. Before installation of

the neutron-barrel in the summer of 2001 those aerogel detectors (forward and barrel) were removed and a new forward aerogel detector has been designed, constructed, and installed. This new veto detector is similar to the old forward aerogel detector. It also consists of a 3 cm Aerogel Cherenkov radiator held in a self supporting structure of aluminized mylar that also serves as a mirror light collection system to focus the Cherenkov light on a single 12.7 cm diameter photomultiplier tube. The design was optimized using ray tracing modeling in the Optica environment for Mathematica. Despite the much tighter constraints on space that was available for the detector, the electron detection efficiency could be kept at the level of the old detector. Designs with more than one photomultiplier were found to give no or only minimal improvement over the design with one photomultiplier.

4.10.2 Time Projection Chamber

Particle identification by means of E-dE signature and time of flight does not allow determination of the charge of the particle. Thus π^+ and π^- cannot be identified. With an HD target reactions on neutrons and on protons take place simultaneously. To distinguish charged pion production on the neutron from that on the proton either the nucleon has to be detected or the detector needs to be upgraded to enable charge determination. This requires a large magnet to bend the charged particles and a detector to measure the resulting approximately helical tracks. A Time Projection Chamber (TPC) located inside a large super-conducting solenoid is the proposed solution. The TPC will consist of an inner and outer can surrounding the target inside the In-Beam-Cryostat nose. Its active volume is filled with a drift gas mixture. On both cans there will be gradient rings to apply a uniform drift voltage along the z axis. This will cause ionization electrons that are created along the tracks of transversing charged particles to drift to the upstream endcap of the TPC where they are detected in a readout plane. The particle track is projected in x and y onto the x and y readout and the z coordinate reconstructs from the drift time. The downstream exit of the TPC can be constructed from very thin material so that negligible energy loss occurs as the particle passes through.

The active volume is surrounded by a trigger scintillator which was developed at Virginia Tech. Outside this there is the coil of the superconducting magnet with its cooling. To start the readout of the TPC on the readout plane there has to be some trigger signal. This signal cannot come from the xtal box, because the TPC magnet may absorb particles that leave good tracks in the TPC such that there would be no signal in the xtal box. For this reason a layer of 0.3 cm \times 0.3 cm square profile scintillating fibers (Bicron, BCF 12) will be installed oriented along the z direction between the TPC and its magnet. It will be read out on the upstream end by twelve Hamamatsu 580 photomultiplier tubes in segments of 32 fibers per photomultiplier.

The magnet that provides the field for the TPC will also provide a high field in the target region. This will allow reduction of the material surrounding the target by removal of the

IBC magnet that now provides the field for the target. Studies are required to determine how the target can be loaded without the IBC magnet, because during target loading the IBC is not in the field region of the TPC solenoid.

Chapter 5

Data Taking at LEGS

5.1 Introduction

This chapter describes the process of data taking for the data sets used in this analysis. Most aspects of the data taking remained constant through the different periods of data taking. However, there are some differences between the data sets that are discussed here.

5.2 NQ-DAQ Software and other controls

The DAQ software controls the experiment. The user can issue commands to start and stop data taking, temporarily suspend a run, if short access to the experimental hall is needed, and show the status of the data acquisition. When a run is started, NQ opens an output file and writes a begin of run record that contains a user comment describing the run. Then the file contains buffer events as described in section 4.9.2. The user can insert comments into the data stream at any time. They are stored as special records in between buffer event records. This is useful if something unexpected happens during data taking. At the end of a run the output file is closed and a summary printed.

During data taking the NQ software fills histograms that can be viewed using PAW. These histograms show the raw detector data and allow to identify online detector elements that fail, problems with adc gains or tdc ranges, problems with the electron beam orbit in the NSLS storage ring, etc.

It also is useful to monitor various rates during data taking. The rate at which the veto detectors are hit (normalized to the tagger rate) gives a good indication if the beam hits the copper target ring. The rate of main events to beam flux monitor events can be used for the same purpose. The tagger rate normalized by the current in the NSLS storage ring

indicated if the laser needs to be tuned. Typical rates are $2kHz$ in the xtal box, $7kHz$ in the pn bars, and $2kHz$ in the PbG wall for a tagger rate of $1.5MHz$. The veto detectors have a combined rate of $60kHz$ (mostly due to the forward direction gas Cherenkov detector). This results in a trigger rate of $4kHz$ with the DAQ being ready to take data $\sim 90\%$ of the time.

Usually no good calibration is available during data taking for the current detector conditions. This makes a detailed online analysis impossible. Since 2001 there are however some higher level histograms that are created based on less accurate calibrations from previous running periods. These show pion peaks in the E-dE plots and allow to form asymmetries online for a large average of solid angle and beam energy.

The In-Beam-Cryostat (IBC) has to be monitored while it is cold because a variety of problems have been encountered during its operation that require human intervention. A display in the control room provides most of the information on the IBC status and allows to do some adjustments remotely. Often a flow valve on the liquid helium transfer lance needed to be adjusted. Also the pressure set point for the JT valves in the recirculation system of the IBC had to be adjusted periodically. Access to the IBC was necessary to change the helium supply dewar, to refill the liquid nitrogen trap reservoir, to change the trap, and pump out the trap not in use. Whenever such maintenance could not be done during NSLS beam fills, the data taking had to be suspended.

The NSLS beam fills happen usually twice daily at 7AM and 7PM. The shutters at all beam lines are closed, the remaining beam current is dumped, and the ring filled by the NSLS control room. After the orbit is corrected the shutters are opened and beam is available again. This usually takes ~ 30 minutes. After this the LEGS shift personnel has to make sure that the tagger spectrum did not shift, which might happen if the electron orbit in the NSLS is shifted after the fill. If necessary the spectrum can be shifted by adjusting the *mode* or *energy* setting of the tagger control system. This has not usually been necessary.

5.3 LEGS data runs in 1999 and 2000

Data was taken at LEGS on unpolarized HD targets in November 1999 and in April 2000. The main difference between these data sets is the energy range of the photon beam. In November 1999 the Argon Ion laser was used in MLUV mode and the NSLS provided electrons of 2800 MeV. In April 2000 a lower range of photon energies was explored using the visible line (488nm) of the Argon Ion laser on electrons of nominal 2584 MeV for most of the data. In both running periods the photon beam polarization was switching between 0° linear and 90° linear with equal time in each of these states. Small amounts ($\sim 4\%$) of bremsstrahlung data were taken. The polarization was flipped at random times approximately every 5 minutes.

5.3.1 November 1999 data set

The November 1999 data set consists of 18 runs with the HD target (run numbers between 4341 and 4362) and four runs with an empty target cell (run numbers 4379 and 4383-4385). The full target data consists of a total of 78 hours of data taken between 3 November 1999 and 8 November 1999. This data will be referred to as 'nov99hd'. The empty target runs add to 21 hours of data taken from 14 November 1999 to 16 November 1999. This data set is abbreviated as 'nov99mt'. The integrated photon flux of the full target data runs is 4.00445 times that of the empty target runs.

5.3.2 April 2000 data set

The April 2000 data set has nine runs (run numbers 4416 to 4424) with an HD target and the MLUV laser mode ('apr00hduv'), followed by 24 runs (4425-4448) of HD target data in the lower energy ($\lambda = 488$ nm) laser mode ('apr00hd') and nine runs of empty target data (4480-4488) at the same energy ('apr00mt'). The apr00hduv data set has no corresponding empty target data and was not used to produce physics results. However, since its energy range overlaps both the nov99hd and the apr00hd data, it was useful to perform cross checks between the data sets.

Chapter 6

The Data Analysis Software

6.1 Introduction

It is a long way from taking the data to producing cross sections and asymmetries. All steps of the offline processing and analysis of the data are discussed in the following part of this thesis, from detector calibrations and Monte Carlo simulation to reaction reconstruction, background suppression and error estimation. First the tools used for the analysis are described.

There are various people working on the analysis of the experimental data as well as related tasks like simulations for proposed new detector subsystems. Through personal preference and suitability to different tasks in the analysis the use of different softwares has developed. Here an overview of the data analysis frameworks is given.

6.2 NQ-Analysis Software

The NQ-Analysis software is derived from the NQ-DAQ software. It uses the same Q-commands to control replay of the data as are used during data taking. In addition there are commands to specify the data file or files to replay. During replay, data events are handed to the different event processes for analysis by user supplied subroutines that take the place of the rather simple online analysis processes. The NQ framework further provides a mechanism to interactively call subroutines and functions from the command line while the replay software is running. To replay the data with the user analysis routines, the analysis routines have to be compiled and the NQ-analysis-software linked against libraries with the NQ core functionality. Then the analyzer is started with QSTART from the command line. This command searches for an analyzer in the current directory and thus many analyzers for different tasks in the analysis can be worked on at the same time in different directories.

Throughout the analysis the NQ-analysis framework has been filled with a library of calibration routines, clustering algorithms, functions to calculate various kinematic variables from different inputs, etc. Also the framework has been extended by the author beyond the simple representation of the data as raw hits in the detectors to include layers of abstraction for calibrated detector data, clustered data and identified particles. At and above the layer of calibrated detector data the NQ framework can be used to replay Monte Carlo data.

Typically the analyzer will process the data by filling histograms. The histograms are created in a global section that PAW can link to. PAW is used as the histogram displaying system and can also be used to do fits and for other tasks.

6.3 SASYSOFT

The SASYSOFT software has similar functionality to the NQ-Analysis software. It is based on the ROOT package and on C++, whereas the NQ package is written in FORTRAN and uses the older PAW for histogramming. For use with this software the data first has to be converted into ROOT-format. This is a one time process done at the end of data taking periods. The analysis scheme is of course the same as in the NQ-software. There are data structures for hits, clusters of hits, particles, etc. corresponding to the different stages of analysis. The use of an object oriented programming language and the ROOT package offers many practical, even though not principal advantages. ROOT has a lot of features that PAW is missing. The main disadvantages of SASYSOFT are that all data has to be converted and that ROOT does not run on the VMS operating system which is used on most computers in the LEGS group. Also replay of the data is slower in SASYSOFT than in NQ.

The use of different analysis software for the same tasks provides a useful consistency check. Both NQ and SASYSOFT give identical physics results after all bugs in the software are removed.

6.4 Monte Carlo

Without a detailed Monte Carlo model of the detector system a meaningful analysis of the data is virtually impossible. Also in the design stage of the experiment Monte Carlo simulations have been very useful to study the performance of SASY. The Monte Carlo simulation was developed at Virginia Tech and is based on GEANT 3.21. The full geometry of all SASY detectors is implemented and different versions for the details of the detector setup can be selected, e.g. the type of target cell or the position of the light guides for the xtal box veto paddles. The Monte Carlo simulation can be run to create events for later analysis with NQ or SASYSOFT, it can analyze the events it creates, or it can analyze events read from a file. Because the Monte Carlo model was developed in the design stage of the

experiment, it uses its own file format. Data can be converted from MC format for replay with the other software packages. Also data from the experiment can be converted to the MC format to make use of the analysis subroutines in the Monte Carlo software.

The Monte Carlo simulation was used for the adc calibrations, to determine efficiencies, and to account for the gaps in solid angle coverage of the detector. It will be mentioned many times below.

6.5 Data preprocessing

The raw experimental data contains buffers as described in section 4.9.2. The first step in processing the data is to 'strip' the data files of bad buffers. Bad buffers are buffers that contain data with FERA errors. This means that the data recorded in some events of this buffer cannot be decoded to the correct detector elements. If even one event in a buffer has a FERA error, the whole buffer is discarded. The buffers that pass this low level consistency test are written to the stripped data file.

To decrease replay time of the data set, subsets are created for different tasks. For example the calibration of the xtal box cannot depend on events where the xtal box was not hit. The count rate in the xtal box is much lower than that in the pn bars. Creating a subset of the data that contains only events with at least one hit in the xtal box thus reduces the replay of 'useless' events during calibration of the xtal box. Also the beam flux monitor events are stripped out into their own files as they are used for a specific purpose only. Furthermore the data can be stripped of events that have only electrons as identified in E-dE plots. Such a reduction in background events increases the analysis speed, but it bears the risk of cutting too much of the data at too early a stage of the analysis. Final results have always been checked against the unstripped, original data files to ensure that in the stripping no good events got lost.

6.5.1 Data format conversion

If experimental data is to be replayed by a software other than the NQ-software or Monte Carlo data by software other than the MC-software, it has to be converted into the file format for the software package to be used. There is a set of data format conversion utilities. Conversion of the data is loss free. The file formats are different, but the logical content of the files is the same in each format with the exception that raw detector data cannot be converted into Monte Carlo format as the latter requires calibrated data (energies and times).

Chapter 7

Calibration procedures for the SASY detector system

7.1 Introduction

The experiment records detector signals in the form of adc- and tdc-values. These signals have to be calibrated, i.e. converted into units of energy and time, before a meaningful analysis of the data is possible. Here the various steps of this process are described.

7.2 Timing calibrations

7.2.1 Introduction

The TDCs in the SASY detector setup are used to measure time of flight (tof) of particles from the target to the detector to allow particle discrimination and energy measurements for nucleons. Depending on which detector subsystems are hit and on the reaction that caused the event, the time that elapses between an event happening in the target and the triggering of the electronics (and thus the start of all the tdc's) varies. For this reason a single tdc cannot give the right time of flight. However, the time of the tagger hit is related to the event happening in the target through a constant offset because the photons travel down the beam pipe at the speed of light and the electrons also practically move at the speed of light to the tagger. The hit of the electron in the tagger serves as a start for the time of flight measurements, independent of where in the straight section the Compton scattering occurred and only smeared by the length of the electron bunches in the NSLS storage ring. The stop signals for the time of flight measurements are of course the tdc's on each of the detector elements. The difference of the calibrated detector element tdc and the tagger tdc

is the time of flight of the particle:

$$tof^{hit} = t^{detectorelement} - t^{tag} \quad (7.1)$$

The second purpose of the tagger tdc's is to discriminate events in the true peak and the accidental peaks as described in chapter 8. If an accidental hit in the tagger is analyzed the time of flight of all particles needs to be shifted by an integer multiple of 18.9 ns depending on the accidental bunch.

We verified that all tdc's are linear, i.e. that an equal amount of tdc channels corresponds to an equal amount of time passed, regardless of where within the dynamic range of 2048 channels the time start and end pulses occur.

7.2.2 Tagger

The tagger tdc's are started by the event trigger and stopped by the delayed signals from each of the tagger channels. If a channel is not hit, the tdc will not be stopped and no data will be recorded for that channel.

The rf of the NSLS storage ring is known precisely. This together with the true/accidental structure of the tagger spectrum makes the tagger tdc calibration easy. The peaks of each of the true and the following three accidental peaks are fitted in each of the 64 raw tdc histograms. The calibration formula for the tagger time

$$t_i^{tag} = a_i^{tag} \times tdc_i^{tag} + b_i^{tag} \quad (7.2)$$

contains the dispersions a_i^{tag} and offsets b_i^{tag} ($1 \leq i \leq 64$). The dispersion of the tdc's is calibrated to reproduce the spacing of 18.9 ns between peaks, corresponding to the rf of the NSLS. The offsets are adjusted to line up all the different tagger channels to a common and arbitrary time chosen such that $t = 0$ is the center of the true peak.

In April 2000 the Cherenkov detector to improve the tagger time resolution was installed. It's calibration is completely analogous to the other tagger elements.

The dispersion of the tagger tdc's is 55 to 60 ps per tdc channel.

7.2.3 pn bars

For the pn bars the first step in the tdc calibrations is a slew correction. This correction takes into account the dependence of the tdc data on the signal height. For small signals the discriminator threshold is reached later than for bigger signals. To compensate for this effect the adc signal is used when converting tdc channels into time in ns:

$$t_i^{pn1/2} = a_i^{pn1/2} \times tdc_i^{pn1/2} + \frac{b_i^{pn1/2}}{\sqrt{adc_i^{pn1/2}}} \quad (7.3)$$

Here t is the calibrated time in ns, the subscripts 1 and 2 refer to the different sides of each pn bar, the a s and b s are the calibration constants, and the pedestal offsets are added to the adc values. The dispersion a for each tdc is measured offline using short delay cables. The functional form for the slew correction was found to give good results over the whole range of signal heights and the b -parameters are fit to make t independent of signal height. The slew correction is based on electrons that hit the bars in a narrow range near the photo multiplier to be calibrated in order to select events with a constant time (making use of the fact that electrons are relativistic at all energies encountered in the SASY detector). The tagger time has to be subtracted from this to account for the different event trigger timing of different events.

For the pn bars the signals from both ends of the bar have to be combined to give x-position and tof measurements. The position is calibrated as

$$x_i^{pn} = (t_i^{pn1} - t_i^{pn2}) \times c_i^{pn} + d_i^{pn} \quad (7.4)$$

where c is the speed of light in the scintillator and d is an offset. Though not mentioned previously, there were also six finger counters made of 0.635 cm square plastic scintillator running the full height of the bars and equally spaced in the x direction. In z they are located a few cm in front of the pn bars at $z = 85.6$ cm. These are used for the position calibration. Electrons are not useful here because they scatter too much. Charged pions and protons (selected through an E-dE cut) give straight tracks such that the position of the hit on the pn bar counter can be calculated from geometry. Further constraints on the position calibration could be obtained from tracks of cosmic muons through the pn bars. Using the position in each bar that was hit a straight line can be fit to the track. Then for each bar the deviation of the hit in this bar from the track position can be calculated and through iteration the offsets of different bars can be calibrated together. Taking into account that cosmic events should evenly fill the whole range of the bar from +80 cm to -80 cm the position could be calibrated using cosmic events alone.

For the November 1999 data set it was found that cross talk in repeater modules in the tdc signal chain caused shifts in the measured x-position relative to the true position that causes peaks in the x-position spectrum of cosmic events (see figure 7.1). If two channels that are next to each other on the circuit board are hit within a few nanosecond of each other the relative timing of the signals is not preserved in these repeater modules. The repeater modules were used to reshape the signals after delaying them on their way to the tdc's to gain time for the trigger logic. The data could not be corrected for this effect and it is taken into account as a worse position resolution than could have been achieved otherwise.

Before the April 2000 data runs the hardware had been modified to avoid the cross talk problem by changing the cabling such that signals will never pass through nearby channels of the repeaters at the same time for events that hit only a few bars. Cosmic events that hit many bars will still exhibit the cross talk. This is not a problem because the use of cosmic events is largely restricted to energy calibrations and they are not needed in the x position calibration.

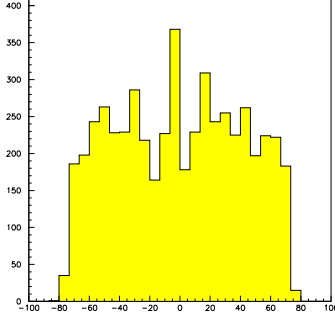


Figure 7.1: Crosstalk in the pn bars: The x-position histogram from cosmic ray tracks should be filled uniformly without any structure. The peaks are due to the cross talk in the repeater modules. A similar structure is seen in all bars.

To get the right time of flight for each pn bar an offset e has to be determined in the equation:

$$t_i^{pn} = \frac{t_i^{pn1} + t_i^{pn2}}{2} + e_i^{pn} \quad (7.5)$$

With knowledge of the position of a hit its time of flight is known for relativistic electrons. In the November 1999 data set the cross talk effects on the time of flight are taken into account through the tof resolution.

bar veto paddles

The veto paddles for charged particle identification are calibrated in the same way as the other pn bars. The two short veto paddles on either side of the hole for the beam are the exception. Even though the tdc information is recorded in the data stream, it is not useful. Neither the position nor the tof of a hit can be reconstructed for these veto paddles.

7.2.4 Lead Glass

The tdc calibration for the PbG detectors consists of three steps: determination of the dispersion a for each tdc, the slew correction as for the pn bars (parameter b), and the subsequent fit of the offsets c to shift photons to $\beta = 1$ in the tof spectra.

$$t_i^{pb} = a_i^{pb} \times tdc_i^{pb} + \frac{b_i^{pb}}{\sqrt{adc_i^{pb}}} + c_i^{pb} \quad (7.6)$$

7.2.5 Trigger tdc

There are three tdc in the data stream that do not correspond to any one detector element. Rather there is one tdc for each of the sub-detectors (xtal box, pn bars, and PbGlass). These tdc get stopped by the fastest channel of each sub-detector group. They provide a convenient way to check, if a particular detector group was hit in an event and further help to adjust the accidental spectrum in the tagger to get more narrow true and accidental peaks. These tdc show a sharp peak for events in which their sub-detector was the only one hit. If another sub-detector was hit as well, only one of them can have started the trigger. In this case the other tdc records a different time with the details of the spectrum depending on the frequency of hits in all the detectors and the details of which detector is delayed by exactly what time. The dispersions for these three tdc are calibrated with cables of known delay and the peaks are shifted to $t = 0$ with offsets.

The effect of these tdc on the true/accidental spectrum of the tagger is minor. Even without their use the true and accidental peaks are cleanly separated. However, in some cases they are useful. If a pn bar starts the trigger, because it has a shorter signal path than all the xtal box elements hit, it will determine the position in the true/accidental histogram. The position will be shifted from the center of the peak by the time of flight of the particle. If this is a nucleon then the shift may be large, with the result of putting good true events into the accidental peak preceding the true peak. Taking the difference of the trigger tdc times for the pn bar and the xtal box hits the true/accidental spectrum can be made as if the box had caused the trigger. For this tof effects are small because the xtal box is closer to the target. The different cable length for each of the detector elements in each of the sub-detectors are taken into account by fitting a tagger-offset for each detector element based on a true/accidental histogram with events in which this detector element had a single hit and no other detectors were hit.

7.2.6 tdc calibration tests

The information from the tdc in this experiment is used in many ways. The most important piece of information, which is also most sensitive to the tdc calibration and resolution, is the measurement of a particle's velocity for particle identification and energy determination in the case of neutrons. The 'reduced time of flight', also named 'inverse beta' of a particle is calculated from the position of the hit in the detector and the time of flight as:

$$rtof = \frac{tof}{\sqrt{x^2 + y^2 + z^2}} \quad (7.7)$$

The spectrum of the reduced time of flight should show a peak at exactly $rtof = 1.0$ for photons and relativistic electrons with a tail to larger $rtof$ for charged pions and a clearly separate broad peak at $rtof \approx 2$ to 7 for nucleons. This spectrum was produced with cuts placed on the tagger channel, on the pn-bar that was hit, and on the range of x in the

bar. The photon peak always has to be at $rtof = 1.0$. In this way inconsistencies in the calibration could be identified and eliminated.

7.3 Energy calibrations

7.3.1 Introduction

Whereas the calibration of the tdcs in this experiment could proceed rather straight forward and independent of external input, relying only on the data itself, the energy calibrations require Monte Carlo input and other information. Furthermore the calibration of all the SASY detectors depends on the tagger energy calibration and any error in the tagger calibration will severely impact the data analysis at every stage from calibrations to final results.

7.3.2 Tagger

There are three different methods of calibration for the tagger energies. As described in chapter 2, laser lines of different wavelength ranging from 263 nm to 514 nm can be used to make the photon beam. The Compton edges from these laser lines lie in different positions on the focal plane of the tagger. By recording tagger hits with beam produced through various laser lines and using the same mode and energy setting of the tagger, different photon energies can be directly assigned to the tag channel that the edges fall on to. The energy of a photon edge is only a function of the NSLS electron ring energy and the wavelength of the laser. If enough Compton edges fall onto the tagger focal plane, interpolation with a suitable function (e.g. second or third order polynomial) can give a calibration in an unambiguous way. This method suffers if the tagger is operated in a mode such that only a few Compton edges fall on the focal plane. In this case interpolation over a large range of tagger channels may be necessary and worse, if there are no Compton edges near the low energy end of the tagger, the calibration of the high tagger channels (corresponding to the low energies) is based on extrapolation of the unknown functional form of the calibration curve.

The second method gives the beam energy for all tagger channels. We are interested in finding the change of photon energy (or equivalently: change in electron energy) dE with change in position on the Tagger focal plane dx . The bremsstrahlung spectrum in the tagger, the number of hits $N(x)$ in the tagger channel at position x on the focal plane, can easily be recorded. This gives $\frac{dN}{dx}$. For a thin target, which is given in the low vacuum of the NSLS storage ring, $\frac{dN}{dE}$ can be computed precisely from QED. We can compute $\frac{dE}{dx} = \frac{dN}{dx} / \frac{dN}{dE}$ and need to use the absolute energy from only one of the Compton edges to shift the calibration curve obtained from the bremsstrahlung spectrum to the right absolute energy. The result for the tagger channels with Compton edges from other laser lines must then agree with the energy computed from these lines. This provides an inherent test for this calibration. (In

practice of course the energy is shifted to minimize the RMS deviation from all the available Compton edges.) This method was used successfully many times at LEGS. However, in November 1999 and April 2000 the dispersion from bremsstrahlung did not result in good agreement with all the Compton edges. The reason for this was ascribed to scattering of electrons from the region of the beam pipe where the tagger pipe splits from the NSLS ring. This 'crotch scattering' superposes and distorts the true bremsstrahlung signal, if the electron orbit is not well controlled or the tagger slits not adjusted properly.

A third method to calibrate the tagger uses knowledge of the magnetic fields throughout the path of electrons from the storage ring through the tagger magnets to the focal plane to do ray tracing of the electron trajectories. This also requires knowledge of the NSLS storage ring energy. The ray tracing usually gives results that are not in agreement with observation. This is attributed to insufficient knowledge of the magnetic fields especially in the region of the D1 magnet which is part of the storage ring and controlled by the NSLS rather than by the LEGS group. More work would be required to turn this method into a practical way of calibrating the tagger.

It is important to note that the NSLS electron ring energy is an input to any of the three calibration methods mentioned above. The storage ring energy cannot be determined independently with the above methods. Also it should be noted that, especially for the first calibration method, there is little room for a large error in the tagger calibration for the tagger channels that the Compton edges fall on.

The first tagger calibrations for the November 1999 and April 2000 data sets were derived from the first method, but taking the bremsstrahlung spectrum into account to choose the functional form to fit to the Compton edges. For the April 2000 data sets this turned out to be wrong because the actual NSLS ring energy was different from its nominal value. In the next subsections it is described how it was found that the actual ring energy was different from the nominal one and how the tagger calibration was modified to reflect this change.

Evidence for a deviation of the NSLS storage ring energy from its nominal value

There are two independent problems in the data identified by the author that can not be explained without assuming the first tagger calibration to be wrong. The first problem shows that the first tagger calibrations for the November 1999 and April 2000 data sets can not both be correct. The range of photon energies overlaps for the nov99hd and apr00hduv data sets. The energy deposited in the xtal box by charged pions created in reactions with photons of the same energy must be the same in November 1999 and April 2000 (ignoring the very minor differences in energy loss due to the slightly different target). Even without a xtal box energy calibration we can compare the adc signals for single hits (i.e. the pion hits only one xtal box crystal) by adjusting for possible gain drifts between the data sets with cosmic ray signals. The position of the peaks in the resulting (gain-corrected) adc spectra is consistently lower in the apr00uv data by $\sim 10\%$ compared to the nov99hd data. The

gain corrections themselves are small (less than 10%) and the error on the gain corrections is completely negligible after averaging over many xtal box counters. To select pions and suppress electrons we place an E-dE cut in the xtal box. This does not introduce a bias and the result is insensitive to the exact shape of the cut. The spectrum can be cleaned further by demanding a neutron in the pn bars (i.e. no pn bar veto and a bar hit with $rtof > 1.5$). This does not change the result. The result is also independent of which region in the xtal box we look at. The peak in the adc spectrum always has some background under it. This is due to the Fermi smearing of the energy in reactions on the deuteron. The peak can always be identified to much better than the observed shift of $\sim 10\%$. The two different data sets from April 2000, apr00hd and apr00hduv, also have overlapping photon energy ranges. The position of adc peaks for these two data sets agree for tagger channels with the same energy, showing that the two tagger calibrations for the different settings in April 2000 are consistent with each other, but not necessarily right.

The second inconsistency in the data can be observed in each of the data sets independently. The kinetic energy of neutrons T_n observed in the pn bars can be calculated from their measured tof and position of hit. This determination of the neutron kinetic energy $T_n(rtof)$ relies only on the timing calibration of the pn bars. This calibration (as described in 7.2.3) is entirely independent from the tagger energy calibration. On the other hand the kinetic energy can be calculated for neutrons from $\gamma p \rightarrow \pi^+ n$ from the incident photon energy E_γ and the neutron angle θ_n using two body kinematics. This $T_n(E_\gamma, \theta_n)$ may give the wrong answer, if the reaction happened on a bound proton inside the deuteron, but should agree with $T_n(rtof)$ otherwise after taking into account shifts of the peak in the $T_n(rtof)$ spectrum that arise due to the limited resolution of the tof and x position measurements. These shifts are explained in more detail in the next subsection. After correcting for the shift due to resolution, the difference $T_n(E_\gamma, \theta_n) - T_n(rtof)$ peaks at 0 for the November 1999 data, as expected. For the April 2000 data sets the difference is non-zero. Detailed checks of the pn bar calibration and analysis of possible errors from the cross talk that affects the position calibration as well as errors from other sources (e.g. wrong target position) have found that no other effect than a wrong tagger calibration can account for a difference between $T_n(rtof)$ and $T_n(E_\gamma, \theta_n)$

Having identified the tagger calibration as the source of the difference, we have to identify the reason why the first tagger calibration for April 2000 was wrong. Especially for the first calibration method mentioned above, there is little room for a large error in the tagger calibration for the tagger channels that the Compton edges fall on. It can be verified that the data was taken at the same tagger settings that the tagger calibration was done at, with shifts of the tagger spectrum from run to run of much less than one tagger channel. The algorithm used to determine the positions of the Compton edges can introduce a small bias, again much smaller than one tagger channel. The energy of the photons from the laser is known with high accuracy. The only other possible source of error is the NSLS electron beam energy.

The NSLS storage ring is designed to provide high luminosity synchrotron radiation to users

at the beam lines. In order for the beam current to stay as high as possible between fills it is desirable to keep electrons in the ring for a large range of energies. For the synchrotron light users it is not important to know the beam energy precisely. It is quite possible that the NSLS could operate at an energy different from the nominal by a large fraction without any of the other users noticing or caring.

In November 1999 the NSLS operated the x-ray ring at 2800 MeV for the first time. In April 2000 one of the sextupole magnets in the x-ray ring was installed with wrong polarity. This caused problems with the orbit, resulting in operations at a beam energy lowered from 2800 MeV and with an orbit different from the operations at 2584 MeV before the year 2000.

Determination of the NSLS storage ring energy with data available

Both of the observations made above can be used to extract information about the actual electron ring energy. Matching the gain-corrected adc spectra of pions from the November 1999 data set with those from the April 2000 data set allows one to identify pairs of tagger channels that corresponded to the same photon energy. For example, tagger channel 12 in apr00hduv had the same energy as channel 34 in nov99hd. This relation between the different tagger calibrations plus use of the Compton edges from three different tagger settings enables a fit of the a priori two unknown electron ring energies simultaneously.

Much more useful is the second observation on the neutron kinetic energy. The photon energy can be calculated from measurement of neutron tof and position. The first equation follows from two-body kinematics. The second equation shows the kinetic energy of the neutron as a function of it's time of flight

$$E_\gamma(T_n, \theta_n) = \frac{1}{2} \frac{2m_p T_n + m_\pi^2 - (m_n - m_p)^2}{\sqrt{T_n^2 + 2m_n T_n \cos \theta_n} - T_n - (m_n - m_p)} \quad (7.8)$$

$$T_n(tof, x) = m_n \left(\frac{1}{\sqrt{1 - \left(\frac{\sqrt{x^2 + y_{pn}^2 + z_{pn}^2}}{tof} \right)^2}} - 1 \right) \quad (7.9)$$

Here m_n , m_p , and m_π are the mass of the neutron, proton, and charged pion, respectively. y_{pn} and z_{pn} are the position of the pn-bar that was hit by the neutron. tof and x are measured in the pn-bar. The neutron angle θ_n is calculated from the coordinates of the hit.

This determination of the photon energy is very sensitive to the neutron time of flight measurement. An error in the neutron time of flight of 0.1 ns results in an error of the photon energy of up to 4 MeV, with larger errors for the higher photon energies and lower errors for the lower energies. The x-position determination is important, too. Here the error in the photon energies is 4 MeV per centimeter in x for the ends of the bars and it falls to zero for the center of the bars.

With the strong dependence of the reconstructed photon energy on the time measurements in the pn bars, any systematic shifts in the tof or position calculated from the pn bar tdc signals could shift the reconstructed electron ring energy by a large amount. It is necessary to examine the effects of such a systematic, the cross talk in the November 1999 data set, in more detail. The cross talk between the adjacent channels in the repeater modules is due to image currents induced in the neighboring (and to a lesser extent the next to neighboring) channels during rise and fall of a signal. The rise time of the signals at the repeaters is ~ 2 ns. The maximum amplitude of the signals induced in the neighboring channels is 25% of the threshold to create the output pulse on the repeater module. So the maximum shift of the timing of one channel due to the presence of another channel is ~ 0.5 ns. Since each of two channels may affect the timing of the other one, the maximum shift in the time-difference of two channels is 1.0 ns. This corresponds to a shift of position in the pn-bars of ~ 10 cm. However, this is the maximum shift due to the cross talk. Mapping the cross talk for a few pairs of channels explicitly, we find that the shift usually does not exceed 5 cm. In the x-position spectra of each single pn-bar it can be seen that there are systematic shifts that would change the measured angle θ_n . However, taking an average over all bars, the shift is basically random and no systematic error is introduced. The sum of all image currents in neighboring channels must be zero. However, this does not imply that the shifts towards later times equal the shifts to earlier times, because the timing of the output signal depends on the threshold of discrimination and the distribution of positive and negative image currents is not symmetric. For differences of the input times on two neighboring channels between -4 ns and $+4$ ns there can be an average delay in the sum of the output signals of about 1 ns relative to the sum of the times at which the outputs would have occurred without the cross-talk. However, the shift in the time of flight is just an offset that is independent of the absolute time of flight. It is the same for slow neutrons and fast electrons. It only depends on the position of the hit in the bar, as this is the only variable that determines the relative timing of the signals from each end of the bar. This means that the shift due to the cross talk is calibrated away when the offsets for the time of flight calibration in equation 7.5 are determined. In conclusion, there is no evidence for a systematic effect due to the cross talk.

The neutron kinetic energy is derived from the measured quantities in the pn bars. The measured tof and x-position in the bars have experimental resolutions. Since the dependence of the neutron energy on the measured quantities is nonlinear (formula 7.9) the peak of the resulting neutron energy distribution for each pair of tof and x distributions is shifted relative to the value calculated from the central values of these tof and x distributions. This can be modeled using a Monte Carlo (MC) simulation with the correct parameters for the experimental resolution (see chapter 10 for a description of the resolutions). For the April 2000 data set this is a relatively small effect, as the tof of neutrons is long for the smaller photon beam energies and the resolutions in tof and x of the pn bars are much improved due to the reduction of cross talk in the pn bars. The effect is illustrated in figure 7.2, where the difference of neutron kinetic energy calculated from tof and x in the pn bars with the Monte Carlo privileged information is plotted against the beam energy (beam energy is plotted as tagger channel) for a Monte Carlo simulation of charged pion production on the protons in

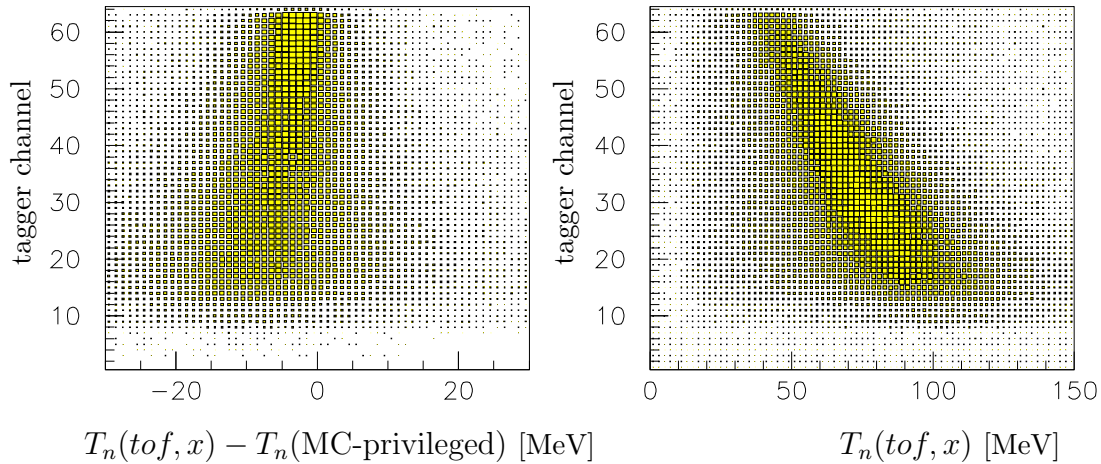


Figure 7.2: left: $T_n(tof, x) - T_n(\text{MC-privileged})$ vs. tagger channel (Monte Carlo simulation of Nov99 data); right: $T_n(tof, x)$ vs. tagger channel for Nov99 data

HD for the November 1999 setup. Further the neutron kinetic energy calculated from tof and x of actual data is plotted. This scatterplot is well reproduced by the MC simulation with the right resolutions. The photon beam energy reconstructed from tof and x in MC is compared to the input beam energy of the MC to obtain the correction due to the shift from resolution. This correction is added to the photon beam energy measured from tof and x in the bars for data. It is less than 15 MeV over the entire range of beam energies. With the correction the photon beam energy from neutron tof and x agrees with the calibration from Compton edges, shown in table 7.1. The electron ring energy for November 1999 was thus found to be consistent with its nominal value of 2800 MeV.

The electron ring energy for April 2000 was fitted by minimizing the RMS deviation of the photon energies at all available Compton edges from the photon energies determined for the same tagger channels from neutron kinematics and from the signals of charged pions in the xtal box based on the November 1999 calibration. These two independent methods give tagger calibrations that agree with each other, giving additional confidence that the result is correct. The NSLS ring energy in April 2000 was $2555\text{MeV} \pm 10\text{MeV}$, resulting in the calibration for the data taken with the 488nm laser line shown in table 7.1. The data taken in MLUV laser mode has been calibrated in the same way. However, since it is not used in the final physics results and only served for cross checks between the data sets, its calibration is not listed here.

tag ch.	Nov99 [MeV]	Apr00 (vis) [MeV]	tag ch.	Nov99 [MeV]	Apr00 (vis) [MeV]
1	405.8	310.0	33	307.4	238.0
2	402.0	307.4	34	304.9	236.0
3	398.3	304.7	35	302.4	234.0
4	394.6	302.1	36	299.9	232.1
5	391.0	299.5	37	297.5	230.1
6	387.4	297.0	38	295.1	228.1
7	383.9	294.4	39	292.7	226.1
8	380.4	292.0	40	290.3	224.2
9	377.0	289.5	41	287.9	222.2
10	373.6	287.1	42	285.6	220.2
11	370.3	284.8	43	283.2	218.2
12	367.1	282.4	44	280.9	216.2
13	363.8	280.1	45	278.6	214.2
14	360.7	277.8	46	276.3	212.2
15	357.5	275.5	47	274.0	210.2
16	354.4	273.3	48	271.7	208.1
17	351.4	271.1	49	269.5	206.1
18	348.4	268.9	50	267.2	204.0
19	345.4	266.7	51	264.9	201.9
20	342.5	264.6	52	262.7	199.9
21	339.6	262.4	53	260.4	197.7
22	336.7	260.3	54	258.1	195.6
23	333.9	258.2	55	255.9	193.5
24	331.1	256.2	56	253.6	191.3
25	328.3	254.1	57	251.4	189.1
26	325.6	252.0	58	249.1	186.9
27	322.9	250.0	59	246.9	184.6
28	320.3	248.0	60	244.6	182.4
29	317.6	246.0	61	242.3	180.1
30	315.0	244.0	62	240.1	177.8
31	312.5	242.0	63	237.8	175.4
32	309.9	240.0	64	235.5	173.0

Table 7.1: Tagger energy calibrations

Determination of the NSLS storage ring energy for future runs

In order to avoid the problem of not knowing the tagger calibration for future data taking periods, it is highly desirable to measure the storage ring energy directly to better than 5MeV uncertainty. There are different methods to do this measurement. An obvious choice may be to use a neutron energy measurement as mentioned above. In order to reduce the uncertainty in the neutron energy one would need to increase the flight path of neutrons from a target to the detector. However, with increased distance the solid angle coverage of the detector diminishes, assuming a detector of the same size. This leads to impractically long running times in order to collect a sufficient number of neutrons with a pion in coincidence. It is not easy to get a small error on the tagger energy this way.

The electron ring energy can also be measured using Compton kinematics. The scattered photons need to be detected at small forward angles. This method was used at LEGS previously and can result in a determination of the ring energy to ~ 15 MeV uncertainty.

A third method, used at other facilities to achieve errors of only ~ 1 MeV [23], makes use of the polarization asymmetry of circularly polarized photons scattered from linearly polarized electrons to measure the $g - 2$ depolarization resonance of the electrons in the synchrotron ring. The electrons in the ring self-polarize transverse to the plane of the synchrotron ring. For the NSLS the polarization builds up within approximately one half hour after injection of the beam. With an rf cavity in the electron ring the difference between the frequency of the ring and a nearby integer multiple of the $g - 2$ frequency could be coupled in to observe the electron depolarization. Alternatively (and without the need to install a new rf cavity) the ring could be operated at the energy of the sixth harmonic of $g - 2$ ($6 \times 440.652 \text{ MeV}$) during a studies shift. The nominal beam energy could be related to this energy through the dependence of beam energy to power supplied to the synchrotron, if the power supplies can be monitored accurately enough. A considerable complication in this method is the existence of synchrotron resonances at a spacing of just 1.2 MeV in the NSLS x-ray ring, a problem other synchrotrons with different working parameters do not have. These resonances depolarize the electrons, not to the extent of the $g - 2$ resonance, but will harm the sensitivity of the measurement. No matter what method will ultimately be chosen to measure the electron ring energy, investment of time, effort, and money is needed to solve this problem.

7.3.3 Xtal Box

General Considerations

The energy of particles is measured in SASY to identify particles based on EdE signature and to place energy thresholds on all detectors for a consistent detector acceptance determination.

The adcs for the xtal box, as well as for the pn bars and lead glass, give a measure of the amount of light that hit the photo-multipliers. Not all the kinetic energy of a particle is

converted to light in the spectral range that the photo-multipliers are sensitive to. We have to distinguish between the energy deposited in the counter and the light seen by the photo-multiplier. The conversion function $\frac{dL}{dE}$, the fraction of deposited energy E that is detected as light L , depends on the type of particle that interacts with the scintillator and the initial energy of this particle. Further there are other effects. For photons the shower created in the scintillators may not be fully contained. The energy of a photon may seem lower than it actually is due to this shower leakage. On the other hand some of the charged pions may decay into muons and neutrinos within the gate time of the adc and light from the muon can be recorded, resulting in a seemingly higher energy of the pion.

The final states of interest for charged pion production do not include photons and thus a description of their treatment is omitted here. Photons are created in neutral pion production from the π^0 , but for the purpose of this analysis they are easily rejected using the veto paddles. The particles of interest are charged pions, protons, and neutrons. The neutron detection efficiency of the xtal box is too low to include reactions with a neutron in the final state where the neutron hits the xtal box. Neutrons are detected in the pn bars only. This leaves the task of calibrating the adcs of the xtal box for charged pions and for protons.

One way to calibrate the energy of detectors is through the use of kinematically overdetermined reactions. This requires knowledge of the initial state and of the angles of the final state particles to calculate the energy of the final state particles. In the case of SASY with the SPHICE target there are several limitations to this approach. Detection of all particles in the final state severely cuts the number of events compared to the case of detecting only one particle. Also the Fermi smearing inside the Deuteron causes deviations of the energy of the final state particles from that expected by measurement of their angles. This could only be overcome if the spectator nucleon in a reaction on Deuteron could be detected. This is impossible because the spectator has not enough energy to leave the target.

Instead the calibration relies on a Monte Carlo simulation to predict the light seen in the detectors for charged pion productions with photons of given energy. These spectra are compared to the adc spectra produced with the same set of cuts as MC. A fit of MC energy versus data adc value determines the energy calibration. This is most easily done with single hit data, i.e. reactions in which the final particles hit at most one detector element, such that energy splitting between different detector elements does not need to be considered.

Due to the detector geometry some detector elements will not contain single hits. These are the xtal box elements near the edges of each face and in the corners. These detector elements are calibrated by adjusting their gain relative to the elements in the center of each face using signals from cosmic rays.

Calibration for charged pions and protons

The calibration is quite simple to the extent that the response of the detectors is linear. The first step is a relative calibration based on cosmic ray data to line up the peaks from cosmic ray muons. With sufficient statistics the quality of the fit to a Vavilov distribution is good. The overall scale of the calibration is set by using signals from charged pions selected in data through an EdE cut for pions from reactions of a certain beam energy. The same cuts on tag bin and EdE in the box are placed on the MC sample and the calibration coefficients a_i^{xt} in

$$E_i^{xt} = a_i^{xt} \times adc_i^{xt} \quad (7.10)$$

are adjusted so that data and MC agree in the amount of light E_i^{xt} produced in xt element i for each i . This procedure has a build in redundancy, because the calibration for different counters can be related through both cosmic ray signals and signals from reactions. If the two do not agree, there would be a problem with the MC simulation. In fact, good agreement was found.

The calibration can be done using all charged pions that hit the box. This will include negative pions from reactions on the neutrons in deuterium. Alternatively a coincidence with a neutron in the pn bars can be demanded, severely reducing statistics, but restricting the sample to positive pions. In this way the MC treatment of positive and negative pions can be compared. For the purpose of calibrations no difference between the two methods was observed.

If a particle gets identified as a proton, the differences in energy to light conversion between proton and pion are taken into account through a function that converts the pion-calibrated light into the correct number for the proton. This function was determined by comparing protons from a given photon beam energy in MC and data.

Care has been taken to examine possible nonlinear dependences of the energy calibration. These could arise due to nonlinearities in the electronics chain that amplifies and digitizes the signals. For this purpose equation 7.10 has been extended with a term proportional to the square of the adc value and an offset. The three free parameters have been fit using the peak positions of adc spectra from data and of the corresponding light spectra from MC for different incident photon energies. This results in data points for single crystal pion hits in the range of 50 MeV to 120 MeV for nov99hd and 20 MeV to 50 MeV for apr00hd for crystals in the center of each box face. No significant nonlinearity was observed for these counters. The linearity of detector elements near the edges of each face could not be tested well, as there are no single hits due to detector geometry. However, it is reasonable to assume that all detectors behave linear.

The xtal box corners

The xtal box corner counters are read out on both ends. The propagation of light in the scintillator is described using a uniform attenuation. A particle that deposits an amount of light E_i^{xc} in the corner scintillator i at z_i^{xc} produces signals at the up- and downstream ends of the scintillator of

$$E_{i,up}^{xc} = E_i^{xc} \times e^{\frac{0.5l+z_i^{xc}}{a}} \quad \text{and} \quad E_{i,down}^{xc} = E_i^{xc} \times e^{\frac{0.5l-z_i^{xc}}{a}} \quad (7.11)$$

with $l = 76.2$ cm being the length of the scintillator in z and a the light attenuation coefficient. Assuming the signals $adc_{i,up}^{xc}$ and $adc_{i,down}^{xc}$ to be proportional to the amounts of light $E_{i,up}^{xc}$ and $E_{i,down}^{xc}$, these two equations can be inverted to

$$E_i^{xc} = a_i^{xc} \times \sqrt{adc_{i,up}^{xc} \times adc_{i,down}^{xc}} \quad (7.12)$$

$$z_i^{xc} = b_i^{xc} + c_i^{xc} \times \ln \frac{adc_{i,up}^{xc}}{adc_{i,down}^{xc}} \quad (7.13)$$

The calibration constants a_i^{xc} , b_i^{xc} and c_i^{xc} can be determined using cosmic ray muons that hit detectors in one of the box corners and one full column of side face xtals. The position of the hit is then determined as a straight track at the z position of the hits in the side face of the box. The energy deposited is the same as that deposited in the box face counters that are hit, because the track passes through the same amount of scintillator for each of the detector elements.

The determination of position in the corner based on information from the adcs has a bad resolution due to the logarithmic dependence of the position on the ratio of the signals. A good resolution is not crucial in the xtal box corners. Usually a particle will hit a detector element at the edge of one of the box faces before entering a box corner and the position of the hit can be determined from the position of the corresponding hit in the box face.

In some events one end of a corner is hit without a signal at the opposite end. In this case we can either choose to ignore the hit and treat Monte Carlo data in the same way after placing a threshold on the minimum light seen at a phototube. Or we can process the hit with its position set to $\pm 0.5l$. i.e. at the end of the corner where a signal was seen, and the light of the hit calculated as

$$E_i^{xc} = a_{i,up/down}^{xc} adc_{i,up/down}^{xc} \quad (7.14)$$

where $a_{i,up}^{xc} \times a_{i,down}^{xc} = (a_i^{xc})^2$ and the two coefficients for the up- and downstream end are determined from hits of cosmic muons in the center of the corners (i.e. at $z = 0$) such that $\frac{a_{i,up}^{xc}}{a_{i,down}^{xc}} = \frac{adc_{i,up}^{xc}}{adc_{i,down}^{xc}}$. The results are insensitive to whether the single end corner hits are included or not.

The xtal box veto paddles

The charged particle veto paddles have been mentioned before. They are calibrated with a one parameter fit of the pion signal of pions of fixed energy to the energy from MC:

$$E_i^{xv} = a_i^{xv} \times adc_i^{xv} \quad (7.15)$$

The veto paddles are large in area and the readout is on one end. Due to attenuation of the light inside the scintillator particles of the same energy produce different signals depending on the position where they pass through the veto paddle. Another effect is that particles at $\theta_{lab} = 90^\circ$ travel a shorter distance d_0 in the scintillator than particles at larger or smaller angles, which travel through a distance $d = \frac{d_0}{\sin\theta}$ and thus can leave more light. d_0 is the thickness of the veto paddle. Both of these effects can be taken into account at a later stage in the analysis, when the information from the xtal box faces and the vetos is combined into hit clusters. These turn out to be small corrections that do not significantly improve the particle separation between pions and protons or pions and electrons. At the calibration stage it is not known where the paddle was hit and no corrections can be applied yet.

7.3.4 pn bars

The pn-bars give energy information through the adc readout of the two sides of each bar. We do not need to reconstruct position information from the adcs because the position determination from tdc information has a better resolution, even taking the cross talk problem in the November 1999 data sets into account. The energy is determined as

$$E_i^{pn} = a_i^{pn} \times \sqrt{adc_{i,left}^{pn} \times adc_{i,right}^{pn}} \quad (7.16)$$

The energy of all bars can be calibrated relative with cosmic rays by demanding hits in all bars of one layer at a given position in x. This ensures that the cosmic muon traversed the full height of each bar, traveling along the y direction. (Without the cut on x the muon could travel at an angle from, e.g. top left to bottom right of the bars, thus traveling a longer path inside each bar, broadening the peak in the spectrum.) Then the absolute scale is set through some appropriate reaction by comparison with MC. Protons or pions can be used with a cut on the x position of the hit and particle identification cuts in the EdE spectrum. The sharpest peaks are observed in the first layer of pn bars. The second and third layer can only get hit by high energy particles that also deposit energy in the first layer. The absolute scale of the calibration is set by hits in the first layer.

Hits in the pn bars with only one of the adcs above threshold can be treated analogous to the xtal box corners if only one end records data. However, this data will be at very low energies and not have tdc information usually, because the tdc discrimination threshold is slightly higher than the adc pedestal offset. Taking hits with one adc of a pn bar into consideration does not change the physics results.

bar veto paddles

The bar veto paddles are calibrated analogous to the pn bars, using protons of a given energy and comparison to MC to find the calibration coefficient a_i^{pv} in

$$E_i^{pv} = a_i^{pv} \times \sqrt{adc_{i,left}^{pv} \times adc_{i,right}^{pv}} \quad (7.17)$$

The two small veto paddles left and right of the hole for the beam are a special case. Here the optical connection between the two halves is missing and thus the light will be seen on only one end of the middle veto paddle. The energy in this case is determined as

$$E_i^{pv} = a_{i,left/right}^{pv} adc_{i,left/right}^{pv} \quad (7.18)$$

with $a_{i,left}^{pv}$ and $a_{i,right}^{pv}$ determined for particles that hit the paddle at $35 \text{ cm} < |x| < 40 \text{ cm}$, i.e. half way along the paddle's length. A correction of the light detected due to attenuation of the light in the scintillator can be applied based on knowledge of the position of the hit from its position in the layer of pn bars downstream of the bar veto paddles. This correction is small.

7.3.5 Lead Glass

The lead glass is used for photon detection only. It does not enter the analysis presented here. The calibration is similar to the calibration for photons in the xtal box, taking shower leakage into account. The calibration for photons is described in detail elsewhere [25].

7.4 Beam Flux calibration

The photon beam flux is measured with the photon counter CG3. There are two pieces of information from this detector. First, the total number of CG3 hits Y_{CG3} is counted in a scaler. Second, for a fraction of the counts the tagger tdc's are recorded. This allows assignment of the fractions f_i^{tag} of the flux for each tagger channel. For this the accidental subtracted yield n_i^{tag} is calculated for each tagger channel. Also the total number of times the tag tdc's are recorded, n_{total}^{tag} is counted. Then:

$$f_i^{tag} = \frac{n_i^{tag}}{n_{total}^{tag}} \quad (7.19)$$

To convert the yield in the photon counter into the photon beam flux, CG3 has to be calibrated. At a reduced beam rate a large NaI crystal (ten inch diameter, 14 inch length) is moved into the photon beam directly upstream of CG3. It is 100% efficient at the low beam

E_γ [MeV]	full HD target		empty target cell	
	0° pol.	90° pol.	0° pol.	90° pol.
244.2	4.81013e+09	5.24035e+09	1.22826e+09	1.32836e+09
261.8	6.09800e+09	6.45198e+09	1.57733e+09	1.66915e+09
280.1	6.94206e+09	7.18311e+09	1.77801e+09	1.84516e+09
299.1	8.27182e+09	8.44797e+09	2.10406e+09	2.15038e+09
319.5	1.08271e+10	1.09553e+10	2.72654e+09	2.79214e+09
341.7	1.36817e+10	1.37733e+10	3.41817e+09	3.48280e+09
362.5	8.13739e+09	8.61627e+09	2.06085e+09	2.19616e+09

Table 7.2: Photon beam flux in November 1999

rate, as verified by coincidence with the tagger. The count rate in this crystal is compared with the count rate in CG3 with the crystal moved back out of the beam, but with the beam flux unchanged. This yields a photon energy dependent CG3 efficiency $\epsilon_{CG3}(E_\gamma)$ that is assumed to be valid at the high beam rate of the normal experiment, too. This assumption is based on the fast response of the CG3 counters PCC and PCV, which are thin scintillators with fast photomultipliers. Over the range of energies of the November 1999 data set the CG3 efficiency varies from $\sim 6.0\%$ at the low energy end to $\sim 6.4\%$ for the highest photon energy.

For each polarization state the total flux in each tagger channel is:

$$N_{\gamma,i} = \frac{Y_{CG3}}{\epsilon_{CG3}(E_{\gamma,i})} \cdot f_i^{tag}, \quad (7.20)$$

where Y_{CG3} is the flux in CG3 and $E_{\gamma,i}$ is the central photon energy of tagger channel i . The total flux for each of the tagger bins (consisting of 8 tagger channels) used in the cross section and asymmetry determination for each polarization state is listed in table 7.2. The flux weighted average for the photon energy is given. These numbers have an error of 1% due to statistical uncertainty, precision of the calibration, and the possibility that small drifts in the gains of the photomultipliers may not have been correctly compensated at all times throughout the running period.

7.5 Target length determination

As described in section 3.3.2, the amount of HD gas is measured while making a target by measuring initial and final pressure in the gas reservoir. With the known properties of HD it is possible to calculate the target length. However, this method suffers from large uncertainty. If the HD does not form a uniform crystal more of the gas than expected may freeze near the outside of the target in the region shielded from the beam by the target ring.

Even though unlikely, there may be voids throughout the target. Finally temperature spikes during target transfer may evaporate some of the HD, which could refreeze in an inactive region of the target system.

Due to these uncertainties it is necessary to get an independent measurement of the target length. For this the breakup reaction of deuterium into a proton and nucleon is used. The world data set, consisting among others of measurements from LEGS and from Mainz, is in good agreement and the cross section for this reaction is known to better than 1%. The cross section has been parametrized by a fit to the world data set [24].

The breakup of deuterons produces high energy protons, unambiguously distinguishable in the xtal box from protons produced in pion production reactions. Protons from Compton scattering are kinematically restricted to the forward region of $\theta_{CM} < 75^\circ$ and thus do not cause a background for $\theta_{CM} > 80^\circ$. The resulting deuteron breakup cross sections reproduce the shape of the parametrization well (see figure 6.18 in section 6.7 of [25]). A fit of 40 data points to the parametrization gives the target length as 3.2 cm with an unbiased estimate uncertainty of 1.1% [25].

While many uncertainties in the cross section determination for the deuteron breakup are shared by the pion photo production (e.g. the beam flux) and thus do not contribute to the systematic error of the target length, there are different cuts placed on the data to select the high energy protons of the deuteron breakup than are used in the pion channels. This may be a source of systematic errors. The systematic error is estimated as 5.0%. Thus the total error on the target length is 5.9% and the target length is the largest source of error in the cross section determination.

Chapter 8

Correction for Accidental Hits in the Tagger

8.1 Introduction

A nuclear event is always caused by one photon hitting the target. If there are multiple hits in the Tagger for one event, it is ambiguous which of the tagger hits corresponds to the photon that reacted in the target. There are two ways to extract correct results from the data. The first possibility is to look only at those events with one hit in the tagger ('One hit analysis'). The second possibility is to subtract away the contribution of accidental hits in the tagger. Both analyses must give the same result within the statistical errors. For calibrations usually the simpler one hit analysis was chosen.

8.2 Accidental subtraction

The calibrated spectrum of the tagger tdc's is shown in figure 8.1. The high peak includes the true events (i.e. events that caused a trigger of the experiment). The smaller peaks at a distance of 18.9 ns each are due to accidental hits in the tagger from electron bunches other than the one that included the electron that the true hit in the tagger came from. The shape of the peaks changes depending on the cuts placed in SASY. The chance for an accidental hit in any electron bunch in the storage ring is equal. This means that the true peak has as many accidental events in it as any of the accidental peaks. Thus we can fill histograms for the accidental events from the three electron bunches following the true bunch, divide by a factor f and subtract these histograms from those filled by the events from the true bunch. The factor f would be equal to three, if all the bunches in the storage ring were filled. Due to the ratio of its circumference to the rf at which it operates the storage ring has 30 bunch

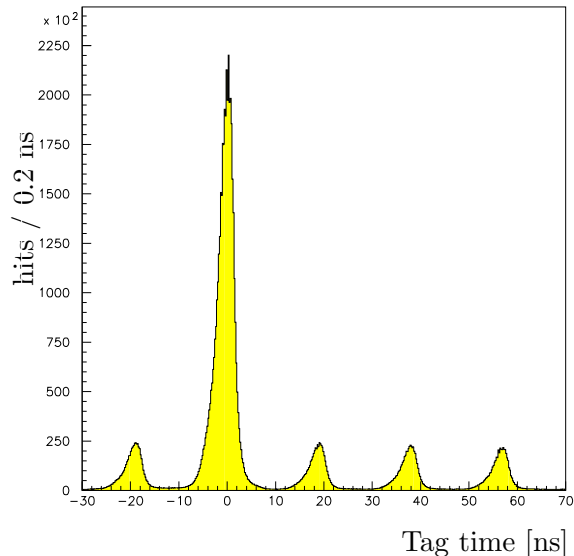


Figure 8.1: True-/Accidental- spectrum of the tagger

positions. However, to increase stability of operation only 25 of these bunch positions are filled, followed by five consecutive empty bunches. If a true event happens in one of the three bunches immediately before the empty bunches the chance for an accidental event in the next three bunches is reduced. A straight forward calculation of the probabilities for an accidental event in each of the bunches following the true bunch results in $f = 2.76$. Taking into account the possibility that the empty bunches are in fact not totally empty, one can calculate the right factor f as a function of the fill fraction e of the empty bunches defined as $e = \frac{\text{number of electrons in a empty bunch}}{\text{number of electrons in an full bunch}}$:

$$f(e) = \frac{(24 + 2e + 4e^2) + (23 + 4e + 3e^2) + (22 + 6e + 2e^2)}{25 + 5e} \quad (8.1)$$

In the nominator the first, second, and third term are due to the first, second, and third accidental bunches, respectively. The $5e$ in the denominator is due to the possibility of a true event happening from an 'empty' bunch. $f(e)$ is within ± 0.005 of $f(0) = 2.760$ for $e \leq 25\%$. Since the fraction e is not known precisely and the statistics on the accidental hits is low such that an uncertainty of 0.005 on f is negligible, the value $f = 2.76$ is used.

There are other corrections to f . Each of the 64 channels of the tagger is connected to a single hit tdc. If there is a second hit in the same tagger channel in one event (either an accidental hit after a true hit or even a true hit after an accidental hit in a previous bunch) it will not be recorded. The magnitude of this effect can be estimated by the fraction of coincidences of tag hits in two channels to the number of hits in one of these channels. It is small and we can neglect it.

Chapter 9

Empty Target Subtraction

9.1 Introduction

As briefly mentioned before (3.4), reactions can happen on the cooling wires and other parts of the target cell, giving a signal in addition to the signal from reactions on the HD. This contribution needs to be subtracted away. For this reason data is taken with the empty target cell and otherwise unchanged conditions to the HD run. The data of the empty target run is analyzed in the same way as the full target data, i.e. using the same set of cuts for particle identification, etc. The signal from the empty target run is then normalized to the same photon flux on target as the full target run and subtracted from the full target signal.

9.2 Comparison of HD and Empty Target spectra

The magnitude of the empty target subtraction as determined by the flux seen in CG3 results in a good approximation to the true scale of the normalization. However, the empty target cell may have shifted in the beam compared to the position during full target data taking. This can result in a different exposure of the empty target to the beam. Thus it may be necessary to apply a correction factor to the ratio of empty target run and full target run photon flux. This correction is determined using the very clean signature of deuteron breakup. The energy of protons from this reaction is completely kinematically determined. The Fermi smearing inside the deuteron is negligible here. The missing energy spectrum of the protons from deuteron breakup cannot have any tails on either side. Such tails could only be due to spallation of protons from the heavier empty target nucleons. The empty target correction factor is adjusted such that the missing energy spectra look clean. With a correction factor of 1.2 the spectra of figure 9.3 result. These spectra show the difference of the proton energy calculated from the detected angle and initial photon energy

for deuteron breakup kinematics and the energy deposited in the xtal box. No correction for the energy loss of the protons in the dead layers between the target and the xtal box is applied, causing the peak to be shifted from zero. There are no significant tails on either side of the distribution. The same spectra without any empty target subtraction and with the empty target subtraction scaled by the photon flux only are shown in figures 9.1 and 9.2 for comparison. The distribution of missing energy for the empty target signal is broad and shifted further from zero, as expected for events on heavy nuclei where Fermi motion of nucleons is large and an excited final nucleus can retain some of the energy.

In summary, the empty target subtraction works well. In the following chapters all spectra will show the empty target subtracted data from HD only.

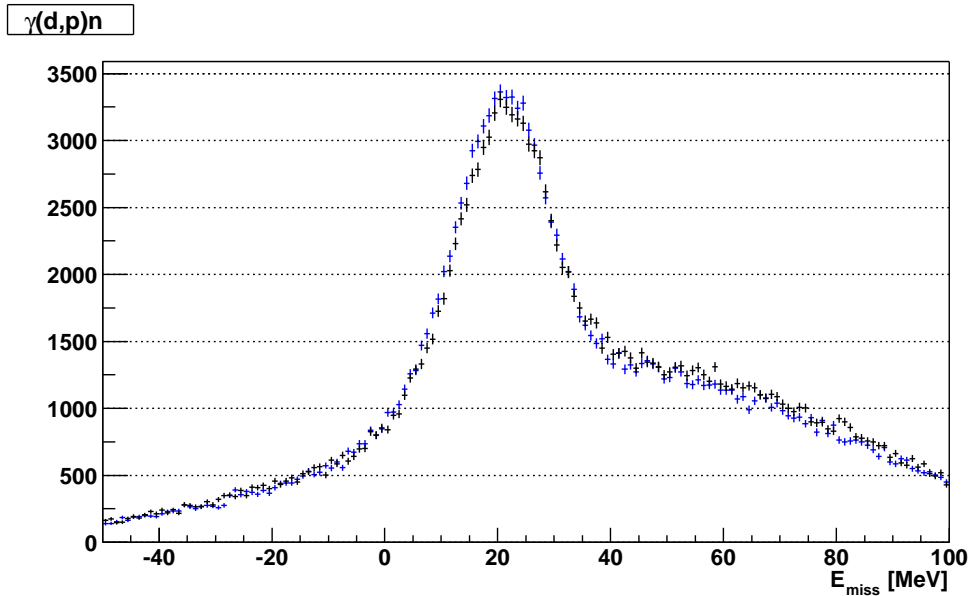


Figure 9.1: Missing energy of protons from deuteron breakup without empty target subtraction, for each polarization state (blue and black points).

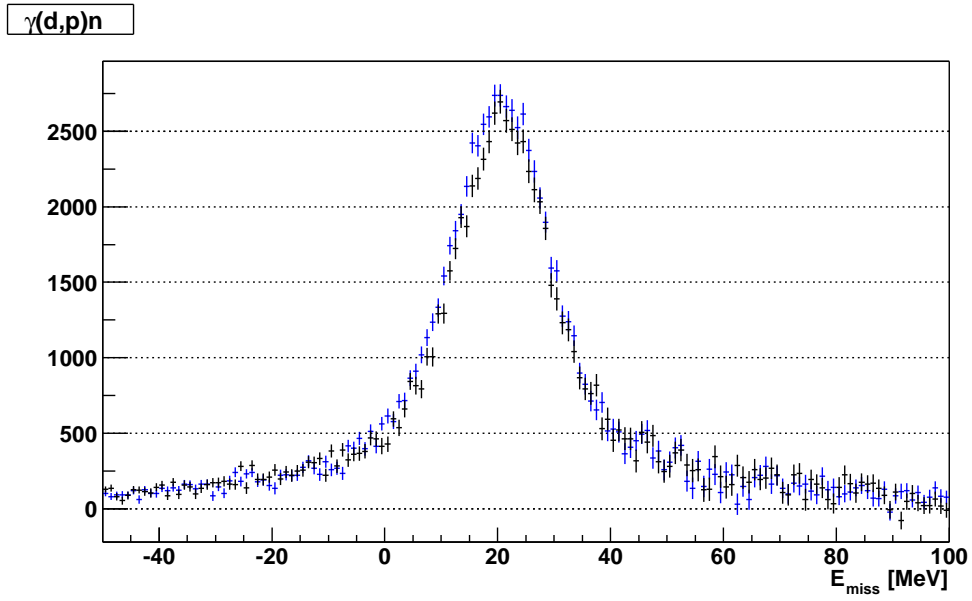


Figure 9.2: same as 9.1, empty target subtracted with beam flux normalization.

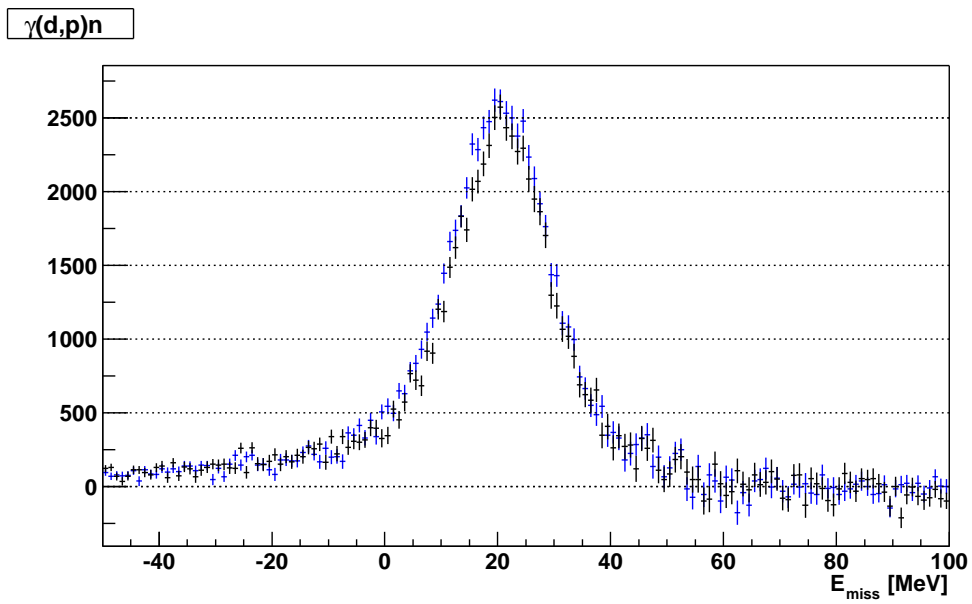


Figure 9.3: same as 9.1, empty target subtracted with a factor of 1.2.

Chapter 10

Detector Thresholds and Resolutions

10.1 Introduction

This section describes the energy thresholds and resolutions for energy, tof, and position measurements.

The detectors cannot detect arbitrarily low signals. They have a threshold below which a signal will not be detected. It is this kind of hardware threshold that will be discussed below. There is a threshold involved in creating a trigger signal in the electronics. However, in a good event (i.e. an event caused by a nuclear reaction in the target with at least one of the reaction particles hitting a detector) there is always at least one detector element that will have a signal far above trigger threshold. Once that detector element causes the trigger, the adc gates for all detector elements of the same subdetector will be open and even signals that would not be large enough to cause a trigger by themselves can be detected if they are above the individual detector element hardware threshold. Thus the detector element hardware threshold determines the energy detection threshold in the ADCs. In the data analysis it is important to impose a software threshold on each detector that is above the hardware threshold. The software thresholds are applied to the MC data as well as to the data taken from experiment. Thus the MC data that lacks intrinsic hardware thresholds becomes comparable to the data from experiment. The exact level of the software thresholds should not affect the final results. This is tested by setting software thresholds in the range of roughly one and a half to three times the hardware threshold and checking for changes in the final results. The situation is different for the tdc's. These receive their signals from the discriminated signals that are also used to feed the trigger. Thus a signal that is above the detector hardware threshold, but below the trigger threshold, can be recorded in the adc, but have a missing tdc. In the pn bars this will lead to missing tof and position information. In the lead glass the tof information would be missing. This can happen for good events. We can either set the software thresholds above the trigger threshold for each detector group to

ensure that tdc information is available for each hit or we can compensate for the missing information in the clustering of hits by assuming the hit to have the same tof and position as a hit in a neighboring detector element, if a neighboring element was hit, or otherwise assume that the signal was caused by noise and can be ignored.

The possible deviation of a measured energy, position, or tof in a detector from its actual value is described by resolutions. In order for the MC data to reproduce the resolutions observed in the data from experiment the MC data has to be *smear*ed. For each detector element the energy, tof, and position (where appropriate) information are added to a random number sampled from a Gaussian distribution centered at 0.0 with the standard deviation given by the resolution, e. g.

$$E_{smear} = E_{MCraw} + \delta E \quad , \quad \delta E = \sigma_E \times r_G \quad (10.1)$$

Here r_G is a number randomly sampled from a Gaussian distribution centered at 0.0 with unit standard deviation This smeared data is then processed through the same analysis procedure as the experiment data. The one resolution that cannot easily be applied to the MC data after it has been generated is the tagger energy resolution. The MC takes the tagger energy calibration and flux weighting of the tagger channels as an input. For each event generated by the MC software, a tagger bin is chosen randomly based on the flux distribution seen in the tagger data of the corresponding experiment data set. The initial photon energy is then randomly sampled from a distribution of energies spanned by this tagger channel.

In the following subsections it is shown how the hardware thresholds and resolutions for each detector subsystem were determined. The results are summarized in table 10.1.

10.2 Energy thresholds

The hardware thresholds are determined by simply looking at the energy (actually light) seen in each detector without placing any cuts on the data. For the pn bars, the xtal box corners, and the large xtal box veto paddles the threshold may be position dependent. Here the threshold is determined for all positions and the highest threshold is applied for all positions in the counter. In case of the box veto paddles the position is determined through the hit in the box crystal of the same particle, ensuring uniqueness in assigning the position by demanding that only one hit cluster in the box face exists. Figure 10.1 shows as representative examples one of the crystal box elements, the box veto paddle at negative x, and two of the pn bars.

For the xtal box the thresholds of all of the detector elements are within a close range, so that a common software threshold is used for all of the box elements (with the exception of broken channels where the threshold is set to infinity). For the pn bars the thresholds vary slightly from bar to bar and in order to maximize neutron efficiency the software thresholds are set individually close to the hardware thresholds. The bars that are split into two halves with

an air gap for the beam have higher thresholds than the bars with plastic scintillator over the full length of the bar, because in the *half bars* the light needs to pass two scintillator–air boundaries.

10.3 Position resolutions

In the Monte Carlo simulation SASY is described with all detector elements. For the xtal box faces and the lead glass the position resolution due to the discrete size of each detector element is thus taken into account. However, the resolution of the positions measured from adcs or tdcs needs to be matched to the data.

The position resolution in the xtal box corner counters is determined using signals from cosmic muons that cross through one side face of the xtal box and the adjacent box corners vertically. They are selected through the requirement that all nine xtals in one column of the box face have to be hit, but none of the other xtals in that face. The position resolution can be determined for ten different 6.35 cm wide regions in the corner to examine position dependence of the resolution. It is sufficient to use the same resolution for all places in the corners as shown by example in figure 10.2.

For the pn bars protons are used that pass through the finger counters. The protons are selected in an E-dE and reduced time of flight cut. The position of the hit in the pn bar is known from the straight trajectory through the finger counter. The front of the pn bar is used for the z coordinate of the hit, because protons will produce light immediately upon entering the scintillator. As in the case of the box corners the position resolution in the bars is position independent. Examples are given in figure 10.3. For very low signals in the bars (below ~ 10 MeV) the position resolution becomes worse than for larger energies. When good angular reconstruction is needed, the threshold can be increased above 10 MeV for the full bars and above 15 MeV for the half bars. The energy dependence of the position resolution is well described by

$$\sigma_x(E) = \tilde{\sigma}_x \left(\frac{E}{1\text{MeV}} \right)^{-0.4} \quad (10.2)$$

$\tilde{\sigma}_x$ is energy independent.

For the pn bars the cross talk problem of the November 1999 data made the position resolutions significantly worse compared to the April 2000 data. Even though the position determination with tdcs in the bars is much better than the determination in the box corners using adcs. The position resolution in the corners may be even worse for energy deposits below that of a cosmic ray muons. Fortunately the box corner position information does not need to be used much in the event reconstruction.

10.4 Timing resolutions

In the pn bars both time and x-position are calculated from the measured tdc values. This means that the timing resolution and the position resolution are related by the speed of light in the bars. However, the tagger tdc resolution enters into the tof determination, and thus the tof resolution cannot be calculated from the position resolution in the bars. The tof resolutions for the pn bars are determined using the width of the peak at $rtof = 1$ for relativistic electrons. The $rtof$ calculation depends on both tof and x-position in the bars. Thus the tof resolution has to be matched to the data after the x-position resolution is fixed. For the lead glass photons are used to make the $rtof = 1$ peak. An example is shown in figure 10.3.

10.5 Energy resolutions

The Monte Carlo simulation takes care of the part of the resolution due to the statistical nature of shower developments of photons and energy loss mechanisms of other particles. However, the part of the resolution due to noise in the detectors and similar effects needs to be taken into account through an additional resolution. This instrumental resolution is energy independent. Resolution due to bad calibrations or non-linear response of photo multipliers is proportional to energy. For the xtal box the additional resolution to the energy is found to be energy independent. For the pn bars a resolution proportional to the energy is found to describe the data best.

For the energy resolution determination it is desirable to select events that deposit a constant amount of energy in the detector element under investigation. Reactions from the bound nucleons include Fermi smearing. Pions from reactions of the free proton can be selected by placing a cut on $\phi_n - \phi_{pi^+}$ to select pions in the reaction plane when a neutron is detected in the pn bars. For a fixed incident photon energy and a given detector element (i.e. θ) they have constant energy. However, due to limited statistics it is not possible to determine the xtal box resolutions using these pions only.

Instead the energy resolution for both the xtal box and its vetos and the pn bars and pn bar vetos are determined by matching the E-dE scatterplot of the MC to the data. This is done for various slices in θ and for different Tagger channels ranging over all initial photon energies. The energy resolution is uniform within each detector system and independent of the energy deposit. As an example the matching energy calibrations and resolutions in data and MC are shown in figure 10.4 for $\theta \approx 90^\circ$. The two top panels are the E-dE plots for data and MC. The bottom panels are band projections of the top plots as indicated by the lines. Data is marked yellow and MC is pink.

Detector group	E_{thr} [MeV]	σ_E [MeV]	σ_{tof} [ns]	σ_{pos} [cm]
xt	3.0	1.0	-	-
xc	10.0	1.0	-	5.0
xv	0.6	0.4 to 0.6	-	-
pn	~ 5	$9.5\% \cdot E$	0.6	~ 5
pv	0.8	$9.5\% \cdot E$	0.6	~ 5

Table 10.1: Summary of detector thresholds and resolutions.

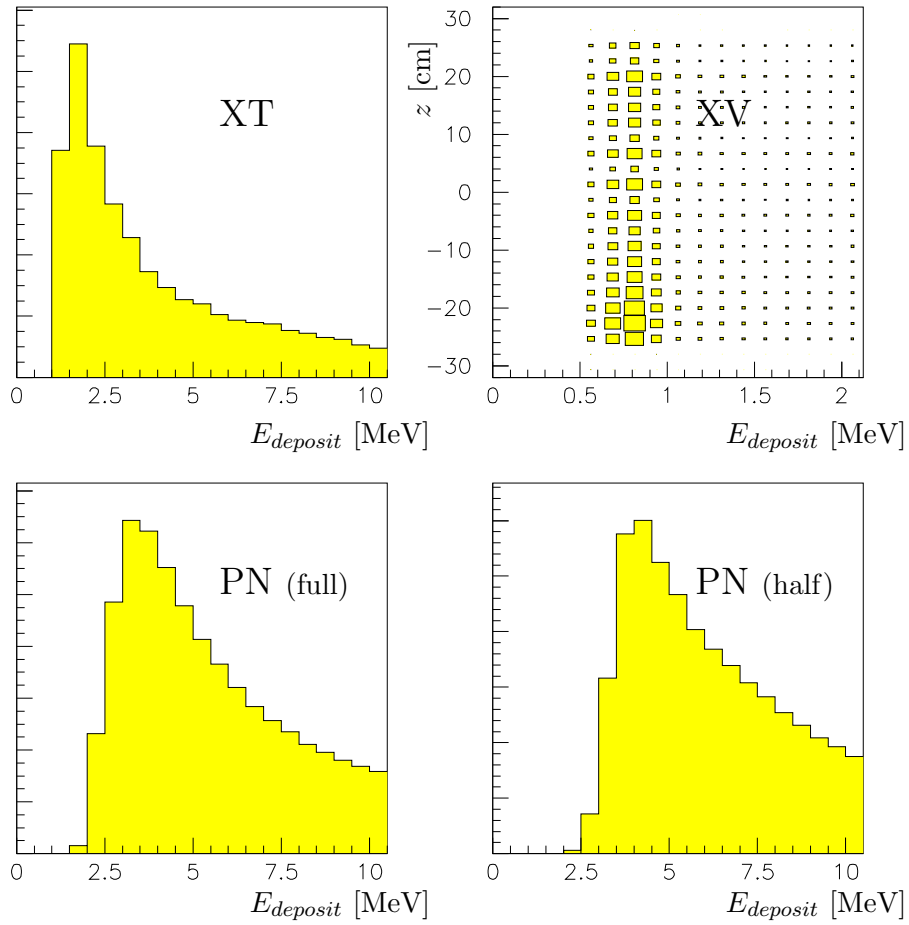


Figure 10.1: Energy spectra showing hardware thresholds for some detectors

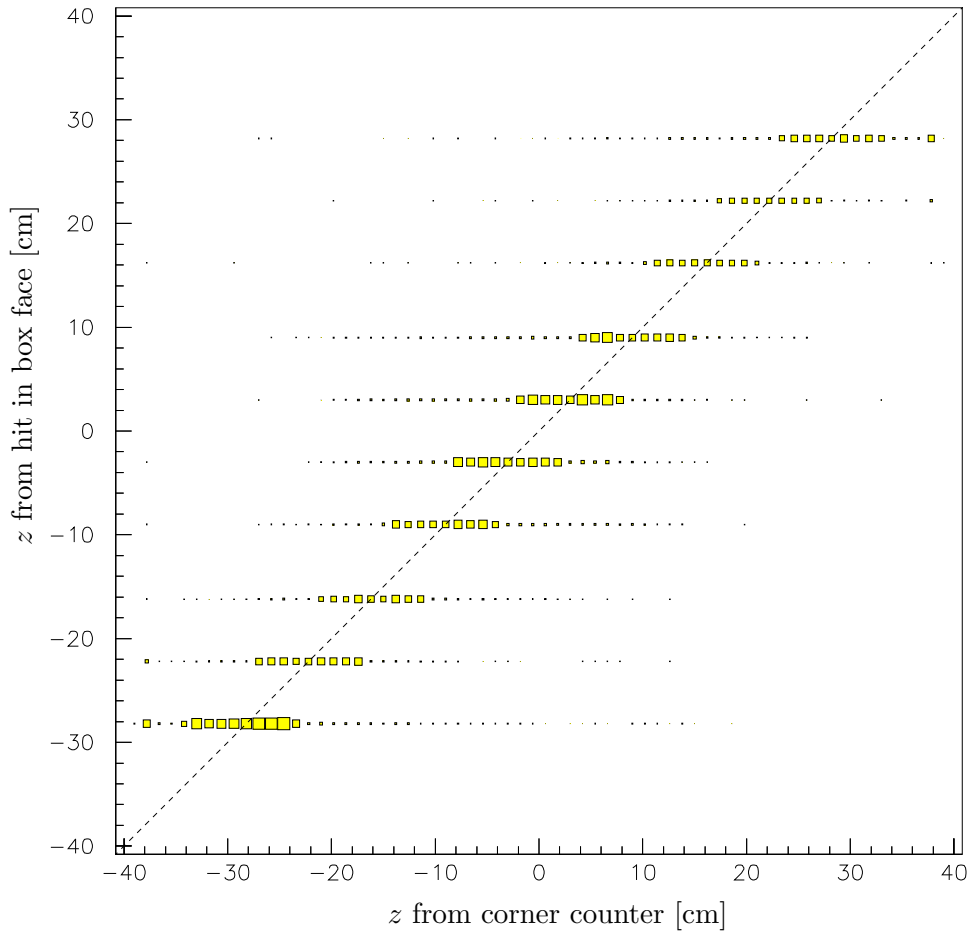


Figure 10.2: Position resolution in Xtal box corner 4, row 1, column 2

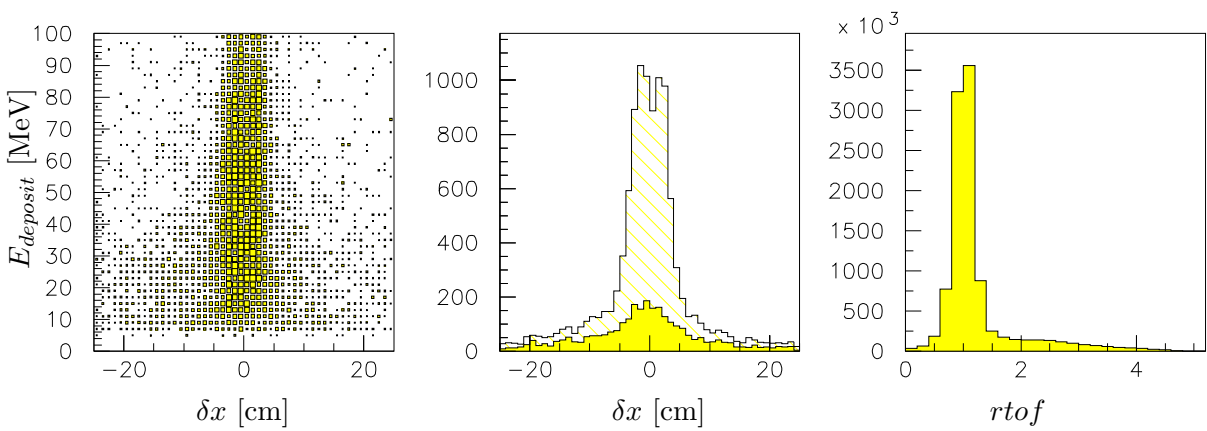


Figure 10.3: Position and tof resolution in PN bars (bar 14): $E_{deposit}$ vs. δx (left), δx for all energies (yellow hatched, center) and below 25 MeV (shaded, center), reduced tof spectrum (right)

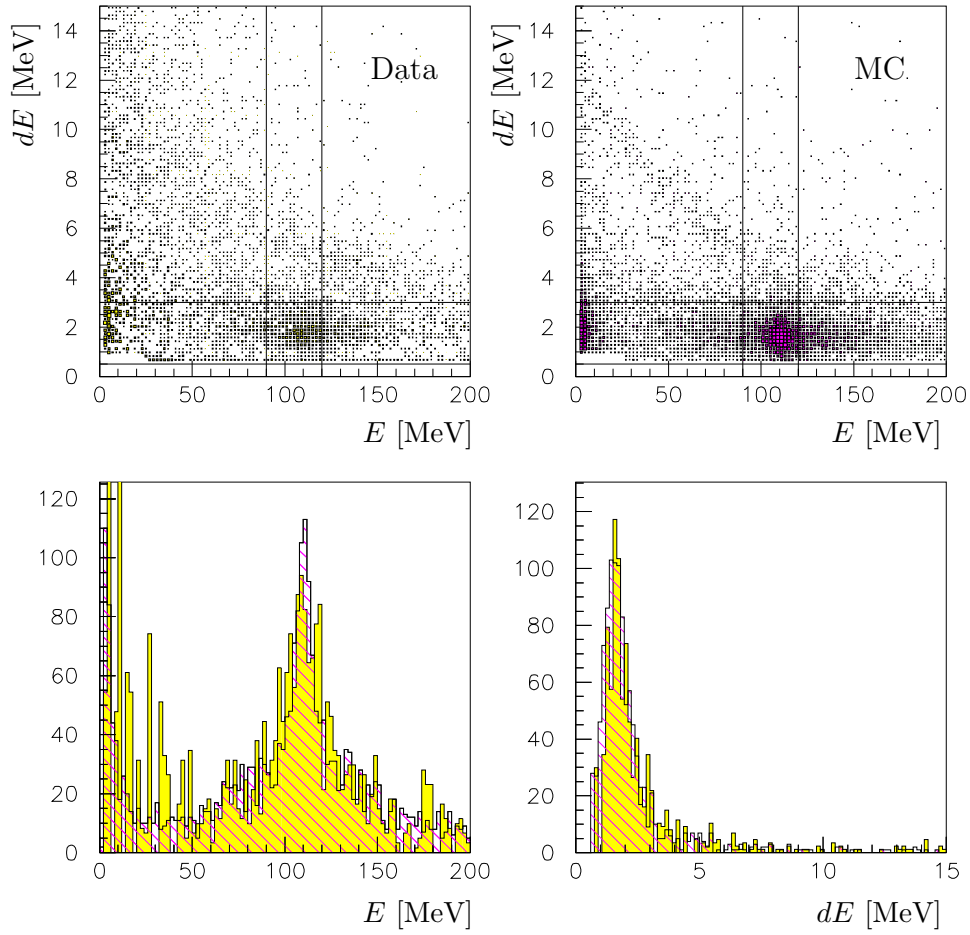


Figure 10.4: Energy resolution of the Xtal box: E-dE plots for data (top left) and MC (top right) with lines indicating the slices projected in E (bottom left) and dE (bottom right). In the bottom panels the yellow shaded plots are from data and the magenta hatched plots are from MC.

Chapter 11

Particle Identification

11.1 Introduction

In several places particle identification cuts have been mentioned without providing further detail. In this chapter the cuts are explained and the particle identification quality is examined.

11.2 Clustering of Hits

The first step in identifying particles in the calibrated detector data is to cluster hits in adjacent detector elements into hit clusters. The final states of reactions examined here have very few (two to three) final state particles. These have kinematical correlations. It is thus almost impossible that two particles hit the same region of the detector. This makes the clustering easy. In the xtal box clusters consist of hits in adjacent detector elements. If a cluster consists of more than one hit, the shape of the cluster is not examined further. The angles θ and ϕ of the particle are determined as the energy weighted average of the angles of the detector elements hit. The energy deposited by the particle is the sum of the energies deposited in all the hits of the cluster. For charged pions a cluster often consists of only one hit (plus a hit in the dE paddle). More than three hits in a charged pion cluster are very rare ($\approx 0.2\%$). Photons often shower into many crystals. However, the number of hits of a cluster is not used in the particle identification, because the E-dE identification is much more powerful.

The energy deposited in the dE paddle can be corrected for the thickness of material traversed and for light attenuation in the paddle once the position of the hit is known from the cluster. The first effect is due to the fact that the scintillator thickness seen by the pion is larger than the actual thickness of the scintillator paddle if the pion does not have normal incidence

on the paddle. This effect is removed from the data by normalizing to a unit path length chosen as the thickness of the paddle. The second effect is due to the paddle being read out on one end only. The correction of the dE energy deposition due to light attenuation can be up to 15%. It is mapped using cosmic muons that traverse the dE paddles perpendicular independent of position, thus leaving a constant amount of light where they hit the paddle.

In the pn bars clusters are formed assuming straight tracks from the target. Hits in each layer of the bars are grouped into the same cluster, if their position is on the same track in position and time of flight. Here broad cuts (larger than the resolution) are placed on the tof- and position difference between different hits of the same cluster. Neutrons will usually hit only one bar. Depending on their energy protons can hit all layers. The best tof information will come from the first layer that was hit because the proton slows down as it loses energy in the front layer of bars.

11.3 Charged Particle Identification

Different particles have different energy deposition profiles as they enter a material. For charged particles the energy loss per unit length $-\frac{dE}{dx}$ depends (among other things) on the mass of the particle. Particles of larger mass have a larger $-\frac{dE}{dx}$. Using a thin scintillator in front of the main counter, $-\frac{dE}{dx}|_E \times \delta x$ can be plotted versus the total Energy of the particle E. This is called the E-dE plot. It shows bands for different particles with electrons closest to the origin, pions a little further out and protons at highest dE. Neutral particles do not leave energy in the dE counters. E-dE plots for the pn bars and the xtal box are shown in figure 11.1. Due to the scale of the xtal box histogram protons are barely noticeable in the plot. In the pn bars pions cannot reliably be distinguished from electrons. This limits the angular coverage for charged pions compared to neutral pions. For these the two photons can be detected in the xtal box or in the xtal box and lead glass, resulting in complete coverage of the forward region.

In the pn bars protons are cleanly separated from other particles. In the xtal box protons, pions, and electrons are separated. There are tails from the electrons under the pions for very low energy pions. Pions and protons overlap slightly at some energies. Further cuts can be placed on initial photon energy or θ of the particle. This results in a slight improvement of the separation between different particles. However, it has little impact on final results.

For charged particles the energy detected in the xtal box is smaller than the initial energy of the particle because some energy is lost in material of the target, in-beam-cryostat, aerogel veto detector, and xtal box support structure. This energy loss can be modeled using the MC simulation and energy spectra can be constructed using either the energy deposited in the counter or reconstructed vertex energy.

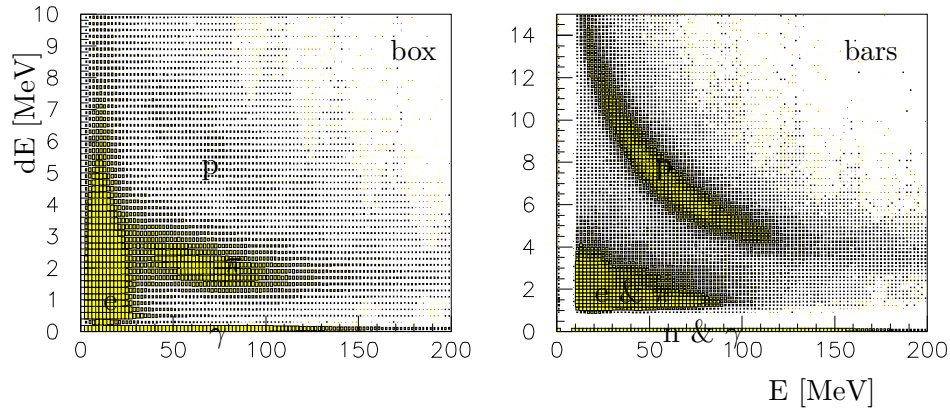


Figure 11.1: E-dE plots for xtal box and pn bars, no cuts.

11.4 Nucleon Identification

In the pn bars nucleons are cleanly separated from electrons and pions in time of flight. To place a cut the reduced time of flight (rtof or inverse beta) is constructed as $rtof = c / \frac{l}{tof}$ where l is the distance travel by the particle from target to detector and c is the speed of light. Slower particles have a larger $rtof$. Figure 11.2 shows the rtof spectrum in the pn bars without cuts and after identification of a charged pion in the xtal box. The coincidence with a pion eliminates almost all the photons and electrons, leaving only the slow nucleons. For protons the front of the counter is used in determining l . For neutrons the center of the counter is used because they can start to produce light anywhere inside the counter. Protons and neutrons are distinguished by the energy in the dE paddle. Neutrons do not leave energy there. Protons will form the typical band in the E-dE plot. In figure 11.3 it is seen that the E-dE plot contains very few electrons and pions after a nucleon selection cut on the rtof. These remaining particles can be cut in the E-dE plot, cutting events with $dE < 5 \text{ MeV} - E/20$.

The vertex energy of neutrons can be calculated from their tof, because they do not lose energy on the way to the counter. For protons the energy calculated from tof will be lower than the vertex energy because the proton can lose energy on the way to the counter, slowing it down.

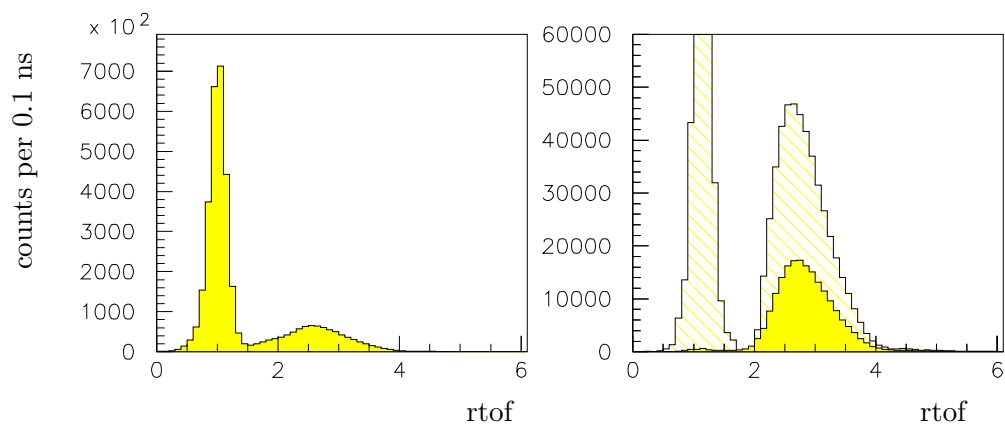


Figure 11.2: *rtof* in the pn bars: without empty target subtraction (left) and with (yellow shaded) and without (hatched) the additional requirement of a charged pion in the xtal box in coincidence.

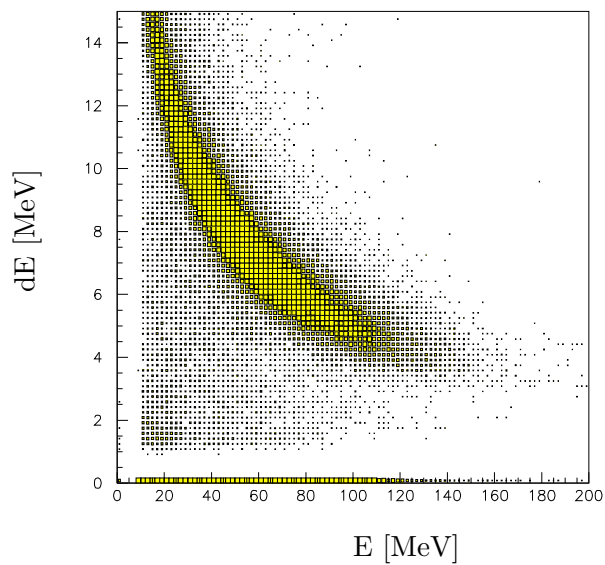


Figure 11.3: E-dE plot for the pn bars for particles with *rtof* > 1.5.

Chapter 12

Energy Spectra of Pions

In this section the energy deposit of pions in the xtal box is examined in detail. Comparison of spectra from experiment and MC shows how well the MC simulation describes the detector. Then missing energy spectra are examined to learn about the effects of the Fermi smearing inside the deuteron.

12.1 Energy Deposit of Positive Pions

The energy spectra of positive pions of data and the MC simulation are in good agreement for all angles θ and incident photon beam energies. The GEANT 3.21 energy loss package describes the energy loss of positive pions in NaI well. Further the spectra demonstrate that the few electrons that pass the E-dE pion selection cut are subtracted by the empty target. With a much less restrictive cut the electrons can be seen as an excess of counts at low energy deposit. Examples of the spectra are shown in figure 12.1. Spectra at angles and energies not shown have equally good agreement between data and MC.

12.2 Energy Deposit of Negative Pions

With the unmodified GEANT 3.21 energy loss package the energy deposit of negative pions in NaI (i.e. in the xtal box) was not described well. The energy loss routine was modified such that particles produced when the π^- stars (i.e. gets captured in a nucleus resulting in small breakup products of the nucleus being emitted in all directions) are not traced further with a certain probability. By default in the GEANT software all breakup products are put on the stack and GEANT processes them one by one, producing light from each one of them. In the modified code only resulting particles (protons, neutrons, deuterons, He^3 , ...) above an energy threshold are put on the stack with only a certain probability. The

energy threshold and probability are specified for each particle species. This in effect is a modification of the branching ratios and cross sections of the pion capture process. The parameters are adjusted to fit the data. With this modification the Monte Carlo matches the data reasonably well, as seen in figure 12.2.

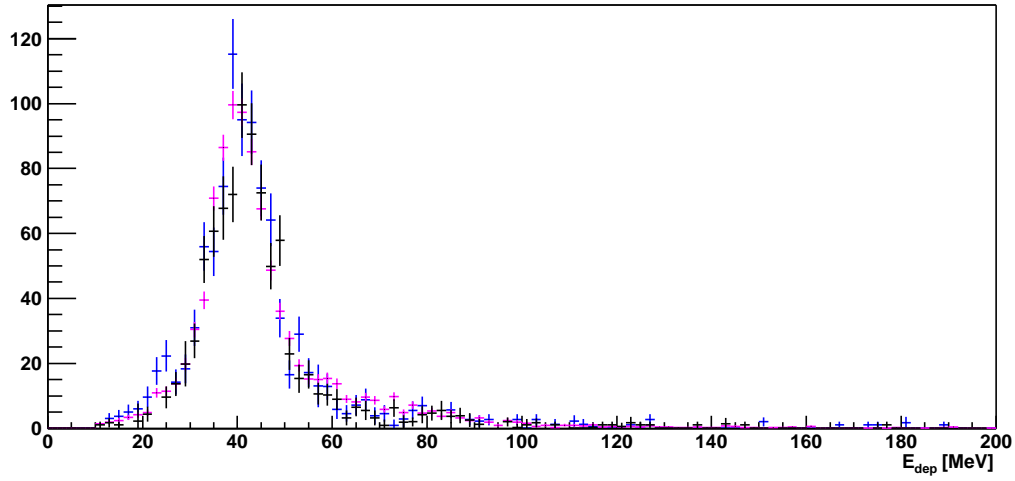
12.3 Missing Energy spectra

The inclusive missing energy spectrum for the pions (figure 12.3) clearly shows a narrow peak centered at zero on top of a broader distribution. The narrow peak is due to pions from reactions on the free proton in the hydrogen atom of the HD molecules in the target and its resolution is due only to the finite energy and angular resolution of the detector. The broader contribution is due to reactions on one of the bound nucleons in the deuterium nucleus. The Fermi smearing, i.e. the distribution of relative momenta of the two nucleons inside the deuterium, causes the width of that part of the distribution. This interpretation of the spectrum is supported by the exclusive missing energy spectra (figures 12.4 and 12.5). The spectrum from positively charged pions looks similar to the inclusive spectrum. The difference is that the broad contribution is suppressed, as expected. Instead of one free and two bound nucleons as for the inclusive spectrum, only one free and one bound proton contribute to the spectrum, reducing the broad contribution to (approximately) half its size. Negatively charged pions can result from reactions on the neutron only. Since all neutrons in the target are bound, the narrow peak disappears in the spectrum for negative pions and only the broad distribution is left.

Even though the binding effects in the deuterium nucleus are smaller than in any heavier nucleon, the neutron inside the deuterium cannot be viewed as a good approximation to the free neutron. To extract free neutron data from the deuterium data, a good model of the deuteron has to be used. This is at present a challenge for theorists.

In the π^+ missing energy spectrum a cuts can be placed to select events that are mostly from the free or mostly from the bound proton. However, complete separation cannot be obtained on an event by event basis. To extract cross sections for the reactions on the deuteron alone, the known contribution from the free proton can be subtracted. For the beam asymmetry a clean separation is not possible and pure hydrogen and deuterium targets can give better results.

$E_\gamma = 244 \text{ MeV}, \theta_{\text{lab}} = (120 \pm 5)^\circ$



$E_\gamma = 341 \text{ MeV}, \theta_{\text{lab}} = (100 \pm 5)^\circ$

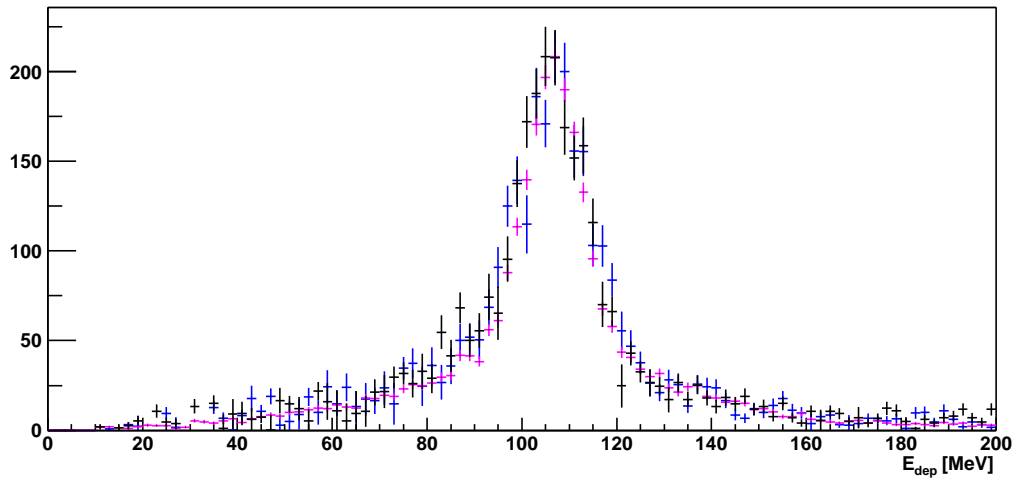


Figure 12.1: Energy deposit in the xtal box for π^+ at two beam energies and angles. Black and blue are data in each polarization state, magenta is MC.

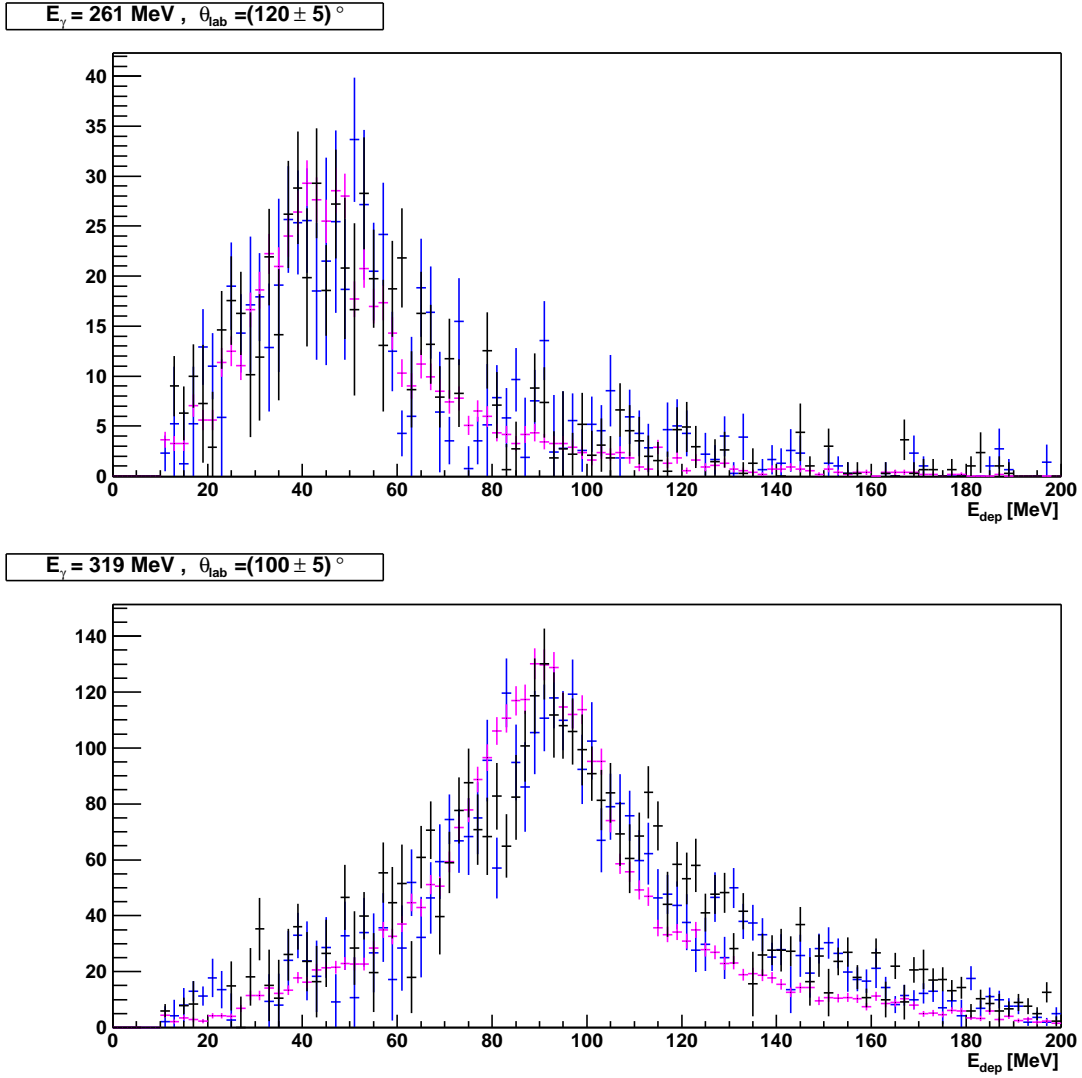


Figure 12.2: Energy deposit in the xtal box for π^- at two beam energies and angles. Black and blue are data in each polarization state, magenta is MC.

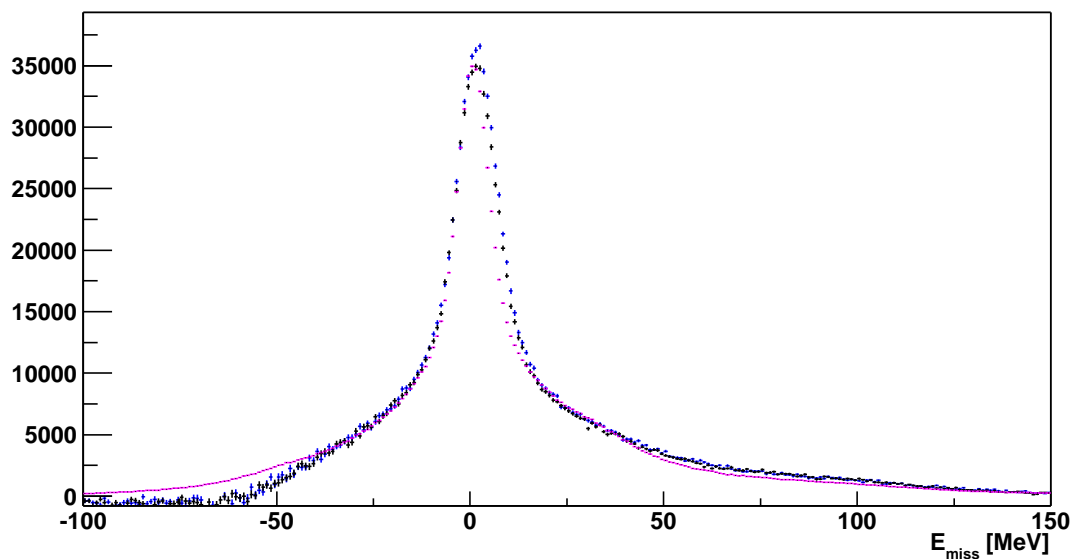


Figure 12.3: Missing energy in the xtal box for π^\pm . Black and blue are data in each polarization state; magenta is MC, scaled to match the peak height of the data.

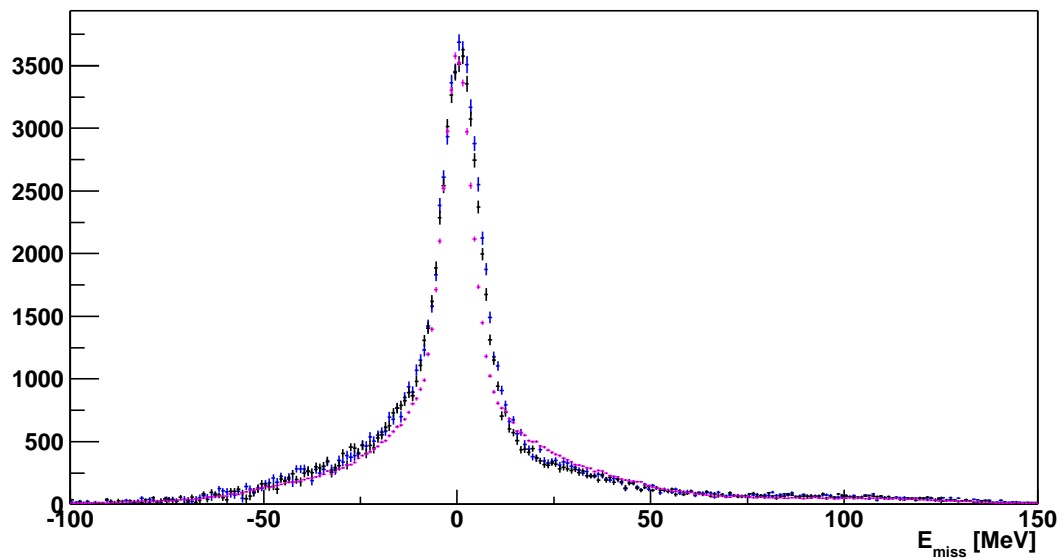


Figure 12.4: Missing energy in the xtal box for π^+ . Black and blue are data in each polarization state; magenta is MC, scaled to match the peak height of the data.

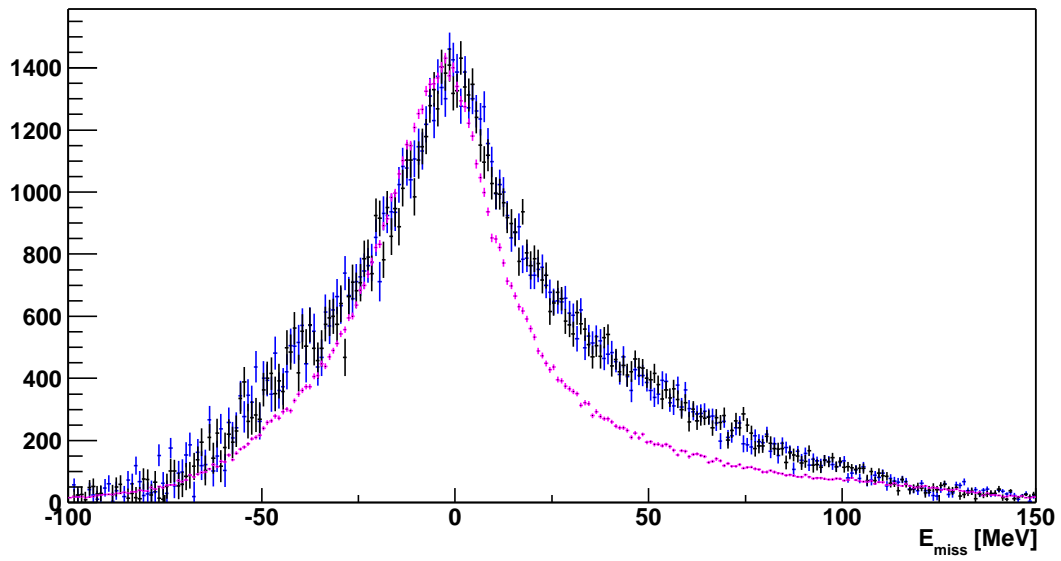


Figure 12.5: Missing energy in the xtal box for π^- . Black and blue are data in each polarization state; magenta is MC, scaled to match the peak height of the data.

Chapter 13

Detector Efficiency

The Monte Carlo simulation is used to determine the detection efficiency of particles in the detector. In the simulation all pion production channels on the free proton, bound proton, and bound neutron of the HD target are simulated, as well as the deuteron breakup. The neutral pion production channels should not lead to any yield in any variable of interest. They are included because a reaction may be misidentified during the analysis.

The Monte Carlo contains the initial four-momenta of the particles produced in the reactions. This is the MC-privileged information. Also the detector response to the reaction is recorded for each simulated event. This is the detector information. It is analyzed using the same software as is used for the data from the experiment to reconstruct the reaction. Thus the simulation produces two distributions for each variable, the detected distribution and the privileged initial distribution. The ratio of these distributions, the fraction of events seen in the detector divided by the number of events created in the target, is used as the efficiency in the cross section calculations. It takes into account that the detectors may not produce a signal that passes all analysis cuts, even if a particle hits the detector, as well as the solid angle acceptance, i.e. that a particle may be emitted into a direction where it does not hit any detector at all. The correct simulation of the acceptance only relies on providing the correct detector geometry to the Monte Carlo simulation. But the detector response in the simulation has to be verified carefully by comparison with the data. The efficiency obtained from the MC can only be trusted when the spectra for energy deposit and angular distributions match the data. The spectra of pion energy deposit in the detectors have been compared in chapter 12.

The neutron detection efficiency is $\sim 25\%$ in the pn bars and cannot be determined from the data directly. Using a H₂-target the neutron efficiency could be measured. A charged pion in the xtal box would identify the reaction channel as $\gamma p \rightarrow \pi^+ n$. Two-body kinematics would determine the direction of the neutron. The neutron detection efficiency could be mapped as a function of neutron energy and position in the pn bars. This measurement has not been performed yet.

The neutron detection efficiency of the GEANT simulation has been compared to another software, the Stanton code [26]. This code contains neutron efficiencies based on measurements on CH materials. The efficiencies predicted by the two different codes are in good agreement.

Two different sets of cuts have been applied to obtain results. In the first analysis charged pions have been selected in the xtal box using an EdE cut with or without a pion missing energy cut in coincidence. Then the bars have been used to detect a nucleon in coincidence without placing any cut on the angle of the nucleon. This analysis relies on a good energy reconstruction in the xtal box. The second analysis uses nucleons detected in the pn bars, identified through their time of flight and a very open EdE cut for the protons. From the nucleon the angle of the pion is reconstructed using two body kinematics. If a charged hit happened in the xtal box within a cone of 15° around the pion angle, it was assumed to be a pion. This can be verified in the EdE plot of such hits, where near 100% of the hits pass the pion cut. This analysis relies on a good reconstruction of the angles, but does not make use of the EdE cut in the box at all.

Chapter 14

Calculation of Cross Section and Beam Asymmetry from the Data

In previous chapters it was described in detail how to determine the yields of final state particles and the gamma ray flux. This chapter shows how to extract cross sections and beam asymmetries from this data.

The differential cross section is given by

$$\frac{d\sigma}{d\Omega} = \frac{N_{int}}{N_\gamma \cdot N_{scat} \cdot d\Omega}, \quad (14.1)$$

with N_{int} being the number of interactions caused by N_γ incident beam photons on N_{scat} scattering centers in the target scattered into a solid angle $d\Omega$.

In the experiment N_{int} is the measured yield Y of particles in the detector divided by the efficiency ϵ . ϵ takes into account the detection response and acceptance for each segment of solid angle.

$$N_{int} = \frac{Y}{\epsilon} \quad (14.2)$$

The measured cross sections at a given θ are averaged differential cross sections over a solid angle covering full azimuth and ten degree bins in θ :

$$d\Omega(\theta) = 2\pi \cdot (\cos(\theta - 5^\circ) - \cos(\theta + 5^\circ)) \quad (14.3)$$

The photon flux N_γ for each polarization state and beam energy bin is determined from the beam flux monitor data as described in section 7.4. Substituting 14.2 into formula 14.1, the cross section depends on the fraction of yield to flux. It is determined in the experiment using accidental tagger hit and empty target subtraction (see chapters 8 and 9):

$$\frac{Y}{N_\gamma} = \frac{Y_{true}^{full} - Y_{acc}^{full}}{N_\gamma^{full}} - \frac{Y_{true}^{empty} - Y_{acc}^{empty}}{N_\gamma^{empty}} \quad (14.4)$$

The number of scatterers in the target is calculated from the target length L_{targ} , Avogadro constant N_A , and molar volume of HD V_{mol} as

$$N_{scat} = \frac{N_A}{V_{mol}} \cdot L_{targ} = 9.37 \times 10^{22} (cm^{-2}) \quad (14.5)$$

with $N_A = 6.022142 \times 10^{23} \text{ mol}^{-1}$, $V_{mol} = 20.57 \text{ mol/cm}^3$ (the number for $T = 0 \text{ K}$ is used as a very good approximation to the molar volume at 1.3 K), and $L_{targ} = 3.2 \text{ cm}$ as determined in section 7.5.

The cross sections measured in the experiment are obtained with partially (although highly) polarized beams. Now formulas are derived to extract unpolarized cross section and beam asymmetry from the cross sections σ_0 and σ_{90} measured with beam polarizations P_0 and P_{90} .

In the absence of target polarization the observed cross section depends on the direction (θ, ϕ) and linear polarization P of the beam, with the electric field vector of the photons in the $\phi = 0$ plane (i.e. ϕ is the angle between polarization and reaction plane) [27]:

$$\frac{d\sigma_{obs}(\theta, \phi)}{d\Omega} = \frac{d\sigma_{unpol}(\theta)}{d\Omega} (1 + P\Sigma(\theta) \cos(2\phi)) \quad (14.6)$$

The physics is contained in the unpolarized cross section $\sigma_{unpol}(\theta)$ and the beam asymmetry $\Sigma(\theta)$. These we want to extract from the data.

The two measured cross sections can now be expressed as:

$$\frac{d\sigma_0(\theta, \phi)}{d\Omega} = \frac{d\sigma_{unpol}(\theta)}{d\Omega} [1 + P_0^\gamma \Sigma(\theta) \cos(2\phi)] \quad (14.7)$$

$$\begin{aligned} \frac{d\sigma_{90}(\theta, \phi)}{d\Omega} &= \frac{d\sigma_{unpol}(\theta)}{d\Omega} \left[1 + P_{90}^\gamma \Sigma(\theta) \cos\left(2\left(\phi + \frac{\pi}{2}\right)\right) \right] \\ &= \frac{d\sigma_{unpol}(\theta)}{d\Omega} [1 - P_{90}^\gamma \Sigma(\theta) \cos(2\phi)] \end{aligned} \quad (14.8)$$

where $\phi = 0$ is along the x-axis.

These two equations can be solved for the unpolarized cross section and beam asymmetry. Since these two quantities do not depend on ϕ , we can integrate over ϕ to decrease statistical uncertainties of the measurement:

$$\frac{d\sigma_{unpol}(\theta)}{2\pi d\theta} = \int_0^{2\pi} \frac{P_{90}^\gamma \frac{d\sigma_0(\theta, \phi)}{d\Omega} + P_0^\gamma \frac{d\sigma_{90}(\theta, \phi)}{d\Omega}}{P_0^\gamma + P_{90}^\gamma} d\phi \quad (14.9)$$

and

$$\Sigma(\theta) = \int_0^{2\pi} \frac{\frac{d\sigma_0(\theta, \phi)}{d\Omega} - \frac{d\sigma_{90}(\theta, \phi)}{d\Omega}}{\left(P_{90}^\gamma \frac{d\sigma_0(\theta, \phi)}{d\Omega} + P_0^\gamma \frac{d\sigma_{90}(\theta, \phi)}{d\Omega} \right) \cos(2\phi)} d\phi \quad (14.10)$$

The $\cos(2\phi)$ dependence of the polarized cross section can be observed in the yields in each polarization state. Figure 14.1 shows the difference in the charged pion yields of the two

polarization states divided by their sum for one energy bin of the tagger. The solid line is a fit of $p_1 \cos[2(\phi + p_2)] + p_3$ with fit parameters p_1 to p_3 . The offset p_3 is 1.57% of the amplitude p_1 and the phase p_2 is -1.49° . These two values are close to zero. The experimental asymmetry has the expected ϕ dependence. The amplitude p_1 is the (θ -averaged) beam asymmetry for this tagger energy bin.

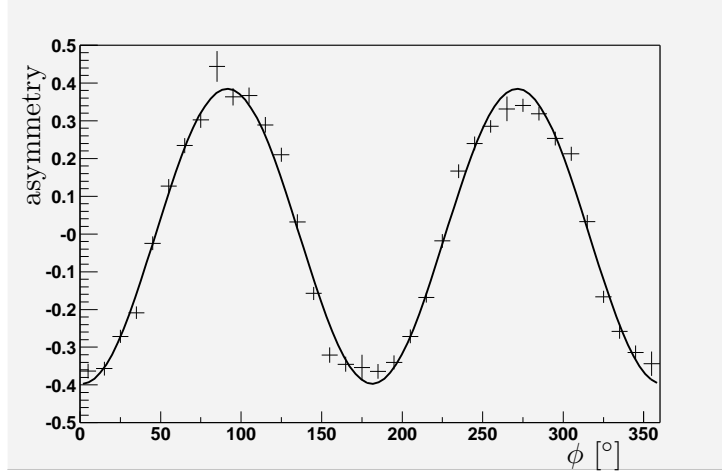


Figure 14.1: ϕ dependence of the asymmetry $\frac{Y_0 - Y_{90}}{Y_0 + Y_{90}}$.

Chapter 15

Cross Sections

The cross sections $d(\gamma, \pi^- p)p$, and $d(\gamma, \pi^+ n)n$ are shown in figures 15.1 and 15.2 versus center-of-momentum pion angle and in figures 15.3 and 15.4 for the lab system, and tabulated in the appendix. The π^+ cross sections for deuterium have been calculated from the data measured on HD by subtraction of the well known cross section for $p(\gamma, \pi^+ n)$, using the current solution of the SAID database [28].

In the plots results from both different analyses are shown (cf. chapter 13). The black points are from the analysis that uses the E-dE cut in the xtal box (first analysis). The green points show the results obtained by detecting a nucleon in the pn bars and using a cut on the conjugate angle of the pion (second analysis). Within statistical errors the two analyses agree with the exception of a few angles. The first analysis is considered more reliable in the π^+ reaction channel, because it does not use the position information in the pn-bars for angle reconstruction. The pn-bar position information was distorted by cross talk. The results quoted in the appendix for the π^+ channel are from the first analysis. For the π^- channel the results from the second analysis are given in the tables. The π^- energy distribution in the xtal box could not be reproduced well by the Monte Carlo simulation. This is a worse problem than the position distortions in the pn bars.

For comparison the 1973 DESY data in the π^- channel [29] is plotted in figure 15.3 . The data is given in table 2 of [29] for the lab angles at which it is plotted here. The data shown here has been interpolated from the beam energies given in [29].

The plots show the predictions for the free nucleons from the SAID multipoles in black and the calculation from the impulse approximation of the model of the deuteron developed by T.-S. H. Lee and the LEGS collaboration in red. It can be seen that the Fermi motion in the deuteron causes the cross sections to decrease compared to the free nucleon predictions from SAID. The missing contributions in the model (final state interaction, etc.) are expected to increase the model predictions. This will result in better agreement with the data in both charged pion channels.

15.1 Errors

Statistical errors are given in the data tables in the appendix. The systematic errors are shown here. In the cross section measurements the target length determination introduces the largest uncertainty. Other errors are due to photon flux normalization and photon polarization. The empty target contribution was determined based on the spectra from deuteron breakup. Different correction factors have been used to produce the cross sections and the error has been estimated based on the change seen in the cross sections. Detector efficiency uncertainty has been measured using the coincidence of cuts on angle and E-dE. Running each analysis with a different detector calibrations, resolution, and thresholds gave results varying by 2%. These errors are listed in table 15.1 and add in quadrature to the total systematic uncertainty of $\pm 7.1\%$.

Source of error	Error [%]
target length	5.9
photon flux	1
beam polarization	1
empty target	1
detector efficiency	3
calibrations and resolutions	2
total	7.1

Table 15.1: Systematic errors for the cross sections.

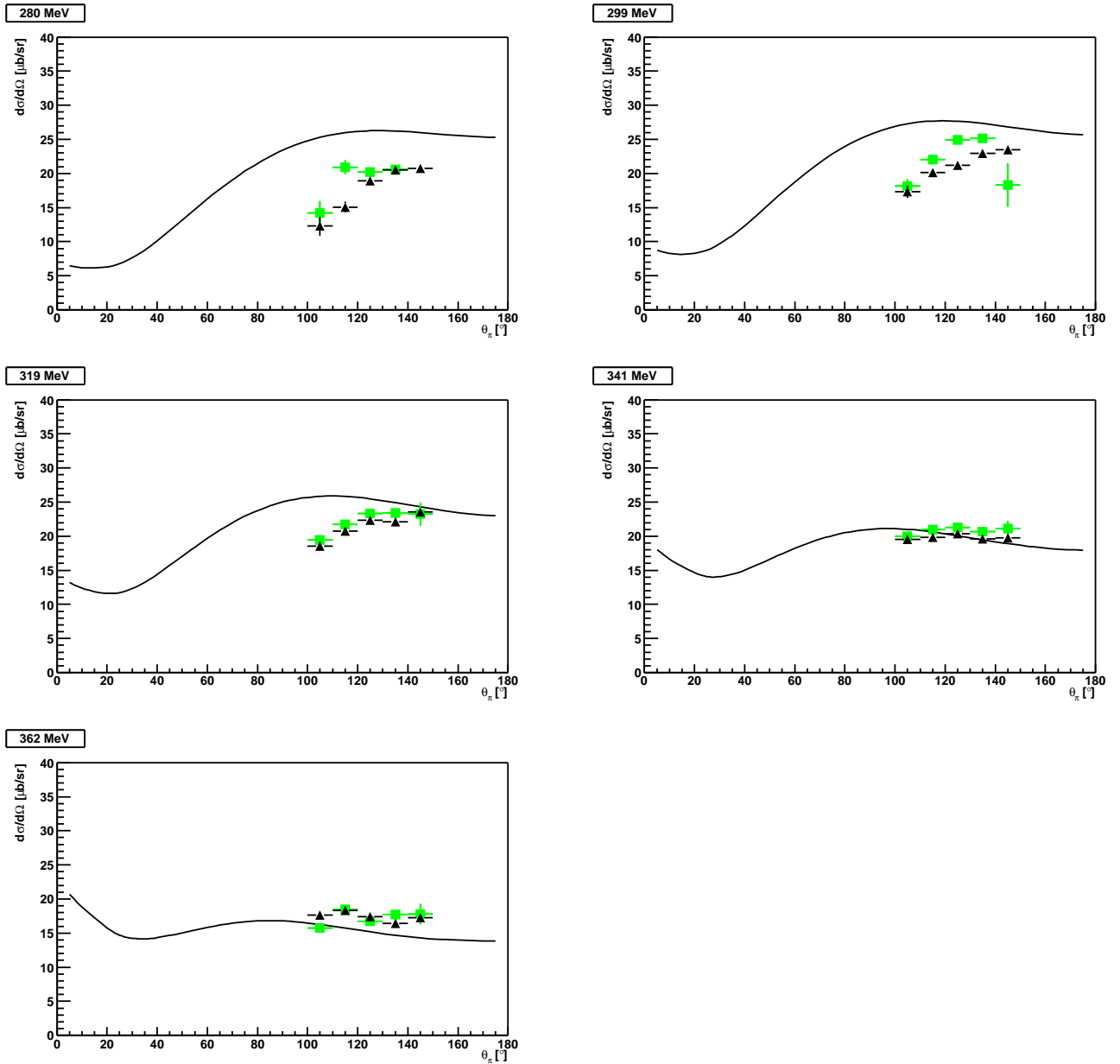


Figure 15.1: Differential cross section for $d(\gamma, \pi^- p)$, exclusive π^- production on d vs. θ_{CM} . Solid line is the SAID prediction for $n_{free}(\gamma, \pi^- p)$. Black results are from the first analysis (E-dE cut in xtal box); green results are from the second analysis (nucleon in bars and cut on conjugate pion angle).

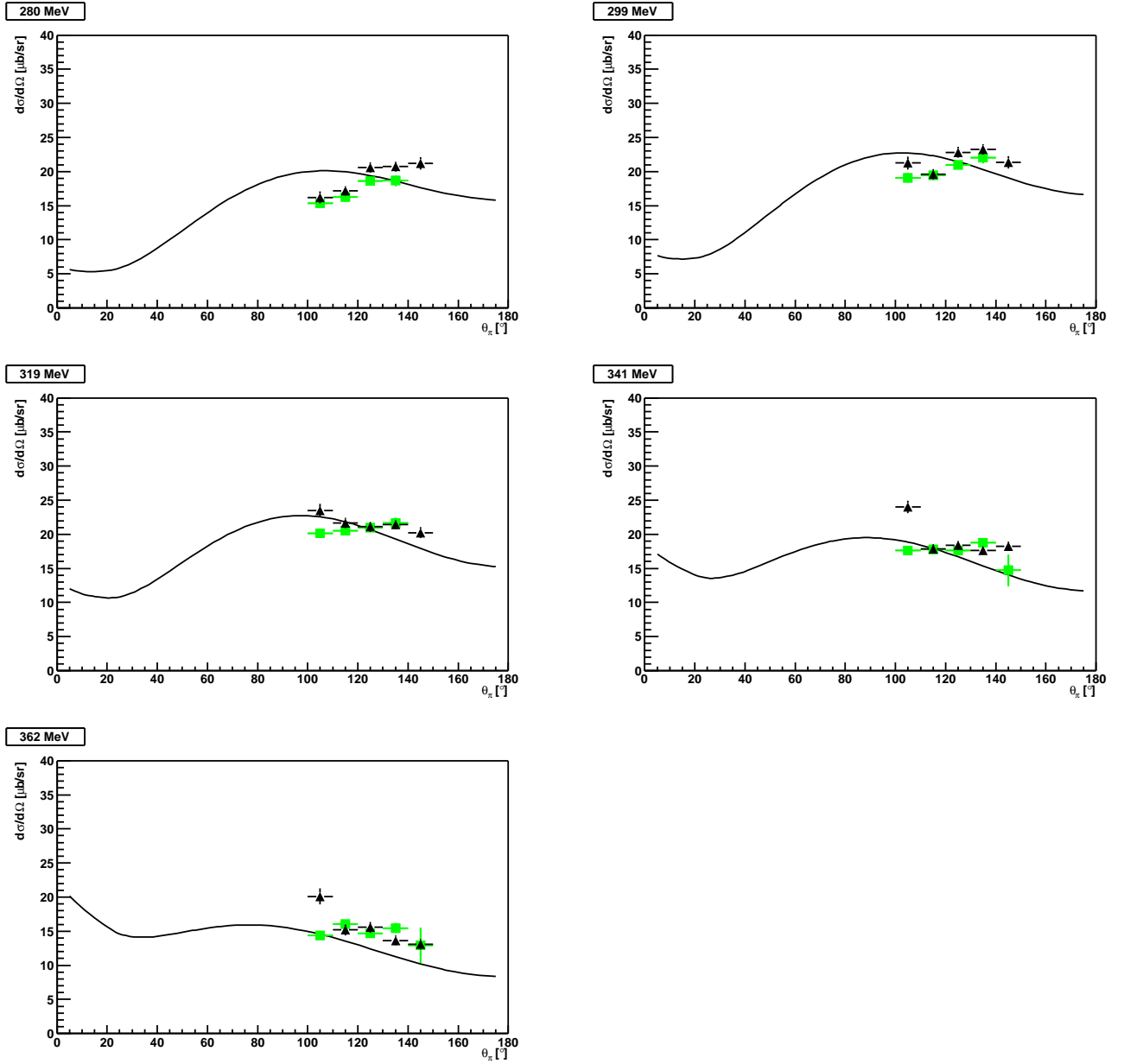


Figure 15.2: Differential cross section for $d(\gamma, \pi^+n)$, exclusive π^+ production on d vs. θ_{CM} constructed from $HD(\gamma, \pi^+n)$ by subtracting the free $p(\gamma, \pi^+n)$ cross section. Solid line is the SAID prediction for $p_{free}(\gamma, \pi^+n)$. Black and green symbols as in figure 15.1.

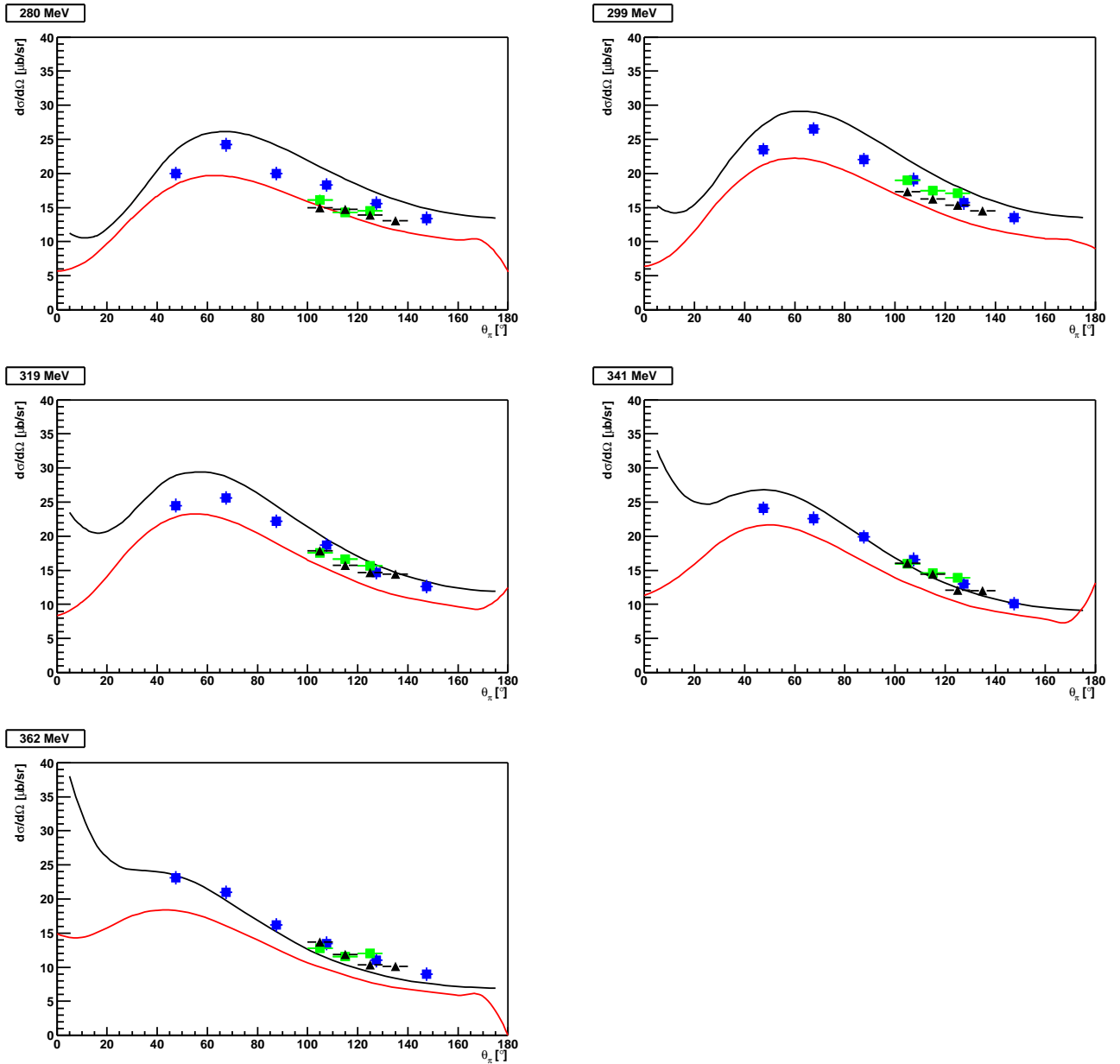


Figure 15.3: Differential cross section for $d(\gamma, \pi^- p)$, exclusive π^- production on d vs. θ_{lab} with comparison to prediction from impulse calculation (red) and to SAID prediction for $n(\gamma, \pi^- p)$ (black). Black and green symbols as in figure 15.1. Blue points are taken from [29] for comparison.

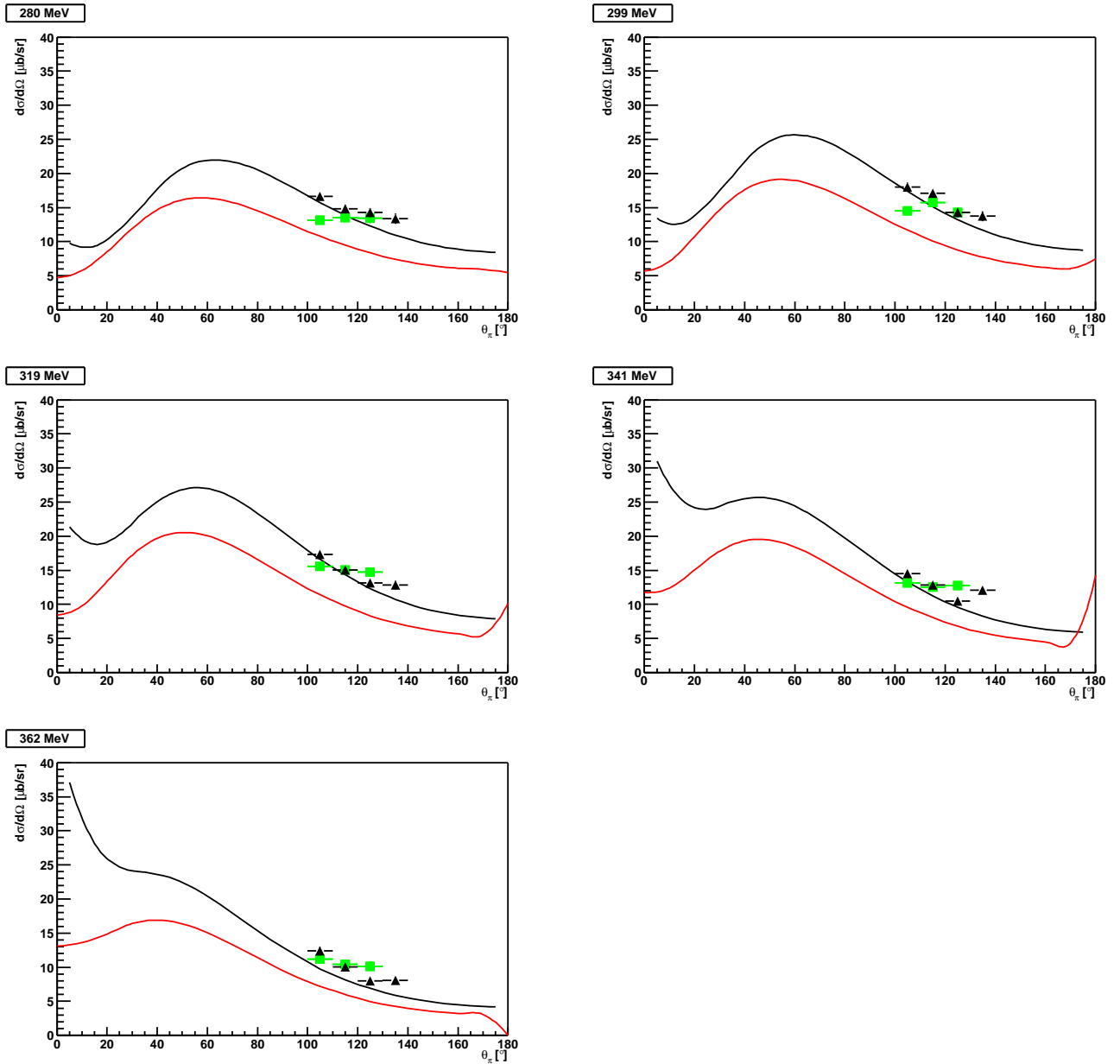


Figure 15.4: Differential cross section for $d(\gamma, \pi^+n)$, exclusive π^+ production on d vs. θ_{lab} (constructed from $HD(\gamma, \pi^+n)$ by subtracting the free $p(\gamma, \pi^+n)$ cross section) with comparison to prediction from impulse calculation (red) and to SAID prediction for $p(\gamma, \pi^+n)$ (black). Black and green symbols as in figure 15.1.

Chapter 16

Beam Asymmetries

The beam asymmetries for the exclusive charged pion reaction channels on HD are shown in figures 16.1 and 16.3 for the CM frame and in figures 16.4 and 16.6 for the lab frame. They are tabulated in the appendix. The two different analyses did give identical asymmetries. The results shown here are from the analysis that uses the E-dE cut in the xtal box and not the angle of the nucleon in the pn bars.

The asymmetries for the π^+n channel on HD have contributions from reactions on the free as well as the bound proton and are consistent with the SAID predictions. The beam asymmetry for this channel on d are calculated from the data measured on HD and the SAID predictions for the free proton as

$$\Sigma_{d(\gamma,\pi^+n)} = \frac{(\sigma_{HD}^{\parallel} - \sigma_p^{\parallel}) - (\sigma_{HD}^{\perp} - \sigma_p^{\perp})}{(\sigma_{HD}^{\parallel} - \sigma_p^{\parallel}) + (\sigma_{HD}^{\perp} - \sigma_p^{\perp})} \quad (16.1)$$

where

$$\sigma^{\parallel} = \sigma^{unpol}(1 + \Sigma) \quad (16.2)$$

$$\sigma^{\perp} = \sigma^{unpol}(1 - \Sigma) \quad (16.3)$$

for both HD and p and for each angle θ . This is shown in figures 16.2 and 16.5. The asymmetries calculated for the π^+n reaction on d are similar to the asymmetries on HD, because the asymmetry on the proton is close to the measured data over the range of angles investigated here.

The asymmetries for the π^-p reactions on the bound neutron do not show large deviations from the SAID predictions in the angular range tested with the present experiment. However, at forward angles the π^- asymmetry is slightly smaller than what is predicted by the multipoles for the free nucleon. There is little data available for beam asymmetries in this

reaction channel. Only 35 data points exist in the photon energy range from 270 MeV to 370 MeV. Data from the present measurement has significantly lower statistical errors than most previous measurements. The only other data with small statistical error is limited to $\theta_{CM} = 97^\circ$. For comparison the data at 300 MeV from the 1973 Tokyo measurement [30] are shown in figure 16.1.

For both reaction channels the beam asymmetry calculated from the impulse approximation of the Lee deuteron model are shown in red in the plots in the lab frame. The Fermi motion reduces the asymmetry predicted by the model. The impulse approximation results are not in good agreement with the data. The missing parts in the model are important. Work in this area will continue with the data presented here as new input.

16.1 Errors

The statistical errors are given in the data tables in the appendix. In the beam asymmetry determination many errors cancel. However, there are significant uncertainties left. The asymmetry determination is sensitive to the empty target subtraction. Oversubtracting the empty target tends to increase the asymmetry while insufficient subtraction of the empty target results in lower asymmetries. Also the beam polarization uncertainty enters into the systematic error for the polarization. These errors are listed in table 16.1 and add in quadrature to the total systematic uncertainty of $\pm 1.4\%$.

Source of error	Error [%]
beam polarization	1
empty target	1
total	1.4

Table 16.1: Systematic errors for the beam asymmetries.

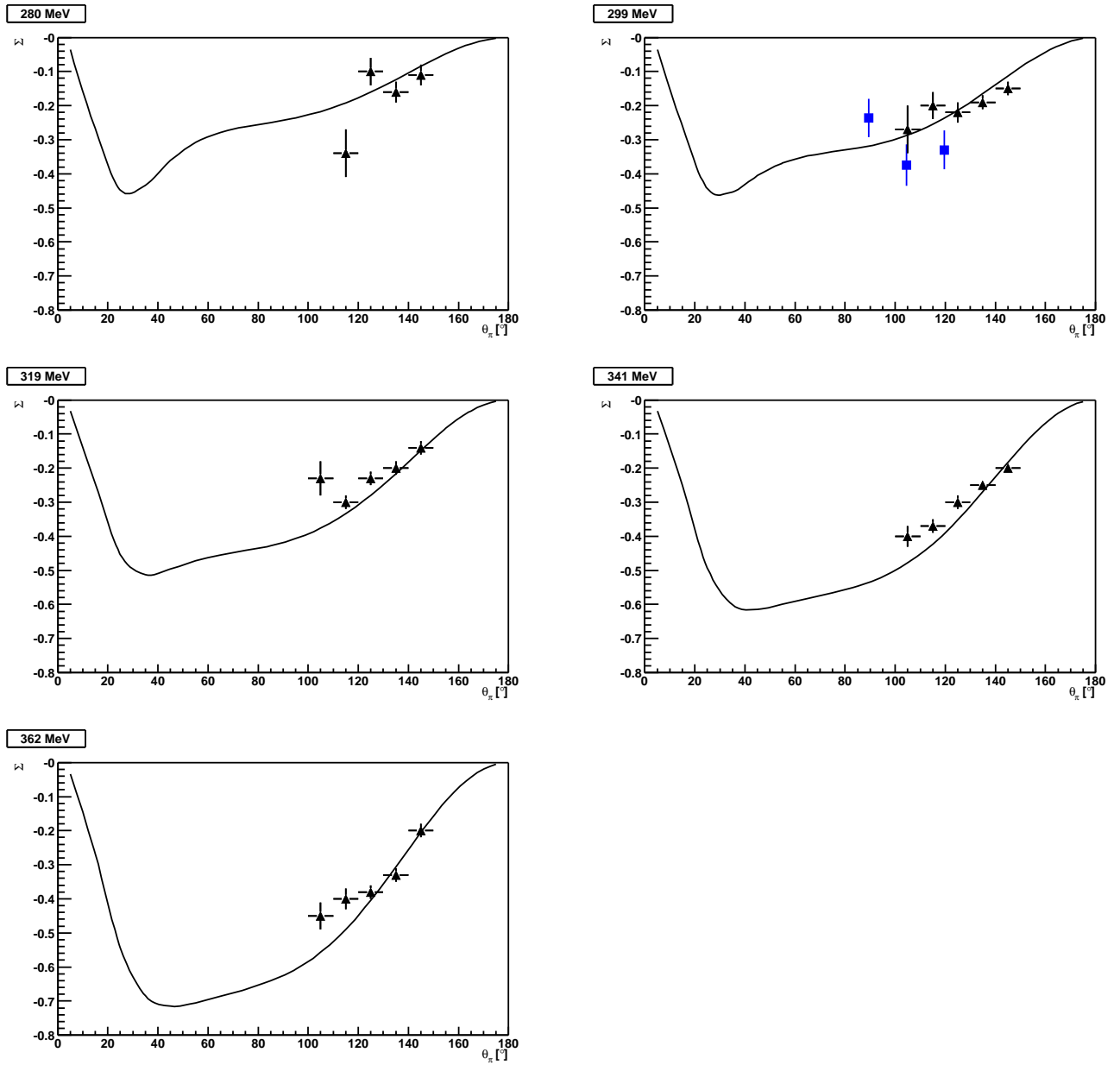


Figure 16.1: Beam asymmetry of exclusive pion production $d(\gamma, \pi^- p)p$ vs. θ_{CM} with comparison to SAID prediction for $n(\gamma, \pi^- p)$.

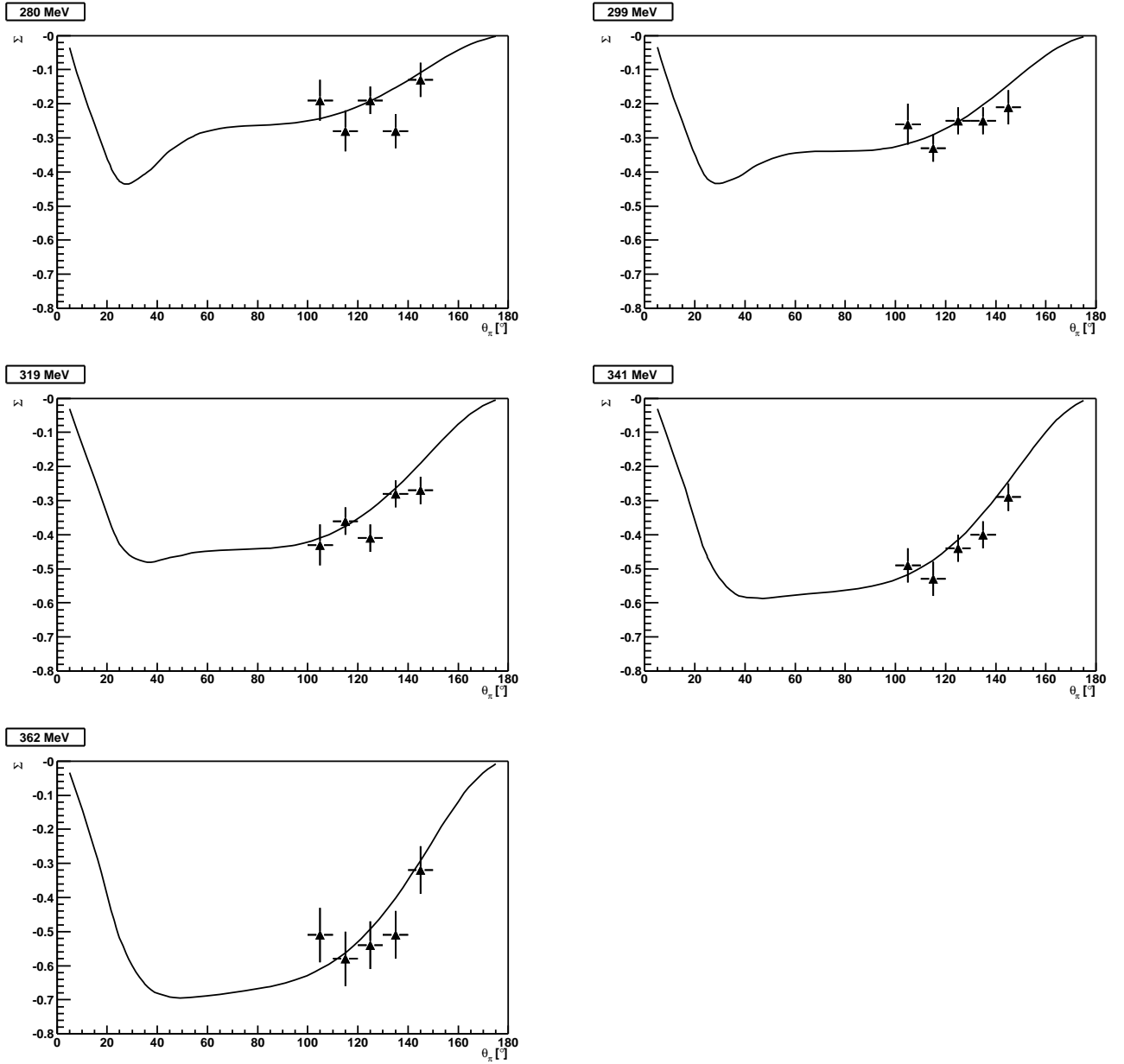


Figure 16.2: Beam asymmetry of exclusive pion production $d(\gamma, \pi^+n)$ (calculated from $[HD(\gamma, \pi^+n)]_{measured}$ and $[p(\gamma, \pi^+n)]_{SAID}$ as in eqn. 16.1) vs. θ_{CM} with comparison to SAID prediction for $p(\gamma, \pi^+n)$.

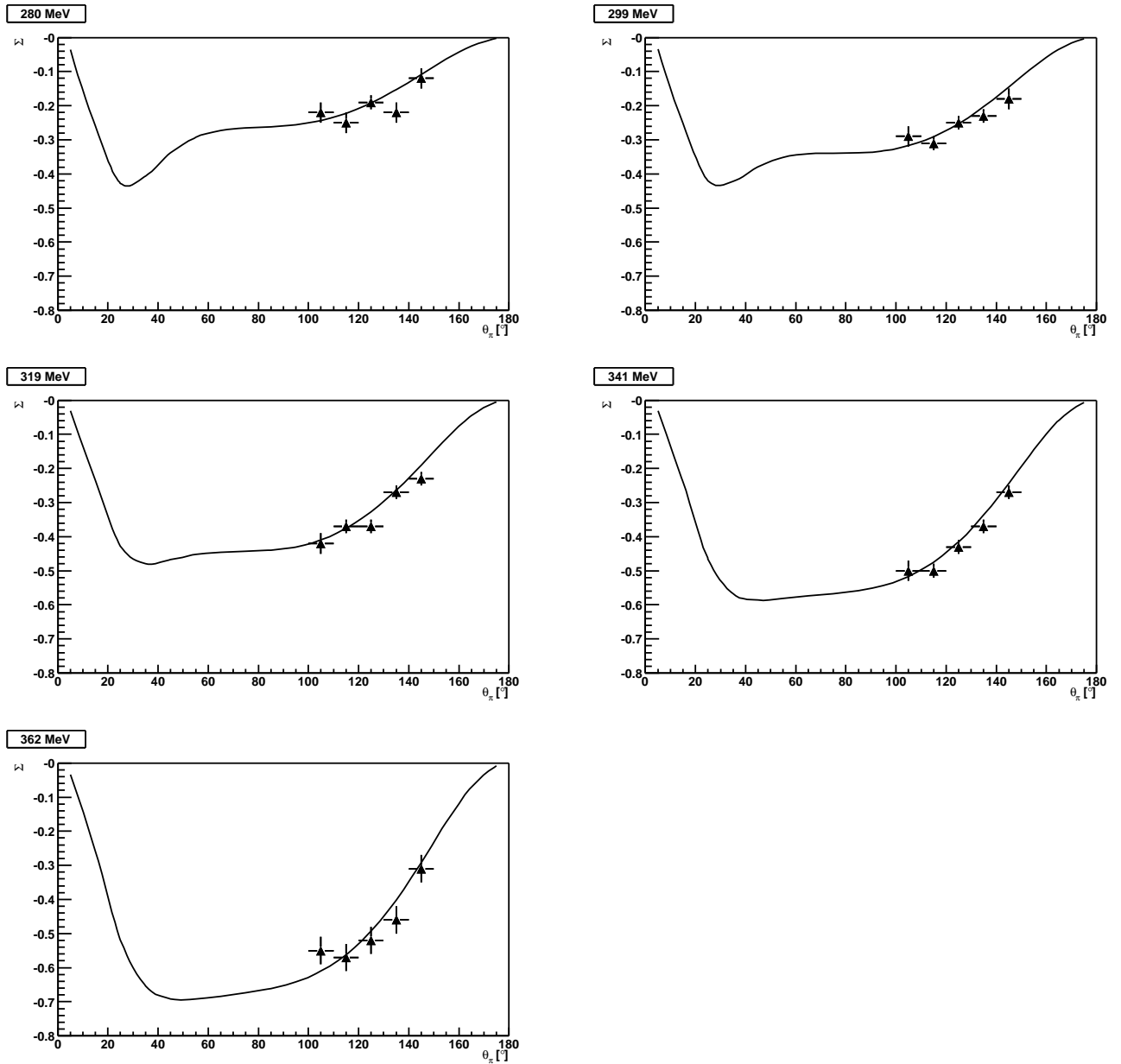


Figure 16.3: Beam asymmetry of exclusive pion production $HD(\gamma, \pi^+n)$ vs. θ_{CM} with comparison to SAID prediction for $p(\gamma, \pi^+n)$.

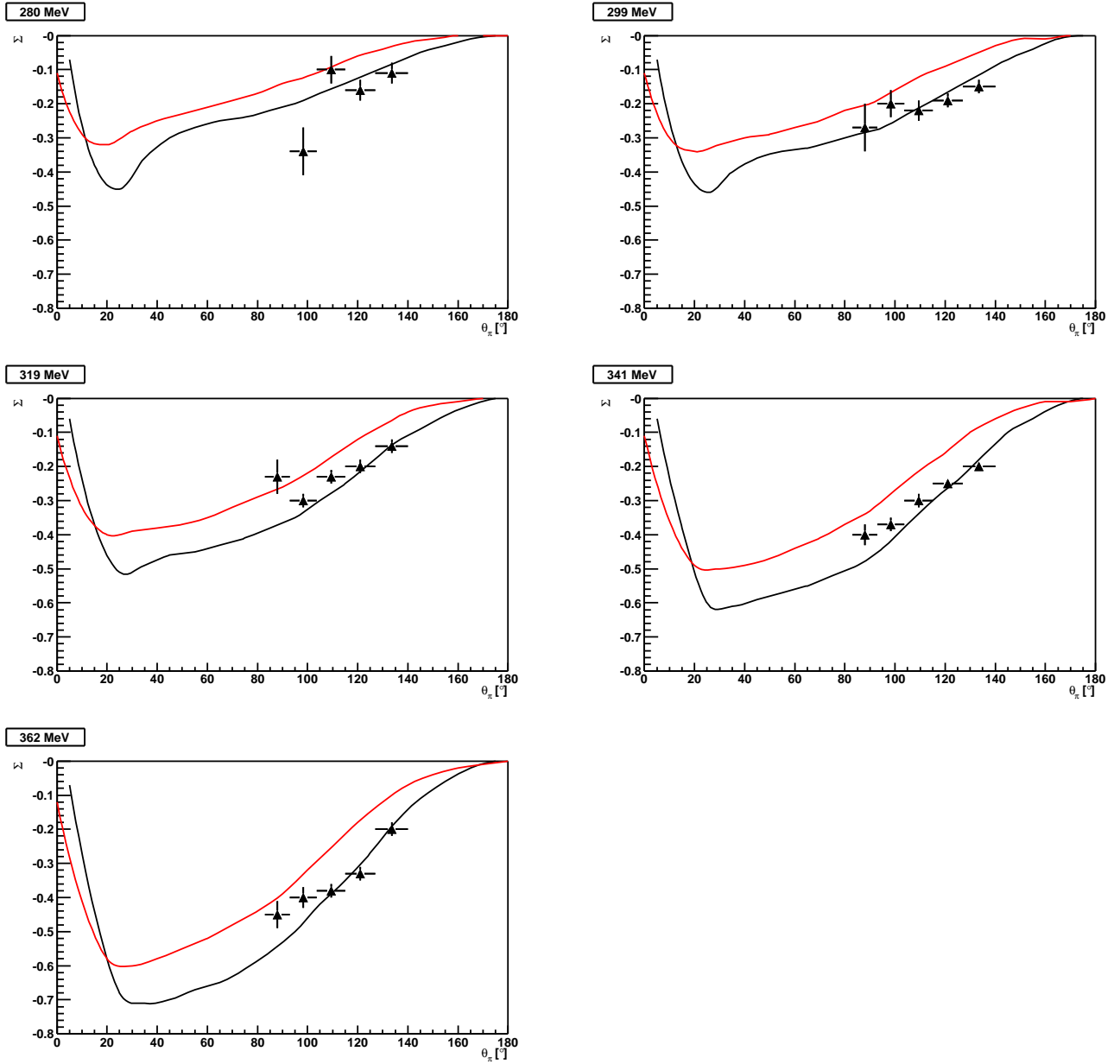


Figure 16.4: Beam asymmetry of exclusive pion production $d(\gamma, \pi^- p)p$ vs. θ_{lab} with comparison to prediction from impulse calculation (red) and to SAID prediction for $n(\gamma, \pi^- p)$ (black).

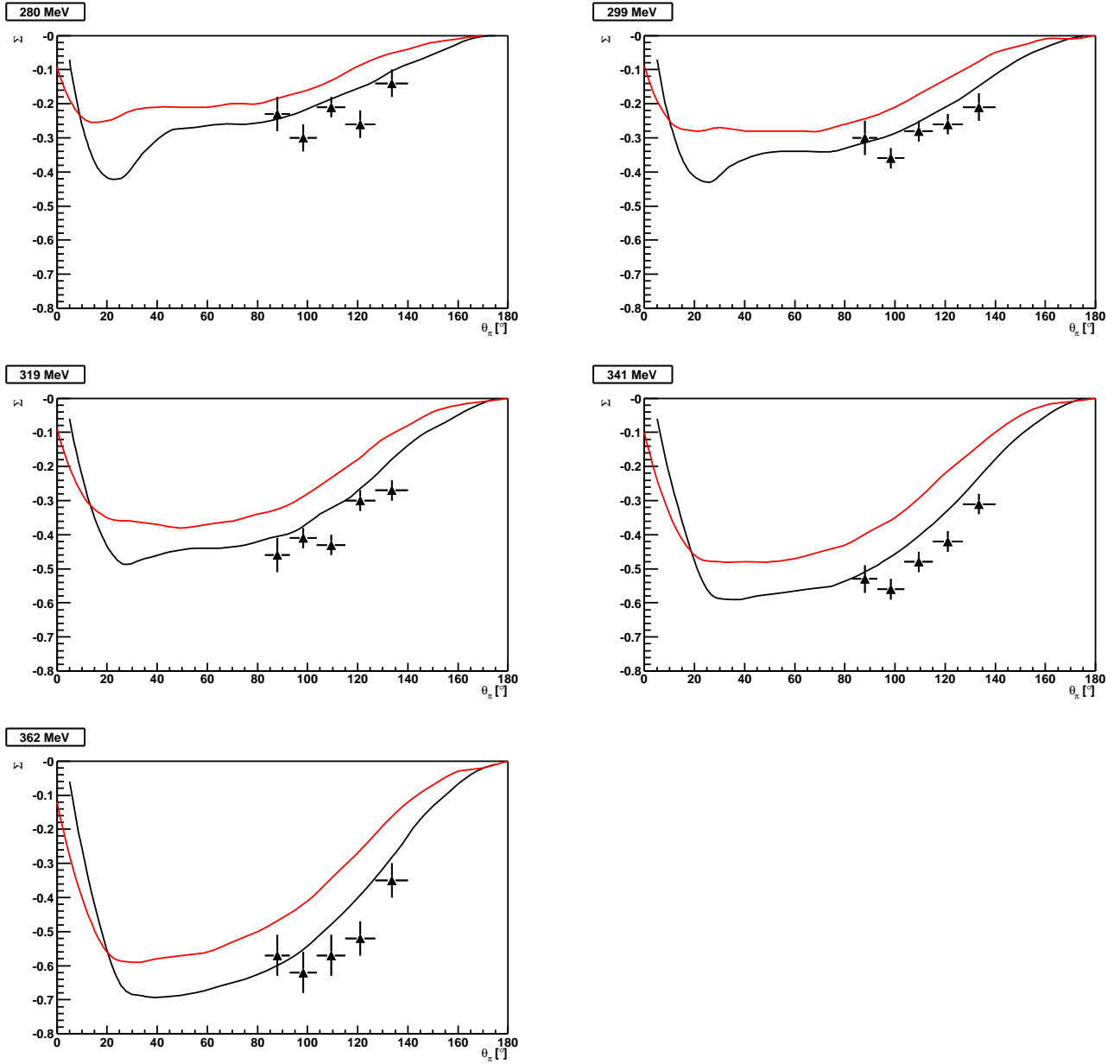


Figure 16.5: Beam asymmetry of exclusive pion production $d(\gamma, \pi^+n)$ (calculated from $[HD(\gamma, \pi^+n)]_{measured}$ and $[p(\gamma, \pi^+n)]_{SAID}$ as in eqn. 16.1) vs. θ_{lab} with comparison to prediction from impulse calculation (red) and to SAID prediction for $p(\gamma, \pi^+n)$ (black).

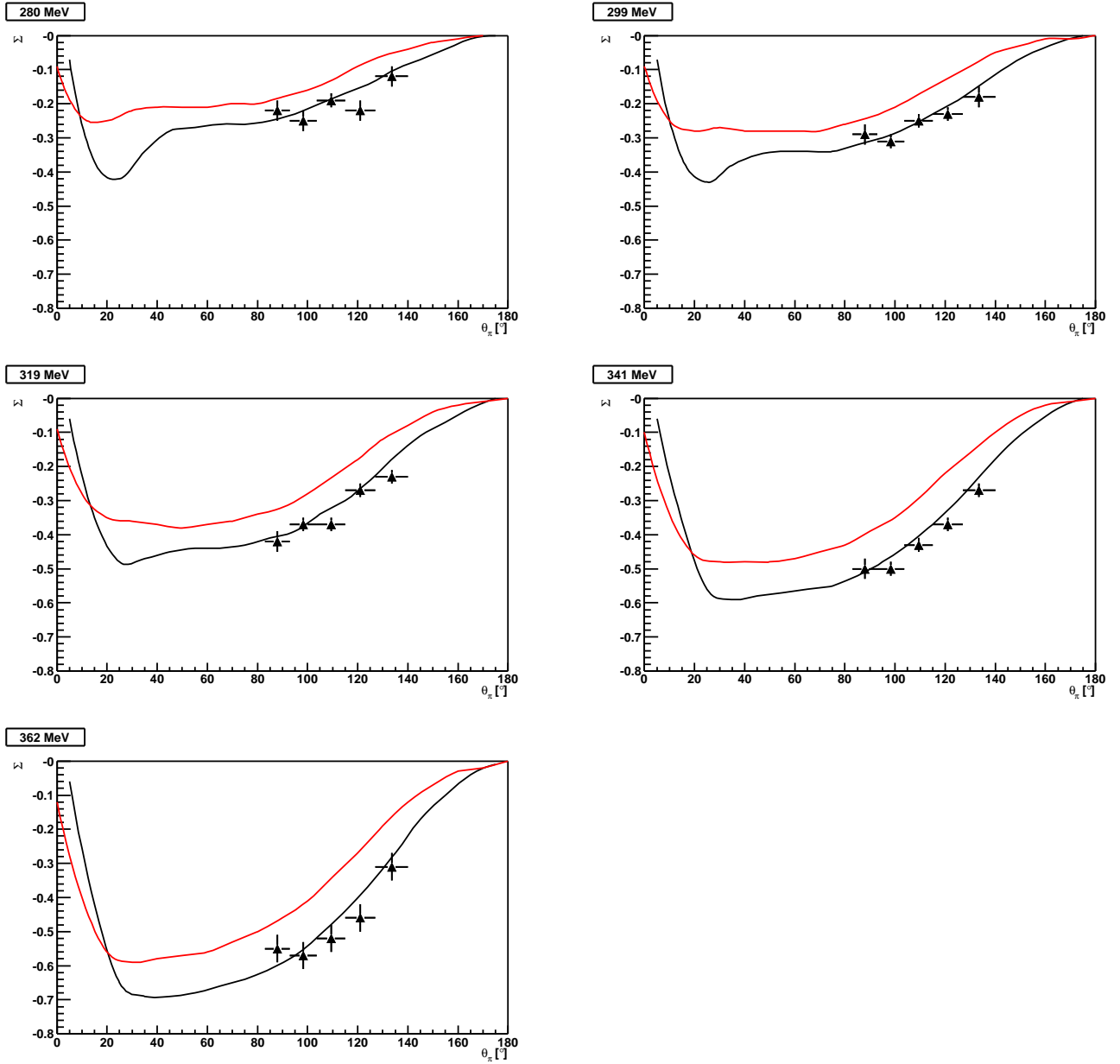


Figure 16.6: Beam asymmetry of exclusive pion production $HD(\gamma, \pi^+n)$ vs. θ_{lab} with comparison to prediction from impulse calculation (red) and to SAID prediction for $p(\gamma, \pi^+n)$ (black).

Chapter 17

Conclusion

Differential cross sections and beam asymmetries of charged pions have been measured on HD. From the measured cross section for $HD(\gamma, \pi^+n)$ the cross section for $d(\gamma, \pi^+n)$ has been constructed by subtraction of the known cross section on the free proton. These measurements increase the available world data set that is used in the multipole fits. Especially the new data on the beam asymmetry in the π^- channel is useful.

This data also gives input to the development of a theoretical model of the deuteron. Such a model is important because the extraction of observables for the free neutron and a test of isospin symmetry in the nucleon rely on it. Calculations from the impulse approximation show how the Fermi motion of the nucleons change the observables. The cross sections are lowered compared to the free nucleons. The asymmetries are reduced. The model predictions may change as the model is developed further. Data and model predictions from the impulse approximation alone do not agree well. However, the impulse approximation gives a first understanding of the deuteron. The observed cross sections in the π^- on the deuteron are lower than the SAID predictions for beam energies below 340 MeV. This is where the difference between the impulse calculation and the SAID prediction is large as well.

In the π^- channel a slight deviation in the beam asymmetry from the SAID predictions for the free neutron has been observed. A measurement at $\theta_{CM} < 100^\circ$ is needed to further examine this deviation.

Chapter 18

Outlook

While the present experiment provides valuable data it also served to validate the experimental setup for future runs. The upgrade of the detector system with the neutron barrel and then the TPC will improve the solid angle coverage and performance of the detector significantly. The neutron barrel will extend the solid angle coverage for nucleons of the detector setup. This will extend the measurement of exclusive beam asymmetries to lower pion angles, the region where binding effects may be important.

The newly developed HD target has been used in an experiment for the first time. Data with a polarized target will provide an interesting test of the GDH sum rule. With the unique capabilities of the HD target, beam, and detector, the LEGS group can look forward to an exciting future.

Bibliography

- [1] R. A. Arndt *et al.*, Phys. Rev. C **42**, 1853 (1990) and references therein
- [2] I. S. Barker *et al.*, Nucl. Phys. B **95**, 347 (1975)
- [3] T. Sato and T.-S. H. Lee, Phys. Rev. C **54**, 2660 (1996)
- [4] T. Sato and T.-S. H. Lee, Phys. Rev. C **63**, 055201 (2001)
- [5] M. Gell-Mann *et al.*, Phys. Rev. **95**, 1612 (1954)
- [6] S. B. Gerasimov, Sov. Journal of Nucl. Phys. **2**, 430 (1966)
- [7] S. D. Drell and A. C. Hearn, Phys. Rev. Lett. **16**, 908 (1966)
- [8] F. E. Low, Phys. Rev. **96**, 1428 (1954)
- [9] M. Gell-Mann and M. L. Goldberger, Phys. Rev. **96**, 1433 (1954)
- [10] Lino Miceli, 'Simultaneous Measurement of Positive Pion Photoproduction Cross Section and Beam Asymmetries with Linearly Polarized Photons in the Delta-Region', PhD thesis, LEGS publication LEGS-01T1 (2001)
- [11] R. H. Milburn, Phys. Rev. Lett. **10**, 75 (1963)
- [12] F. R. Arutyunian, V. A. Tumanian, Phys. Lett. **4**, 176 (1963)
- [13] O. Klein and Y. Nishina, Zeitschrift f. Physik **52**, 853 (1929)
- [14] A. Honig, Q. Fan, X. Wei, M. Breuer, J. P. Didelez, M. Rigney, M. Lowry, A. Sandorfi, A. Lewis and S. Whisnant, Proceeding of 12th Int'l Symp. on High Energy Spin Physics, Amsterdam, Sept. 1996, World Scientific, p. 365 (1997)
- [15] X. Wei, A. Honig, A. Lewis, M. Lowry, A. Sandorfi, S. Whisnant and J. P. Didelez, Physica B **284-288**, 2051 (2000)
- [16] A. Honig, X. Wei, F. Lincoln, M. Lowry, A. Sandorfi, A. Lewis, S. Whisnant, C. Commeaux, J. P. Didelez and C. Schaerf, Proceeding of Int'l Workshop on Polarized Sources and Targets, Erlangen, Sept. 29-Oct. 2, 1999, PST99, p. 392 (2000)

- [17] A. Honig, Q. Fan, X. Wei, A. Sandorfi and S. Whisnant, Nucl. Inst. Meth. **A356**, 39 (1995)
- [18] e.g.: E. J. Beise *et al.*, Nucl. Instrum. Meth. **A378**, 383-391 (1996); M. M. Pavan *et al.*, Phys.Rev. **C64**, 064611 (2001)
- [19] e.g.: G. Blanpied *et al.*, Phys. Rev. **C 52**, R455 (1995)
- [20] C. Bradtke *et al.*, Nucl. Instrum. Methods Phys. Res. **A 436**, 430 (1999)
- [21] e.g.: K. Abe *et al.*, Phys. Rev. **D 58**, 112003 (1998)
- [22] S. L. Wilson *et al.*, Nucl. Instrum. Methods Phys. Res. **A 264**, 263 (1988)
- [23] W. W. MacKay *et al.*, Phys. Rev. **D 29**, 2483 (1984)
- [24] S. Whisnant *et al.*, private communication
- [25] K. Ardashev, PhD thesis, LEGS report LEGS-02T1
- [26] Stanton Code available from Edwards Laboratory, Ohio University, Athens, Ohio
- [27] F. Partovi, Ann. Phys. **27**, 79 (1964)
- [28] SAID Partial Wave Analysis, <http://gwdac.phys.gwu.edu/>
- [29] P. Benz *et al.*, Nucl. Phys. **B 65**, 158 (1973)
- [30] K. Kondo *et al.*, Phys. Rev. **D 9**, 529 (1974)

Appendix A

Data tables

θ_{CM}	280.1 MeV	299.1 MeV	319.5 MeV	341.6 MeV	362.5 MeV
105°	36.33 ± 0.87	43.95 ± 0.96	46.01 ± 0.99	42.87 ± 0.93	34.62 ± 1.18
115°	37.16 ± 0.70	41.91 ± 0.73	43.49 ± 0.73	35.77 ± 0.66	28.73 ± 0.82
125°	40.01 ± 0.74	44.26 ± 0.79	41.82 ± 0.72	35.07 ± 0.63	28.00 ± 0.80
135°	39.29 ± 0.74	43.54 ± 0.75	40.76 ± 0.68	33.01 ± 0.60	24.91 ± 0.73
145°	38.85 ± 0.90	40.41 ± 0.91	38.15 ± 0.80	32.27 ± 0.68	23.30 ± 0.76

Table A.1: $d\sigma/d\Omega[\mu b/sr]$ for $HD(\gamma, \pi^+n)$, CM frame.

θ_{CM}	280.1 MeV	299.1 MeV	319.5 MeV	341.6 MeV	362.5 MeV
105°	16.22 ± 0.87	21.23 ± 0.96	23.46 ± 0.99	24.02 ± 0.93	20.08 ± 1.18
115°	17.19 ± 0.70	19.60 ± 0.73	21.65 ± 0.73	17.85 ± 0.66	15.19 ± 0.82
125°	20.60 ± 0.74	22.81 ± 0.79	21.11 ± 0.72	18.35 ± 0.63	15.58 ± 0.80
135°	20.71 ± 0.74	23.25 ± 0.75	21.43 ± 0.68	17.64 ± 0.60	13.64 ± 0.73
145°	21.19 ± 0.90	21.36 ± 0.91	20.22 ± 0.80	18.21 ± 0.68	13.10 ± 0.76

Table A.2: $d\sigma/d\Omega[\mu b/sr]$ for $d(\gamma, \pi^+n)n$ (calculated as $[HD(\gamma, \pi^+n)]_{measured} - [p(\gamma, \pi^+n)]_{SAID}$), CM frame.

θ_{CM}	280.1 MeV	299.1 MeV	319.5 MeV	341.6 MeV	362.5 MeV
105°	12.28 ± 1.40	17.31 ± 0.92	18.53 ± 0.68	19.56 ± 0.53	17.65 ± 0.61
115°	15.07 ± 0.79	20.10 ± 0.57	20.75 ± 0.42	19.82 ± 0.34	18.33 ± 0.42
125°	18.90 ± 0.57	21.22 ± 0.43	22.33 ± 0.33	20.34 ± 0.28	17.43 ± 0.34
135°	20.51 ± 0.44	22.94 ± 0.35	22.08 ± 0.28	19.61 ± 0.24	16.44 ± 0.30
145°	20.73 ± 0.45	23.49 ± 0.39	23.55 ± 0.32	19.73 ± 0.26	17.26 ± 0.32

Table A.3: $d\sigma/d\Omega[\mu b/sr]$ for $d(\gamma, \pi^-p)p$, CM frame.

θ_{CM}	280.1 MeV	299.1 MeV	319.5 MeV	341.6 MeV	362.5 MeV
105°	-0.22 ± 0.03	-0.29 ± 0.03	-0.42 ± 0.03	-0.50 ± 0.03	-0.55 ± 0.04
115°	-0.25 ± 0.03	-0.31 ± 0.02	-0.37 ± 0.02	-0.50 ± 0.02	-0.57 ± 0.04
125°	-0.19 ± 0.02	-0.25 ± 0.02	-0.37 ± 0.02	-0.43 ± 0.02	-0.52 ± 0.04
135°	-0.22 ± 0.03	-0.23 ± 0.02	-0.27 ± 0.02	-0.37 ± 0.02	-0.46 ± 0.04
145°	-0.12 ± 0.03	-0.18 ± 0.03	-0.23 ± 0.02	-0.27 ± 0.02	-0.31 ± 0.04

Table A.4: Beam asymmetry for $HD(\gamma, \pi^+n)$, CM frame.

θ_{CM}	280.1 MeV	299.1 MeV	319.5 MeV	341.6 MeV	362.5 MeV
105°	-0.18 ± 0.07	-0.26 ± 0.05	-0.42 ± 0.05	-0.48 ± 0.05	-0.50 ± 0.08
115°	-0.29 ± 0.05	-0.33 ± 0.05	-0.37 ± 0.04	-0.53 ± 0.05	-0.59 ± 0.08
125°	-0.19 ± 0.04	-0.25 ± 0.04	-0.40 ± 0.04	-0.45 ± 0.04	-0.54 ± 0.07
135°	-0.28 ± 0.04	-0.26 ± 0.04	-0.28 ± 0.04	-0.40 ± 0.04	-0.52 ± 0.07
145°	-0.12 ± 0.05	-0.21 ± 0.05	-0.27 ± 0.04	-0.28 ± 0.04	-0.32 ± 0.07

Table A.5: Beam asymmetry for $d(\gamma, \pi^+n)n$ (calculated from $[HD(\gamma, \pi^+n)]_{measured}$ and $[p(\gamma, \pi^+n)]_{SAID}$), CM frame.

θ_{CM}	280.1 MeV	299.1 MeV	319.5 MeV	341.6 MeV	362.5 MeV
105°	0.07 ± 0.16	-0.27 ± 0.07	-0.23 ± 0.05	-0.40 ± 0.03	-0.45 ± 0.04
115°	-0.34 ± 0.07	-0.20 ± 0.04	-0.30 ± 0.02	-0.37 ± 0.02	-0.40 ± 0.03
125°	-0.10 ± 0.04	-0.22 ± 0.03	-0.23 ± 0.02	-0.30 ± 0.02	-0.38 ± 0.02
135°	-0.16 ± 0.03	-0.19 ± 0.02	-0.20 ± 0.02	-0.25 ± 0.01	-0.33 ± 0.02
145°	-0.11 ± 0.03	-0.15 ± 0.02	-0.14 ± 0.02	-0.20 ± 0.01	-0.20 ± 0.02

Table A.6: Beam asymmetry for $d(\gamma, \pi^-p)p$, CM frame.

θ_{lab}	280.1 MeV	299.1 MeV	319.5 MeV	341.6 MeV	362.5 MeV
105°	32.40 ± 0.61	35.39 ± 0.64	33.95 ± 0.59	27.83 ± 0.52	22.13 ± 0.64
115°	28.66 ± 0.61	32.22 ± 0.63	29.42 ± 0.56	24.08 ± 0.49	18.19 ± 0.60
125°	26.53 ± 0.64	27.50 ± 0.64	25.49 ± 0.55	20.08 ± 0.47	14.93 ± 0.52
135°	24.33 ± 0.74	25.39 ± 0.72	23.56 ± 0.63	20.35 ± 0.54	13.97 ± 0.62

Table A.7: $d\sigma/d\Omega[\mu b/sr]$ for $HD(\gamma, \pi^+n)$, lab frame.

θ_{lab}	280.1 MeV	299.1 MeV	319.5 MeV	341.6 MeV	362.5 MeV
105°	16.63 ± 0.61	18.03 ± 0.64	17.34 ± 0.59	14.51 ± 0.52	12.37 ± 0.64
115°	14.78 ± 0.61	17.10 ± 0.63	15.09 ± 0.56	12.84 ± 0.49	10.01 ± 0.60
125°	14.24 ± 0.64	14.28 ± 0.64	13.18 ± 0.55	10.49 ± 0.47	8.02 ± 0.52
135°	13.38 ± 0.74	13.72 ± 0.72	12.82 ± 0.63	12.08 ± 0.54	8.07 ± 0.62

Table A.8: $d\sigma/d\Omega[\mu b/sr]$ for $d(\gamma, \pi^+n)n$ (calculated as $[HD(\gamma, \pi^+n)]_{measured} - [p(\gamma, \pi^+n)]_{SAID}$), lab frame.

θ_{lab}	280.1 MeV	299.1 MeV	319.5 MeV	341.6 MeV	362.5 MeV
105°	15.00 ± 0.49	17.32 ± 0.36	17.83 ± 0.28	16.05 ± 0.23	13.66 ± 0.28
115°	14.76 ± 0.38	16.28 ± 0.30	15.75 ± 0.24	14.48 ± 0.20	11.89 ± 0.24
125°	13.88 ± 0.34	15.37 ± 0.27	14.66 ± 0.22	12.08 ± 0.18	10.36 ± 0.22
135°	13.04 ± 0.35	14.51 ± 0.30	14.44 ± 0.24	12.01 ± 0.20	10.12 ± 0.24

Table A.9: $d\sigma/d\Omega[\mu b/sr]$ for $d(\gamma, \pi^-)p$, lab frame.

θ_{lab}	280.1 MeV	299.1 MeV	319.5 MeV	341.6 MeV	362.5 MeV
87°	-0.22 ± 0.03	-0.29 ± 0.03	-0.42 ± 0.03	-0.50 ± 0.03	-0.55 ± 0.04
97.5°	-0.25 ± 0.03	-0.31 ± 0.02	-0.37 ± 0.02	-0.50 ± 0.02	-0.57 ± 0.04
109°	-0.19 ± 0.02	-0.25 ± 0.02	-0.37 ± 0.02	-0.43 ± 0.02	-0.52 ± 0.04
120.5°	-0.22 ± 0.03	-0.23 ± 0.02	-0.27 ± 0.02	-0.37 ± 0.02	-0.46 ± 0.04
133°	-0.12 ± 0.03	-0.18 ± 0.03	-0.23 ± 0.02	-0.27 ± 0.02	-0.31 ± 0.04

Table A.10: Beam asymmetry for $HD(\gamma, \pi^+n)$, lab frame.

θ_{lab}	280.1 MeV	299.1 MeV	319.5 MeV	341.6 MeV	362.5 MeV
87°	-0.23 ± 0.05	-0.30 ± 0.05	-0.46 ± 0.05	-0.53 ± 0.04	-0.57 ± 0.06
97.5°	-0.30 ± 0.04	-0.36 ± 0.03	-0.41 ± 0.03	-0.56 ± 0.03	-0.62 ± 0.06
109°	-0.21 ± 0.03	-0.28 ± 0.03	-0.43 ± 0.03	-0.48 ± 0.03	-0.57 ± 0.06
120.5°	-0.26 ± 0.04	-0.26 ± 0.03	-0.30 ± 0.03	-0.42 ± 0.03	-0.52 ± 0.05
133°	-0.14 ± 0.04	-0.21 ± 0.04	-0.27 ± 0.03	-0.31 ± 0.03	-0.35 ± 0.05

Table A.11: Beam asymmetry for $d(\gamma, \pi^+n)n$ (calculated from $[HD(\gamma, \pi^+n)]_{measured}$ and $[p(\gamma, \pi^+n)]_{SAID}$), lab frame.

θ_{lab}	280.1 MeV	299.1 MeV	319.5 MeV	341.6 MeV	362.5 MeV
87°	0.07 ± 0.16	-0.27 ± 0.07	-0.23 ± 0.05	-0.40 ± 0.03	-0.45 ± 0.04
97.5°	-0.34 ± 0.07	-0.20 ± 0.04	-0.30 ± 0.02	-0.37 ± 0.02	-0.40 ± 0.03
109°	-0.10 ± 0.04	-0.22 ± 0.03	-0.23 ± 0.02	-0.30 ± 0.02	-0.38 ± 0.02
120.5°	-0.16 ± 0.03	-0.19 ± 0.02	-0.20 ± 0.02	-0.25 ± 0.01	-0.33 ± 0.02
133°	-0.11 ± 0.03	-0.15 ± 0.02	-0.14 ± 0.02	-0.20 ± 0.01	-0.20 ± 0.02

Table A.12: Beam asymmetry for $d(\gamma, \pi^-)p$, lab frame.

Vita

Holger Meyer was born in Braunschweig, Germany on 26. July 1972. He studied physics at the Technische Universität Braunschweig from 1992 to 1995 and at Virginia Polytechnic Institute and State University where he earned a Master of Science in 1996. In 1998 he moved to Brookhaven National Lab to join the LEGS group for his Doctoral studies.